UNIVERSITY OF OKLAHOMA

GRADUATE COLLEGE

# QUANTIFYING THE IMPACT OF EXPERIMENTAL FACTORS ON THE MEASUREMENT OF DYNAMIC CAPILLARY EFFECTS IN UNSATURATED POROUS MEDIA

A DISSERTATION

SUBMITTED TO THE GRADUATE FACULTY

in partial fulfillment of the requirements for the

Degree of

DOCTOR OF PHILOSOPHY

By

LILI HOU
Norman, Oklahoma
2014

QUANTIFYING THE IMPACT OF EXPERIMENTAL FACTORS ON THE MEASUREMENT OF DYNAMIC CAPILLARY EFFECTS IN UNSATURATED POROUS MEDIA

A DISSERTATION APPROVED FOR THE
SCHOOL OF CIVIL ENGINEERING AND ENVIRONMENTAL SCIENCE

BY

_____
Dr. Tohren C. G. Kibbey, Chair

_____
Dr. Faruk Civan

_____
Dr. Randall L. Kolar

_____
Dr. Gerald A. Miller

_____
Dr. K.K. Muraleetharan

© Copyright by LILI HOU 2014
All Rights Reserved.

This material is based upon work supported by the National Science Foundation under Grant No. 0911139.

Chapter 3 has been previously published as "Dynamic capillary effects in a small-volume unsaturated porous medium: Implications of sensor response and gas pressure gradients for understanding system dependencies" in *Water Resources Research*, 2012 and is used here by permission.

Chapter 5 has been previously published as "The influence of unavoidable saturation averaging on the experimental measurement of dynamic capillary effects: A numerical simulation study" in *Advances in Water Resources*, 2014 and is used here by permission.

## Acknowledgements

The past four years might be the most influential period of my life – I have grown up as an independent person, physically, mentally, and financially. At this moment, I really would like to express my gratitude to many names.

First of all, I would like to thank my advisor Dr. Tohren Kibbey for everything he did for me throughout my study. I am so grateful to have him as my mentor. I must thank him for his plentiful good ideas and constructive insights, for his patience and time to an academic newbie, for always being there to offer help, for absolute understanding, and for financial support. His enthusiasm in research, belief in truth, confidence in his own academic opinions, and toughness to challenges deeply influence me and encourage me to try and achieve more. Without his encouragement, guidance and support, I would not have been able to finish my study.

I also gratefully thank the committee members of my doctoral study, Dr. Faruk Civan, Dr. Randall Kolar, Dr. Gerald Miller, Dr. K. K. Muraleetharan, and Dr. Dimitrios Papavassiliou, for their interest in my study and for their time, support and invaluable suggestions on my research.

Special gratitude is given to Dr. Elizabeth Butler, Drs. John and Barbara Wilson, and Dr. Fei Liu. Without the encouragement and support from Dr. Liu, the recommendation from Dr. Wilson, and the consideration from Dr. Butler, I had no chance to stay and study at this peaceful college town. Over the last seven years, discussions with Dr. Liu on almost every aspect of my life are indispensable parts leading me to this stage.

I sincerely thank Dr. Janis Paul, for the writing skills she taught me, and especially for the understanding, encouragement, support, and the hug she gave me during my depression days, the darkest days so far in my life. Speaking of the darkest days, I really have to thank my parents, my advisor, Dr. Paul, somebody, Junyi, Yuan, and Qiong for being supportive. More gratitude words are reserved because words are weak.

I would like to thank Dr. Lixia Chen for her helps and suggestions on my research and my life in the United States. Also thank Michael Schmitz and Ronald Conlon for their assistance in experimental apparatus fabrication and equipment maintenance. Mike always considers my requests for apparatus modifications as high priority jobs, which facilitates the research progress to a great extent.

I would like to thank my American family, the Marrs family, for their adopting me as a family member, and for all the joys they offered. I also thank my friends I met here for their company and help. We learned from each other and made progress on our studies, works and lives.

Last but not least, I would like to thank my parents and my families for their unconditional love since the very beginning of my life. Despite being born in a family without a good financial situation, I was able to focus on pursuing my studies all because of my parents' determination and sacrifice. It is their diligence and stubbornness that encourages me never to stop improving myself.

I know there are still many things I have to learn or to improve both as a scholar and, in a broader scope, as a human being. I deeply know while all the failure and humiliations I have experienced are attributed to my own faults, all the success and

glories I have achieved go to those people around me. I have no choice but to do my best to be a better scholar and be a better human being in return for the love, support, and encouragement I've ever received. And last, one more reminder for myself (for my procrastination actually): every minute counts and your effort will finally pay off.

# Table of Contents

# List of Tables

# List of Figures

## Abstract

Multiphase flow is an important phenomenon in many natural and engineering systems; for example, oil recovery and water movement in the unsaturated zone are two common multiphase flow systems. The capillary pressure-saturation ($P_c$-$S_w$) relationship, a constitutive relationship between pressure between phases (the capillary pressure, $P_c$) and the water saturation ($S_w$), has been studied over nearly the past hundred years. Studies of $P_c$-$S_w$ relationships are complicated by the often-reported observation of dynamic capillary effects. Dynamic capillary effects refer to a range of observed capillary phenomena which appear to occur under conditions of dynamic saturation change. One of the most widely investigated dynamic effects is the observed rate-dependence of capillary pressures. The focus of the work described here was on studying dynamic capillary effects in the $P_c$-$S_w$ relationship. Specifically, the work aimed to understand how measurement factors impact the magnitude of observed dynamic capillary effects.

A number of studies have experimentally investigated the magnitude of dynamic capillary effects. Many have calculated a dynamic capillary coefficient, $\tau$, as a measure of the magnitude of dynamic capillary effects. The results of reported $\tau$ values have differed widely from each other, even for systems with seemingly very similar properties. Furthermore, studies have reported different dependencies between system properties and dynamic effects. However, few studies have examined how features of the measurement system have impacted the accuracy of data collected. In this study, three important factors in the measurement were examined: response rates of pressure sensors, gas pressure drops through porous media, and unavoidable spatial averaging in

saturation measurement. Unsaturated drainage experiments in a small-size cell (1.27 cm ID × 2.54 cm H) and a larger column (2.54 cm ID × 15.24 cm H) were conducted to investigate the impact of sensor response and gas pressure gradients on measurement of dynamic effects, and simulations were used to evaluate the effects of gas pressure drops and unavoidable spatial averaging.

Results show that the response rate of pressure sensors has a pronounced impact on the measurement of $\tau$, particularly in systems where drainage is rapid. Even if sensors for both wetting and non-wetting phases respond rapidly, if their response rates do not match each other, the mismatched sensor responses can mimic dynamic capillary effects. Results also show that dynamic capillary pressures determined can be significantly greater than their actual values due to internal gas pressure drops or gradients, if inlet gas pressures are taken as gas phase pressures. The extent of gas pressure drops depends on both porous medium properties and boundary properties. Finally, results show that differences between local and spatially-averaged saturations as well as rates of saturation change can potentially amplify $\tau$ values calculated from measurements. The extent of the amplification is impacted by fluid properties and flow conditions of the multiphase flow system.

# Chapter 1. Introduction

## 1.1 Motivation

A wide range of practical issues involve multiphase flow in porous media. Examples where multiphase flow knowledge is important include design of $CO_2$ sequestration systems, remediation of non-aqueous phase liquid (NAPL) contamination in aquifers, enhanced oil recovery, and improvement of subsurface drip irrigation systems (Kalaydjian 1992; Bhattarai *et al.* 2005; O'Carroll and Sleep 2007; Plug and Bruining 2007; Class *et al.* 2009). It is of critical importance to develop an accurate quantitative understanding of how immiscible fluids flow through porous media to address these practical issues.

The capillary pressure-saturation ($P_c$-$S_w$) relationship, also known as soil-water characteristic curve or water retention function, plays an essential role in understanding immiscible fluids flow and transport in porous materials. Determination of $P_c$-$S_w$ relationships mostly relies on experimental measurements. The experimental results are then often fitted to analytical expressions such as the Brooks and Corey (1966) or van Genuchten (1980) models, to generate parameters needed for hydrologic models. Measurements of $P_c$-$S_w$ relationships have historically been conducted in static or steady-state flow systems. However, getting an equilibrium $P_c$-$S_w$ relationship can be extremely time-consuming and effort-consuming, typically requiring weeks or even months to achieve a complete $P_c$-$S_w$ curve (Gardner 1956; Dane and Hopmans 2002). As a result, dynamic experiments such as one-step or multi-step outflows were developed to determine the $P_c$-$S_w$ relationships with the assistance of flow simulator or parameter optimization approaches (Kool *et al.* 1985; Parker *et al.* 1985; Eching and

Hopmans 1993; Eching *et al.* 1994; Chen *et al.* 1999; O'Carroll *et al.* 2005; Sakaki *et al.* 2010; Diamantopoulos *et al.* 2012). However, many experiments using dynamic systems have reported the observation of dynamic capillary effects during rapid saturation change (Topp *et al.* 1967; Smiles *et al.* 1971; Vachaud *et al.* 1972; Stauffer 1978), complicating the determination of soil capillary properties.

Dynamic capillary effects refer to the observed flow-rate dependence of capillary properties in systems where saturation changes rapidly. The dependence of capillary pressure on flow rate is one of the most studied dynamic effects. A dynamic capillary coefficient, $\tau$, has been widely used in recent publications to quantitatively evaluate the dynamic capillary effect (Hassanizadeh *et al.* 2002; Camps-Roach *et al.* 2010; Joekar-Niasar *et al.* 2010; Bottero *et al.* 2011a; Goel and O'Carroll 2011; Joekar-Niasar and Hassanizadeh 2011). A number of studies have numerically or experimentally explored the magnitude of $\tau$ and its system dependencies (Stauffer 1978; Dahle *et al.* 2005; Gielen *et al.* 2005; Helmig *et al.* 2007; Juanes 2008; Vogel *et al.* 2008; Camps-Roach *et al.* 2010; Joekar-Niasar *et al.* 2010; Joekar-Niasar and Hassanizadeh 2011). However, measurement results obtained from different studies have been contradictory from each other in terms of both the magnitudes of $\tau$ and the quantitative relationships between $\tau$ and system properties. For example, Hassanizadeh *et al.* (2002) reviewed and calculated $\tau$ as a function of saturation in eight publications. Seven out of the eight publications studied unsaturated drainages in sandy materials, yet the $\tau$ values calculated vary from ~$10^4$ to ~$10^7$ Pa·s, a difference spanning three orders of magnitude.

Regarding the great variation in $\tau$ values reported, recent studies have explored the relationship between system properties and $\tau$ (e.g., (Camps-Roach *et al.* 2010; Sakaki *et al.* 2010; Bottero *et al.* 2011b)); reported trends have varied widely. It is possible that the wide variation of both $\tau$ and its dependence on system properties is simply a result of strong sensitivity of $\tau$ to small variations in system properties, such as grain size distribution and fluids involved. However, it is also possible that the accuracy of $\tau$ values obtained is affected, at least in part, by experimental factors during the measurement. For example, if dynamic capillary pressures measured at given saturations differ from their real values due to the impact of measurement artifacts, corresponding $\tau$ values determined will deviate from the real $\tau$. Few studies have quantified the contribution of measurement artifacts to the magnitude of measured $\tau$ values. Without quantifying the contribution of artifacts, it is impossible to precisely quantify the magnitude of dynamic effects, or to understand underlying system dependencies.

## 1.2 Research Objective

The objective of this work is to explore how experimentally-determined $\tau$ can be affected by experimental setups in dynamic measurement systems. A combination of experimental and numerical work was conducted to explore the extents to which capillary pressures or rates of saturation change are affected under different systems. Specifically, two assumptions, rapid pressure sensor response and infinite gas mobility, commonly applied in the course of measuring $P_c$-$S_w$ relationships were examined in systems with different scales. The impacts of applying the two assumptions on measuring results of dynamic capillary pressure or $\tau$ were discussed. In addition,

because saturation readings are actually spatially-averaged values, the impact of this unavoidable saturation averaging on the determination of $\tau$ were numerically studied in systems with different non-wetting phase fluids.

### 1.3 Thesis Outline

The thesis is organized as follows:

**Chapter 2** provides background information, introducing concepts related to multiphase flow theory. The concepts discussed in Chapter 2 are necessary to understand the experimental phenomena discussed in subsequent chapters.

**Chapter 3** describes experimental results examining unsaturated drainage in a small-volume soil cell. Dynamic $P_c$-$S_w$ relationships and corresponding $\tau$ values are calculated with and without corrections for sensor rate and gas pressure artifacts. Impacts of measurement artifacts on the determination of $\tau$ are discussed.

**Chapter 4** describes experimental results examining unsaturated drainage in a larger sand column, with the specific purpose of understanding gas pressure gradients and drops. Trends in gas pressure gradients and drops influenced by system boundary properties are observed and simulated. Implications for dynamic capillary pressure measurement are discussed.

**Chapter 5** describes a numerical simulation study aimed at exploring the effects of saturation spatial averaging on the determination of $\tau$ in systems with different fluid properties.

Finally, **Chapter 6** discusses and summarizes the main findings of the work.

# Chapter 2. Background

Multiphase flow in porous materials is of great interest due to its broad applications in a wide range of natural and engineered systems, such as NAPL contamination remediation in groundwater, enhanced oil recovery, $CO_2$ geological sequestration, and fuel cells. Studies of multiphase flow have largely focused on two-phase flow, such as unsaturated (air-water) flow and oil-water flow. This chapter provides an overview of fundamental concepts and underlying theories associated with the movement of immiscible fluids in porous media. The concepts in this chapter provide background necessary to understand the work exploring dynamic capillary effects described in subsequent chapters.

## 2.1 Fundamental Concepts of Multiphase Flow

### *2.1.1 Interfacial tension and contact angle*

Multiphase flow is simultaneous movements of two or more immiscible fluids in porous materials. Unlike single-phase flow, e.g., the movement of groundwater in aquifers, in which hydraulic gradient is the only fundamental concept as a driving force governing the movement of fluids, fluid behaviors become more complex when it comes to multiphase flow. When two immiscible fluids meet in porous media, three interfaces are formed: one interface between the two fluids, and two interfaces between each fluid and the solid. The formation of interfaces produces two phenomena: interfacial tension and contact angle.

Interfacial tension is a property of the interface between two phases or fluids resulting from intermolecular forces. In the bulk phase of a fluid, molecules are attracted equally by forces from all directions around. These forces cancel out each

other and result in a net force of zero on molecules in bulk phase. When another immiscible fluid is introduced, molecules located on the interface are subjected to imbalance forces from different species of molecules (Bottero 2009). To keep the system at the minimum energy state, the interface wants to minimize its area. Interfacial tension, typically designated as $\gamma$, is the force that exerted on the interface for minimizing interfacial area between the two fluids or phases. Interfacial tension can be referred to as a free energy per unit area ($J/m^2$), or as a force per unit length (N/m) (Adamson and Gast 1997; Hiemenz and Rajagopalan 1997). Interfacial tension is a specific property of the immiscible fluids involved, and thus depends only on the chemical composition of the fluids, and temperature (Hiemenz and Rajagopalan 1997; Bottero 2009).

Another commonly mentioned term is surface tension, which is actually a subset of interfacial tension. While interfacial tension is defined between any two immiscible phases, surface tension requires one phase to be gas (Rosen 2004). All the descriptions and properties of interfacial tension apply to surface tension as well.

When mercury is spilled, it forms as nearly-spherical drops rather than spreading out. This is due both to very high contact angle of mercury on many solid surfaces, as well as the extremely high surface tension of mercury (typically more than five times the surface tension of water). Contact angle is defined as the angle between the tangent of the contact line between two fluids (typically vapor-liquid or liquid-liquid) and the solid surface at the common point where all three materials are in contact, as shown in Figure 2.1. In cases where two phases or liquids (say, a vapor-liquid system) are in

contact with a flat rigid solid surface, contact angle can be related with interfacial tensions using Young's equation (Adamson and Gast 1997):

$$\gamma_{SL} - \gamma_{SV} + \gamma_{LV} \cdot \cos\theta = 0 \qquad \text{(Eq. 2.1)}$$

where $\theta$ is contact angle of phase L, $\gamma_{SL}$, $\gamma_{SV}$ and $\gamma_{LV}$ are interfacial energies between surface S and phase L, surface S and phase V, and phases L and V, respectively.

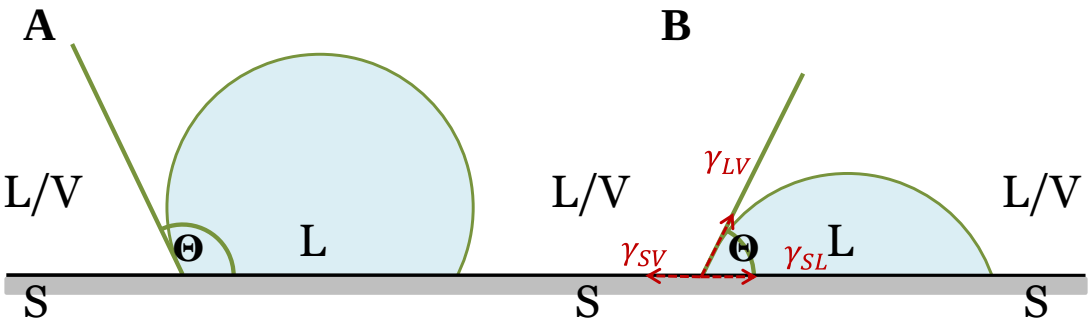


**Figure 2.1. A diagram for illustrating contact angle (L: liquid, S: solid, V: vapor)**

Contact angle describes the affinity of the fluids for the solid surface. Fluids with a smaller contact angle exhibit a greater affinity to the solid, and are more likely to coat the surface (Bottero 2009). Based on the concept of contact angle, immiscible fluids in a multiphase system can be divided into non-wetting and wetting phases. In multiphase flow, the threshold between wetting and non-wetting is considered to be an angle of 90 °. The non-wetting phase is considered to be the fluid whose contact angle is greater than 90 °(e.g., L phase in Figure 2.1A). The wetting phase is the fluid whose contact angle is less than 90 °(e.g., L phase in Figure 2.1B).

### *2.1.2 Capillary pressure*

Associated with interfacial tension and contact angle is the concept of capillarity. A common example of capillarity is capillary rise of a fluid in a narrow glass

tube, driven by capillary forces. Similarly, for immiscible fluids in porous materials, capillary force is the driving force for their movements and distribution. When two fluids meet in a pore space, the interface between fluids is curved due to interfacial tension. This curved interface is referred to as a meniscus. Curvature of meniscus produces a pressure difference across the interface, which is referred to as capillary pressure of the two immiscible fluids in a pore (Leverett 1941; Bear 1972):

$$p_c = p_{nw} - p_w \quad \text{(Eq. 2.2)}$$

where $p_{nw}$ and $p_w$ are the pressure on the interface at the side of the non-wetting phase and the wetting phase, respectively.

From a perspective of geometry, capillary pressure in a pore can be related to the radii of curvature of meniscus by Young-Laplace equation (Adamson and Gast 1997; Hiemenz and Rajagopalan 1997):

$$p_c = \gamma_{nw}\left(\frac{1}{R_1} + \frac{1}{R_2}\right) = \gamma_{nw} \cdot \frac{2}{r} \quad \text{(Eq. 2.3)}$$

where $\gamma_{nw}$ is the interfacial tension between the wetting and non-wetting phases, $R_1$ and $R_2$ denote two principal radii of curvature of meniscus, and $r$ is the mean radii of curvature for simplification or ideal sphere cases. As indicated by Eq. 2.3, the magnitude of capillary pressure depends only on properties of soil and fluids involved.

Both Eq. 2.2 and Eq. 2.3 define capillary pressures at microscopic point, which is valid only on the meniscus in a pore. In practical problems, the concept of capillary pressure is extended at larger scales (e.g., REV scale), described as the macroscopic pressure difference between the non-wetting and wetting phases (Bottero 2009; Armstrong *et al.* 2012):

$$P_c(S) = P_{nw} - P_w \quad \text{(Eq. 2.4)}$$

where $P_{nw}$ and $P_w$ are the measured pressures of the non-wetting and wetting phases in the medium using tensiometer or pressure sensors.

The macroscopic capillary pressure is a statistical average of microscopic capillary pressures over a range of void spaces. As a result, it is a function of saturation of the system. In addition to soil and fluid properties, macroscopic capillary pressure of a multiphase flow system also depends on the geometry of the void space (e.g., grain size and pore-size distribution). Due to the extremely complexity of the geometry of void space in natural systems, it is impossible to analytically describe capillary pressure as a function of saturation. Laboratory measurements are the only way to determine relationships between capillary pressure and saturation ($P_c$-$S_w$ relationships) for a given system (Bear 1972).

## 2.2 Fundamental Equations of Multiphase Flow

In simulation of multiphase flow, each immiscible fluid is considered as a continuum by itself. Conservation and driving force equations have been derived to describe the movement of fluids.

### *2.2.1 Darcy's law*

Originally experimentally determined by Henry Darcy in 1856, Darcy's law describes how fluid continuum responds to local piezometric head (or, potential) gradients in homogeneous porous media (Selker *et al.* 1999; Fetter 2001):

$$Q = -KA\frac{dH}{dl} \quad \text{(Eq. 2.5)}$$

where $Q$ is the volumetric rate through outlet ($m^3/s$), $K$ is the hydraulic conductivity of the porous medium (m/s), $A$ is the cross-sectional area of the column ($m^2$), $H$ is the fluid piezometric head at a given level corresponding to $l$ (m), and $l$ is the length of medium through which flow passes (m). Darcy's law illustrates a linear driving force mechanism of fluid potentials on flow in porous media. It is only valid for laminar flow where *Re* number ($Re = qd/v$) less than 1 (Bear 1972; Fetter 2001). Note that groundwater flow in natural aquifers typically falls into the category of laminar flow.

Hydraulic conductivity, $K$, in Darcy's law is related to the intrinsic permeability of porous media (Fetter 2001):

$$K = \kappa \frac{\rho g}{\mu} \qquad \text{(Eq. 2.6)}$$

where $\kappa$ is the permeability of porous media ($m^2$), $\rho$ is the density of the fluid ($kg/m^3$), $g$ is the gravitational acceleration ($m/s^2$), $\mu$ is the dynamic viscosity of the fluid (kg/(m s)). From Eq. 2.6, it indicates that permeability, which defines the ability of porous medium to transmit fluids, is an intrinsic property of porous media and independent of fluid properties (Todd and Mays 2005). Hydraulic conductivity, however, can be severely affected by the properties of fluids and their distributions in porous media.

For fluid transporting in three-dimensional homogeneous isotropic medium, Darcy's law can be generalized into Eq. 2.7 in terms of fluid pressure instead of potential, with $K$ substituted by Eq. 2.6 (Bear 1972; Bottero 2009):

$$\boldsymbol{q} = -K\nabla H = -\frac{\kappa}{\mu}(\nabla \mathrm{P} - \rho \mathbf{g}) \qquad \text{(Eq. 2.7)}$$

where $\boldsymbol{q}$ is the volumetric flux (the flow rate in a given cross-sectional area, $Q/A$, cm/s).

Eq. 2.7 is derived for movement of single-phase fluid (e.g., groundwater flow in aquifers). To extend Darcy's law into multiphase flow systems, the concept of relative permeability, $k_r$ is introduced. Relative permeability is a measure of the impact of fluid state on permeability of a given fluid in a multiphase flow system. It is defined as the ratio of the permeability of the fluid under specific multiphase conditions to the intrinsic permeability of medium. Relative permeability is a non-linear function of saturation with magnitude ranging from 0 to 1. More information about the relationship between relative permeability and saturation is provided in *section 2.2.4*.

The concept of relative permeability is critical to assessing the mobility of each fluid in a porous medium. Based on relative permeability, the flow of each fluid continuum can be determined by Eq. 2.8, which is one of the fundamental flow equations used in hydrologic models (e.g., (Sleep and Sykes 1993a)):

$$\boldsymbol{q}_\alpha = -\frac{k_{r\alpha}\kappa}{\mu_\alpha}(\nabla \mathrm{P}_\alpha - \rho_\alpha \mathbf{g}), \text{ for } \alpha = nw, w \qquad \text{(Eq. 2.8)}$$

in which $\mathrm{P}_\alpha$ denotes pressure of phase α (Pa).

### *2.2.2 Mass conservation*

The continuum of fluids through a given unit of isothermal porous materials is established based on mass conservation law. The basic idea is the amount of net flux through a control volume should lead to corresponding change in water content (or content of any fluids) in time, as shown in Eq. 2.9 (Selker *et al.* 1999):

$$\frac{\partial \theta}{\partial t} = -\nabla \cdot \boldsymbol{q} \qquad \text{(Eq. 2.9)}$$

in which $\theta$ is the volumetric fluid content.

Applying the continuum concept into the two-phase flow with fluid content being substituted by saturation, Eq. 2.10 can be derived from Eq. 2.9 (Bottero 2009):

$$\frac{\partial}{\partial t}(nS_\alpha\rho_\alpha) + \nabla\cdot(\rho_\alpha \boldsymbol{q}_\alpha) = 0, \text{ for } \alpha = nw, w \quad \text{(Eq. 2.10a)}$$

$$S_{nw} + S_w = 1 \quad \text{(Eq. 2.10b)}$$

where $n$ is the porosity of porous media, $S_\alpha$ is saturation of phase α. Eq. 2.10 together with Eq. 2.8 compose the governing equations for multiphase flow transporting in porous media used in hydrologic models without considering any other sinks or sources.

In unsaturated flow, replacing $\boldsymbol{q}$ in Eq. 2.9 by Darcy's law, and expressing piezometric head as sum of pressure head and elevation head, Eq. 2.9 can be derived as Richards equation, which is a governing equation for unsaturated flow when gas pressure is considered constant (Gardner 1958; Selker *et al.* 1999):

$$\frac{\partial\theta}{\partial t} = \nabla\cdot[K(\theta)\,\nabla h] + \frac{\partial K(\theta)}{\partial z} \quad \text{(Eq. 2.11)}$$

where $K(\theta)$ is unsaturated hydraulic conductivity as a function of water content $\theta$. When gas pressure is zero (atmospheric), pressure head $h$ is an equivalent expression of capillary pressure $P_c$, which is also a function of water content $\theta$.

In order to make Eq. 2.11 look like a classical diffusion equation, it is often written as Eq. 2.12 by introducing 'soil diffusivity' (Gardner 1958; Selker *et al.* 1999):

$$\frac{\partial\theta}{\partial t} = \nabla\cdot[D(\theta)\,\nabla\theta] + \frac{\partial K(\theta)}{\partial z} \quad \text{(Eq. 2.12)}$$

in which $D(\theta) = K(\theta)\frac{\partial h}{\partial\theta}$ is the soil diffusivity. Note that despite of its diffusion form, it is challenge to find analytical solutions of Eq. 2.12 due to the highly non-linear nature of $D(\theta)$ as a function of $\theta$ (Selker *et al.* 1999). Many studies have been conducted to examine the validity of Eq. 2.12 in unsaturated flows (Nielsen *et al.* 1962; Davidson *et*

*al.* 1966; Watson 1966; Topp *et al.* 1967; Smiles *et al.* 1971; Vachaud *et al.* 1972; Stauffer 1978). Some studies have questioned the validity of Eq. 2.12 under conditions where rapid saturation change is observed (e.g., (Nielsen *et al.* 1962; Smiles *et al.* 1971)).

### *2.2.3 The capillary pressure-saturation ($P_c$-$S_w$) relationship*

The combination of Darcy's law (Eq. 2.8) and mass conservation (Eq. 2.10) is not complete for one to predict the transport and distribution of fluids through porous media. To close the system of equations required by hydrological models, it is necessary to derive expressions of pressure and relative permeability of each phase. Phase pressures are the driving forces of flow, and related to each other through capillary pressure, which is a hysteretic function of system saturation (Brooks and Corey 1966; van Genuchten 1980). Relative permeability of a phase is also a function of saturation (see *section 2.2.4*). Saturation mentioned here is the saturation of the wetting-phase (denoted as $S_w$), which is typically water.

The capillary pressure-saturation ($P_c$-$S_w$) relationship has been studied since the beginning of 20th century (e.g., (Gardner 1920; Richards 1928)). $P_c$-$S_w$ relationships were originally studied by agriculturists in soil, and then intensively investigated by petroleum engineers for oil expedition and by hydrologists for understanding the water cycle associated with atmospheric water and groundwater. As mentioned earlier, it is challenging to derive a specific simple analytical expression of capillary pressure as a function of saturation due to complexity of porous media. In general, measurement is the most reliable approach to achieve the $P_c$-$S_w$ relationships. Once measured, $P_c$-$S_w$ curves must be generalized into equation form in order to be used in hydrological

models. Several empirical equations have been developed based on fitting measured results, of which the Brooks-Corey and van Genuchten equations are the most commonly used. The Brooks-Corey equation is shown in Eq. 2.13 (Brooks and Corey 1966):

$$S_e = \begin{cases} \left[\frac{P_d}{P_c}\right]^{\lambda}, P_c \geq P_d \\ 1, P_c \leq P_d \end{cases} \quad \text{(Eq. 2.13)}$$

where $P_d$ is the air entry pressure, $\lambda$ is the pore size distribution index, with small value representing uniform media and large value denoting well-sorted media, $S_e$ is the effective saturation of water ($S_e = (S - S_{rw})/(1 - S_{rw})$), in which $S_{rw}$ is the residual water saturation, denoting the saturation of system at the point that water in the pores becomes discontinuous and cannot be drained anymore. The van Genuchten equation is shown in Eq. 2.14 (van Genuchten 1980):

$$S_e = \frac{1}{[1+(\alpha P_c)^n]^m}, m = 1 - \frac{1}{n} \quad \text{(Eq. 2.14)}$$

where $\alpha$ and $n$ are empirical parameters, with $\alpha$ representing the reciprocal of air entry pressure and $n$ the pore size. Both of these empirical expressions are widely used in numerical models that describe the unsaturated or oil-water flow in subsurface to simulate and predict the movement and distribution of the fluids (e.g., the bounds of a NAPL contaminant plume). For this work, both the Brooks-Corey and van Genuchten models are used to simulate dynamic drainages.

One important characteristic of $P_c$-$S_w$ relationships is hysteresis, which refers to the observed flow path dependence of capillary pressure measured. Typically, a complete $P_c$-$S_w$ relationship consists of a main drainage curve, a main imbibition curve,

and several scanning curves. The main drainage curve takes place in fully saturated system when air displaces water, whereas the main imbibition curve is for water displacing air from residual water saturation ($S_{wr}$) where water cannot drain out anymore. Except for the fully saturated point and residual saturation, any other saturation as the initial point to absorb water or air leads to a different $P_c$-$S_w$ relationship, which is referred to as the scanning curves. The hysteretic nature complicates studies of multiphase flow in that different $P_c$-$S_w$ relationships must be applied depending on wetting-drying history.

Another interesting characteristic of the $P_c$-$S_w$ relationship reported is the observed dependence of system properties (i.e., capillary pressure in this case) on flow rate, sometimes referred to as a dynamic effect. Dynamic effects have been observed in experiments for over 40 years (Topp *et al.* 1967; Watson and Whisler 1968; Smiles *et al.* 1971; Eching and Hopmans 1993; Eching *et al.* 1994; Wildenschild *et al.* 2001; Butters and Duchateau 2002; Simunek and Nimmo 2005; Vogel *et al.* 2008). Quantification of dynamic effect in capillary pressure is the central topic of this study.

### *2.2.4 The relative permeability-saturation ($k_r$-$S_w$) relationship*

Based on Eq. 2.8 and Eq. 2.10, even though a specific $P_c$-$S_w$ relationship is provided, the flow model also requires expressions of phase relative permeability, $k_r$. As mentioned, $k_r$ is a function of saturation, $S_w$. Like $P_c$, phase $k_r$ is also a key parameter for multiphase flow systems, and thus has been extensively studied (e.g., (Burdine 1953; Gardner 1956; Brooks and Corey 1966; Farrell and Larson 1972; Mualem 1976)). Measurement of $k_r$-$S_w$ relationships is an even more burdensome task than measuring $P_c$-$S_w$ relationships. Generally, the relative permeability of the wetting phase, typically

water, is related to the pore size distribution and the tortuosity of pores, and is described as a power function of saturation, with the exponential index assigned by different fitting approaches (Brooks and Corey 1966; van Genuchten 1980; Kuang and Jiao 2011). The relative permeability expression proposed by Brooks and Corey (1966) is one of the most widely applied by multiphase flow models,

$$k_{rw}(S_e) = S_e^{\frac{2+3\lambda}{\lambda}} \quad \text{(Eq. 2.15a)}$$

$$k_{rnw}(S_e) = (1 - S_e)^2(1 - S_e^{\frac{2+\lambda}{\lambda}}) \quad \text{(Eq. 2.15b)}$$

where $k_{rw}$ is the relative permeability of the wetting phase, and $k_{rnw}$ is the relative permeability of the non-wetting phase. Eq. 2.15 is often referred to as the Brooks-Corey-Burdine equations.

Based on the Mualem model (1976) for unsaturated hydraulic conductivity and the van Genuchten model (1980) for $P_c$-$S_w$ relationships, Parker *et al*. (1987) proposed another expression of non-wetting phase relative permeability, which is expressed as Eq. 2.16:

$$k_{rnw}(S_e) = (1 - S_e)^{\frac{1}{2}}(1 - S_e^{\frac{1}{m}})^{2m} \quad \text{(Eq. 2.16)}$$

There are other forms of non-wetting phase relative permeability that have been proposed, mostly showing even greater discrepancies between the model predictions and the measured data. Recently, Kuang and Jiao (2011) derived an new model for predicting $k_{rnw}$ as a function of $S_w$, presenting a better match to the relative air permeability published in sandy materials compared to Brooks-Corey and van Genuchten models, as shown in Eq. 2.17:

$$k_{rnw}(S_e) = (1 - S_e)^{\frac{1}{2}}(1 - S_e^{\frac{1}{m}})^{4m} \quad \text{(Eq. 2.17)}$$

Comparing the above three equations, it can be found that the expression of $k_{rnw}$ can be generalized as the form: $k_{rnw}(S_e) = (1 - S_e)^a(1 - S_e^b)^c$, with *a*, *b*, and *c* corresponding to different fitting parameters. It should be noted that no perfect expressions for relative permeability can be derived, especially for the non-wetting phase. However, using a reasonable model of $k_r$-$S_w$ relationship is of significant importance in precisely simulating the multiphase flow behaviors. The simulated result calculated based on different models can present very different performance, with one model being suitable to some circumstances while not suitable to others. It is critical to select the optimal $k_r$-$S_w$ model for a particular problem.

## 2.3 Dynamic Capillary Effects

Dynamic effects refer to the observed flow-rate dependence of soil hydraulic properties when they are measured under non-equilibrium conditions. As mentioned previously, historically $P_c$-$S_w$ relationships were obtained in static equilibrium measurements, with the whole process taking weeks or even months. Many researchers have reported experiments where the capillary pressures measured under non-steady state deviate from those measured under steady state conditions, and the deviations depend on the flow rate of the system (Topp *et al.* 1967; Smiles *et al.* 1971; Vachaud *et al.* 1972; Stauffer 1978). This flow-rate dependence of capillary pressure has been referred to as a dynamic capillary effect of the $P_c$-$S_w$ relationship (Hassanizadeh *et al.* 2002). While other types of dynamic capillary effects have been reported (e.g., dynamic effects in the $k_r$-$S_w$ (Stauffer 1978; Barenblatt *et al.* 2003)), the work reported in this dissertation focuses specifically on dynamic effects in the $P_c$-$S_w$ relationship. Detailed

background on dynamic capillary effects is provided in Chapters 3-5 in the context of the work discussed in each chapter.

# Chapter 3. The Influence of Sensor Response and Gas Pressure Gradients on the Measurement of $\tau$ in a Small-Volume Unsaturated Porous Medium[*]


## Abstract

Rate dependencies in system properties observed during nonsteady state unsaturated and multiphase flow are often referred to as dynamic capillary effects. One widely-studied dynamic capillary effect is the apparent dependence of measured capillary pressure on the rate of saturation change. While this phenomenon has been observed for over four decades, a clear picture of the source of the phenomenon and its true magnitude remains elusive. Furthermore, reported dependencies on system properties and state variables have been contradictory. The focus of this work was on quantifying the relationship between measured capillary pressure and rate of saturation change using a small volume system with highly-characterized fluid-selective microsensors. Experimental measurements in three systems were used to calculate the dynamic capillary coefficient $\tau$ as a function of saturation during drainage. Corrections for sensor response and flow-induced gas pressure gradients were applied to explore how these potential artifacts would impact measured $\tau$ values. Significant differences in $\tau$ values were observed in uncorrected measurement between the three systems, but corrected values were very similar in all cases. Corrected $\tau$ values were found to be on the order of $10^3$ Pa s or less – one to two orders of magnitude lower than the uncorrected values, and two or more orders of magnitude lower than most published


[*] This chapter has been published as "Dynamic capillary effects in a small-volume unsaturated porous medium: Implications of sensor response and gas pressure gradients for understanding system dependencies" by L. Hou, L. Chen and T. C. G. Kibbey in *Water Resources Research*, 2012.

values for similar porous medium/fluid combinations. Because of the small size of the experimental system used, results suggest that at the representative elementary volume (REV) scale, the dependence of measured capillary pressure on the rate of saturation change may not be as significant as previously thought for unsaturated systems. It is hypothesized that the larger magnitude of some previously-reported $\tau$ values may result at least in part from porous medium packing micro-heterogeneities that influence flow and pressure gradients in larger systems.

## 3.1 Introduction

The nonsteady state movement of multiphase fluids in porous media plays a central role in problems involving a wide range of systems. Examples of problems where the dynamics of saturation change may be important include enhanced oil recovery, geologic carbon sequestration, migration and remediation of nonaqueous phase liquids (NAPLs) in the subsurface, and infiltration/flooding phenomena in extreme weather events. Accurate modeling of these systems requires a quantitative understanding of the dynamic relationships between fluids in porous media undergoing saturation change.

The capillary pressure-saturation ($P_c$-$S$) relationship, also known as the soil-water characteristic curve or the water retention function, is an important constitutive relationship governing multiphase flow (Huyakorn and Pinder 1986; Muraleetharan and Wei 1999). Capillary pressure in a porous medium $P_c$ is defined as the pressure in the nonwetting phase minus the pressure in the wetting phase. In problems of multiphase flow or unsaturated flow, the wetting phase is typically defined as the phase through which contact angle (the angle between the fluid-fluid interface and the solid surface) is

less than 90 deg. In many natural porous media, water is the wetting phase, while air or organic liquid is the nonwetting phase. Wetting phase saturation $S$ is the fraction of the pore volume occupied by the wetting phase. The $P_c$-$S$ relationship describes the relationship between $P_c$ and $S$ in a medium. The relationship is hysteretic, in that the specific value of $P_c$ at a given $S$ depends on the wetting/drying path followed to reach that $S$.

$P_c$-$S$ relationships have historically been measured under static equilibrium conditions. Because of the dynamics of multiphase flow, particularly in fine porous media, it can take hours or even days for fluids to reach their equilibrium states during measurement steps. For this reason, experimental measurement of equilibrium $P_c$-$S$ relationships can require weeks or months to complete for some fine-grained porous media (Dane and Hopmans 2002). More than four decades ago it was observed that when $P_c$-$S$ relationships are measured more rapidly (i.e., where pressure is changed before equilibrium has been reached), the measured relationship differs from the static equilibrium $P_c$-$S$ relationship [e.g., (Topp *et al.* 1967; Smiles *et al.* 1971)]. This phenomenon has come to be referred to as a dynamic capillary effect.

Dynamic capillary effects refer to the observed flow rate dependence of fluid states in porous media experiencing dynamic drainage or imbibition. Besides capillary pressures, other phenomena that have been found to exhibit dynamic capillary effects include relative permeability (Stauffer 1978; Barenblatt *et al.* 2003), and the spatial distribution of fluids (Wildenschild *et al.* 2005). While it is probable that all of these observed phenomena are related, a comprehensive, quantitative understanding of dynamic capillary effects remains elusive. Dynamic capillary effects have been

observed by a number of well-designed experiments and studied by many theoretical analyses and modeling simulation efforts, but to date the observed and predicted system dependencies have been largely contradictory (Topp *et al.* 1967; Stauffer 1978; Wildenschild *et al.* 2001; Manthey *et al.* 2005; Oung *et al.* 2005; Wildenschild *et al.* 2005; Camps-Roach *et al.* 2010; Sakaki *et al.* 2010; Bottero *et al.* 2011b; Goel and O'Carroll 2011; Civan 2012; Das and Mirzaei 2012). Proposed mechanisms of dynamic capillary effects have included dynamic contact angles (Weitz *et al.* 1987; Friedman 1999), dynamic interface deformation (Weitz *et al.* 1987; Kalaydjian 1992), dynamic fluid spatial distribution (Wildenschild *et al.* 2001; Barenblatt *et al.* 2003; Wildenschild *et al.* 2005), and the effects of averaging homogeneous/heterogeneous flow zones (Bourgeat and Panfilov 1998; Dahle *et al.* 2005; Gielen *et al.* 2005).

Several quantitative relationships have been proposed to describe the effect of dynamic saturation change on capillary pressure (Stauffer 1978; Hassanizadeh and Gray 1990; Kalaydjian 1992; Hassanizadeh and Gray 1993a; Hassanizadeh and Gray 1993b; Hassanizadeh *et al.* 2002; Barenblatt *et al.* 2003). Most use a proportionality constant to relate the difference between dynamic and statically measured $P_c$-$S$ relationships to some measure of the rate of saturation or pressure change. Among these equations, the equation presented by Hassanizadeh and Gray (1993a) is one of the more widely used in the recent published literature. Based on thermodynamic theories and constitutive conservation laws, Hassanizadeh and Gray (1993a) derived Eq. 3.1:

$$P_c^d - P_c^s = -\tau \cdot \frac{\partial S}{\partial t} \qquad \text{(Eq. 3.1)}$$

where $P_c^s$ is the pressure difference between nonwetting and wetting phases within a porous medium under static (no flow) conditions (the true, or static capillary pressure),

and $P_c^d$ is the observed pressure difference between nonwetting and wetting phases within a porous medium under conditions where saturation is dynamically changing (the dynamic capillary pressure). It should be noted that some authors (e.g., (Bottero *et al.* 2011b)) have recently argued against the use of the term 'dynamic capillary pressure' as it does not represent a true capillary pressure; we adopt this widely-used terminology in the interest of concise discussion. It must be recognized, however, that $P_c^d$ is not a true capillary pressure, but simply an observed pressure difference between phases under specific flow conditions. The parameter $\tau$ in Eq. 3.1, the dynamic capillary coefficient, is a measure of the magnitude of dynamic effects on measured capillary pressure. Larger values of $\tau$ correspond to a greater difference between $P_c^d$ and $P_c^s$ for a given rate of saturation change.

Although a number of values of $\tau$ have been published, both from experimental and modeling studies, considerable uncertainty exists as to both its magnitude, and to how it is influenced by system properties. Published studies have reported values of $\tau$ for similar materials that differ by orders of magnitude. Based on eight published studies of dynamic effects dating from 1967 to 1998, Hassanizadeh *et al*. (2002) calculated approximate values of $\tau$. Of the eight studies, seven involved drainage measurements in sands for air-water systems. However, despite the similarities in the porous media and fluids used, values ranged from $3\times10^4$ to $5\times10^7$ Pa·s – a range of more than three orders of magnitude. More recent experimental studies in both air-water and organic liquid-water systems (e.g., (O'Carroll *et al.* 2005; Oung *et al.* 2005; Camps-Roach *et al.* 2010; Sakaki *et al.* 2010; Bottero *et al.* 2011b; Goel and O'Carroll 2011; Das and Mirzaei 2012)) have generally fallen within this range, but show little

consistency between studies in terms of the effect of system properties (fluids, porous media) on magnitude of $\tau$, how $\tau$ varies with saturation, or how it differs between drainage and imbibition. For example, Sakaki *et al*. (2010) report air-water drainage $\tau$ values for a fine sand that increase with decreasing saturation, reaching a value of approximately $10^7$ Pa·s at a saturation of 0.4. In contrast, Camps-Roach *et al*. (2010) report air-water drainage $\tau$ values for two similar sands which *decrease* with decreasing saturation, reaching a value of approx. $4\times10^5$ Pa·s at S~0.6 – the opposite trend from that reported by Sakaki *et al*. (2010), and values one to two orders of magnitude lower. Furthermore, some authors have presented evidence suggesting that $\tau$ is higher for finer porous media (e.g., (Stauffer 1978; Wildenschild *et al.* 2001; Camps-Roach *et al.* 2010; Das and Mirzaei 2012)), while others have presented evidence that it is lower (e.g. (Oung *et al.* 2005)).

The overarching objective of this work was to explore dynamic capillary effects during drainage in unsaturated systems, with specific emphasis on understanding how $\tau$ varies with saturation and system properties during drainage. Two key differences between this work and earlier published studies are (1) this work makes use of extremely small (1.27 cm high) packed cells for measurements, and (2) all results include quantitative consideration of the effects of temporal sensor response and gas pressure gradients on calculated $\tau$ values.

The use of a small packed cell eliminates larger-scale microheterogeneities that can occur in laboratory packing of porous media in larger columns, and also physically limits the spatial range of sensors used for determining fluid pressures. Bottero *et al.* (2011b) presented calculations showing that volume averaging of point measurements

could produce measured $\tau$ values an order of magnitude higher than point measurements, a result that suggests that the spatial range of sensors used to make the measurements could potentially impact the resulting measured $\tau$ values. Most published experimental work examining dynamic effects has used packed columns ranging in height from approximately 10 cm (e.g. (Sakaki *et al.* 2010; Bottero *et al.* 2011b)) to more than 50 cm (e.g., (Smiles *et al.* 1971; Stauffer 1978)). In contrast, the cells used here have a height almost an order of magnitude smaller than most of the smallest columns used to date.

Furthermore, it was hypothesized that the dynamics of both sensor response and gas pressure gradients could influence measured $\tau$ values by mimicking dynamic capillary effects under some conditions. As such, corrections for these potential artifacts are calculated for all experiments and their magnitudes explored.

## 3.2 Materials and Methods

### *3.2.1 Materials*

Two different unconsolidated porous media were used in this work: US Silica (Berkeley Spring, WV) F-95 Ottawa fine sand, and Scientific Industries (Bohemia, NY) SI-BG05 coarse glass beads. The properties of F-95 sand and glass beads are shown in Table 3.1. Properties of the F-95 sand are taken from Chen *et al.* (2007). Due to the extremely high permeability of the coarse SI-BG05 glass beads accurate measurement of permeability was not possible with our system (system conductivity is orders of magnitude lower than the glass beads themselves), so permeability of the glass beads was estimated using the Kozeny-Carman equation (Bear 1972). The two media were selected due to their extremely different $d_{50}$ values, and correspondingly different

capillary behavior. Prior to use, media were rinsed at least two times with deionized water to remove fines, and then oven dried.

Two different wetting phases were used to explore the effects of wetting phase viscosity on dynamic capillary effects: Nanopure (Barnstead; Dubuque, IA) water, and a 35% w/v sucrose solution prepared with Nanopure water and standard table sugar. All experiments conducted for this work were conducted in unsaturated, gas-liquid systems, with gas as the nonwetting phase. The nonwetting phase in this study was high purity (≥ 99.99%) compressed nitrogen. Properties of all three fluids are given in Table 3.1. Viscosity and density of the sucrose solution were measured for this work, and are consistent with reported literature values.

**Table 3.1. Properties of porous media and fluids used in experiments** [a]

| Medium | $d_{50}$ (mm) | *Permeability* $\kappa$ ($cm^2$) |
|---|---|---|
| F-95 Sand | 0.140 | $2.27 \times 10^{-8}$ |
| SI-BG05 Glass Beads | 0.500 | $1.88 \times 10^{-6}$ |
| **Fluid** | $\rho$ ($kg/m^3$) | $\mu$ (cP) |
| Water | 998 | 1.002 |
| Sucrose soln. (35% w/v) | 1154 | 3.5 |
| Nitrogen (g) | 1.165 | 0.0178 |

[a] Fluid properties correspond to 20°C, atmospheric pressure.

### *3.2.2 System description*

All experiments were conducted using an automated system modified from systems previously described by Chen and Kibbey (2006) and Chen *et al.* (2007). The system makes use of a small volume, membrane-based soil cell for rapid control and measurement of capillary pressure and saturation in unconsolidated media. The system uses a computer-controlled servo-pressure regulator (type 3110, Marsh Bellofram,

Newell, WV) to apply time-varying gas pressures to the top of the soil cell. Experiments start with a known liquid saturation in the cell (typically fully-saturated), and as liquid drains from the cell it is collected in a vertical glass tube, where its volume is determined in real time from hydrostatic pressure. Saturation is calculated based on the known initial saturation and volume of liquid in the vertical glass tube. Full details of underlying system design and operation are provided by Chen *et al.* (2007).

Figure 3.1 shows a diagram of the soil cell as modified for this work. The internal dimensions of the soil cell are 1.27 cm (height) × 2.54 cm (diameter) (a total internal volume of 6.44 mL, and a pore volume on the order of 2.3 mL, depending on porosity). A nylon membrane with a 20 μm pore size was used at the bottom of the cell as a water-wet capillary barrier, and a PTFE membrane with a 0.22 μm pore size was used at the top of the cell as a hydrophobic capillary barrier. Nylon membranes were purchased from GE Osmonics, Inc. (Minnetonka, MN), while PTFE membranes were purchased from Membrane Solutions (Plano, TX).

For this work, two custom-designed fluid-selective pore pressure microsensors were integrated into the soil cells (Figure 3.1). The sensors are based on commercial pressure transducers (PX481A or PX181, Omega Engineering, Inc., Stamford, CT), and are operationally similar to the sensors used by Bottero *et al.* (2011b). The commercial transducers connect to internal tubes which extend 3.5 mm into the interior of the cell. At the end of the tubes, 3.2 mm diameter countersunk #80 mesh stainless steel screens support fluid-selective membranes, which are glued in place with contact cement. For measurement of wetting phase pressures, nylon hydrophilic membranes with a pore size of 20.0 μm were used. For measurement of gas pressures, PTFE membranes with a pore

size of 0.22 μm were used. For both types of measurement, the dead volume between the screen and the commercial pressure transducer was filled with degassed water and flushed through integrated drains to eliminate any gas behind the membranes. The reason for this is that for the microsensors to respond to a pressure change, a small amount of fluid must pass through the membrane for the fluid pressure to be registered by the commercial pressure transducer. Because of the high compressibility of gas, the presence of any gas behind the membrane can significantly slow the response of a fluid-selective pore pressure microsensor; this effect can be very significant with the fast sensors used for this work. For this reason, water was included behind the membrane even in sensors intended to measure gas pressures.

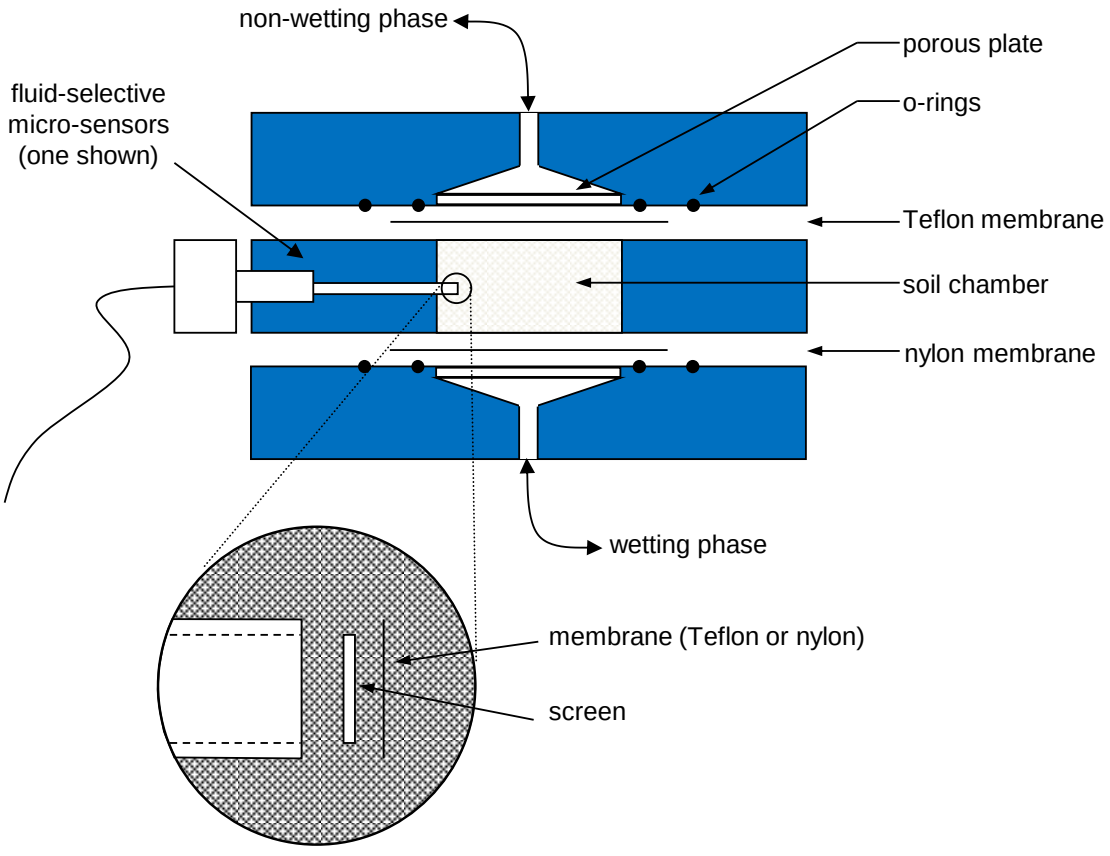


**Figure 3.1. Exploded side view of soil cell with fluid-selective pore pressure microsensor. Second microsensor and microsensor drains not shown.**

Applied pressures were controlled by adjusting voltage to the servo-pressure regulator at 0.1 s intervals using a Measurement Computing (Middleboro, MA) PCI-DDA08/12 8-channel D/A board. Data from all sensors was acquired using a Measurement Computing PCI-DAS6034 A/D board. Data was read continuously at a rate of 12,288 samples $s^{-1}$ per channel, and then continuously averaged over the most recent 1 s interval to smooth electronic noise. Data were recorded at 0.1 s intervals. For calculations involving data collected at different rates, all measurements were interpolated to saturation intervals of 0.001 (0.1%). All derivatives were calculated using central differences over a saturation window of $\pm 0.02$ (2%) about the desired saturation.

### *3.2.3 Experimental procedures*

Cells were wet-packed following procedures described by Chen *et al.* (2007). A nylon membrane was initially placed on the top of the cell to allow degassed water to be flushed through the cell to dissolve any remaining trapped gas. Cells were flushed for approximately 15 pore volumes at a flow rate of 1 mL $min^{-1}$. Water flushed through the column was directed out of the bottom of the cell for the first approximately 5 pore volumes, and the remainder was directed out of the drains for the water-phase pore pressure microsensor(s).

Following flushing, the top membrane was replaced with a PTFE membrane, and the response of the water-phase pore pressure microsensor was measured by closing the valve below the cell to prevent water flow, and then introducing a rapid pressure signal to the gas above the cell. Because there was no flow out of the cell, the change in

applied gas pressure above the cell was transmitted directly to the water. Sensor response was found to be very well described by a first-order relationship (Eq 3.2)

$$\frac{\partial P_s}{\partial t} = k(P - P_s) \qquad \text{(Eq. 3.2)}$$

where $P_s$ is the pressure as detected by the sensor, $P$ is the applied pressure of the phase of interest, and $k$ is the first order rate constant describing sensor response. It should be noted that while the fluid-selective microsensors used in this work are used under positive pressures, their function is fundamentally the same as that of conventional tensiometers. Tensiometer response has been widely studied, and the first order response described by Eq. 3.2 has been observed for more than 60 years (e.g. (Richards 1949; Klute and Gardner 1962; Towner 1980)). The constant $k$ in Eq. 3.2 is expected to be a function of both the porous medium and the sensor, although for media with sufficiently-high permeabilities, sensor capillary barrier permeability dominates sensor response (e.g. (Klute and Gardner 1962; Towner 1980; Selker *et al.* 1992)). Measurements of gas phase sensor response were conducted separately on dry media. Note that separate preliminary tests with both types of sensors found no systematic variation in k over a wide range of saturations, with the exception of the gas sensors, which when initially wet (i.e., at the start of each drainage cycle) typically did not respond to external pressure changes until the pressure difference across the PTFE membrane reached approximately 60-70 cm water; this effect may be due to the rough surface of the PTFE membranes used, or water interaction with the polypropylene lamination, but was not found to impact rapid sensor response at the higher pressures. Note that the near-constant water sensor response with changing saturation observed here is consistent with a sensor whose response is not limited by the porous medium

over the saturation range studied since decreasing conductivity with decreasing saturation would be expected to produce slower response at lower saturations in a porous medium-limited sensor (e.g. (Selker *et al.* 1992)).

Figure 3.2 illustrates the measurement of sensor response for three different water-phase sensors. The applied pressure in Fig. 3.2 corresponds to a 210 cm water ($2 \times 10^4$ Pa) change produced by a voltage step to the servo-pressure regulator. Because the system cannot produce an instantaneous pressure step of this magnitude, and because of the 1 s averaging smoothing used for noise reduction during all data acquisition (Sec. 3.2.2), the measured applied pressure (Fig. 3.2) is used in place of a theoretical step input to calculate sensor response rate constants. (Note that the use of the same averaging smoothing for both the applied and sensor signals means that the resulting calculated sensor response constants are not impacted by the smoothing.) It should be noted that the sensors in Fig. 3.2 respond extremely quickly compared with conventional tensiometers or ceramic-based fluid-selective sensors. For comparison, the sensors used by Camps-Roach *et al.* (2010) reached 95 % of their final value in response to a step input after 120 s in unsaturated conditions, corresponding to a first order constant of ~0.025 $s^{-1}$. Both Bottero *et al.* (2011b) and Sakaki *et al.*(2010) report that their fluid-selective pressure sensors responded to pressure changes faster than those in Fig. 3.2, but they don't provide detailed rate information. From a practical standpoint, it can be difficult to accurately determine rate constants for sensors with *k* faster than ~4 $s^{-1}$, simply because it is difficult to create a rapid enough input pressure change. Note that the differences in the three sensors in Fig. 3.2 likely result from slight differences in the amount of glue used to attach the membranes, and may also result

from small air bubbles trapped in the dead volume between the membrane and the transducer. Other factors that can influence sensor response include fluid viscosity (higher viscosity fluids produce slower response) and membrane permeability (low permeability membranes produce slower response).

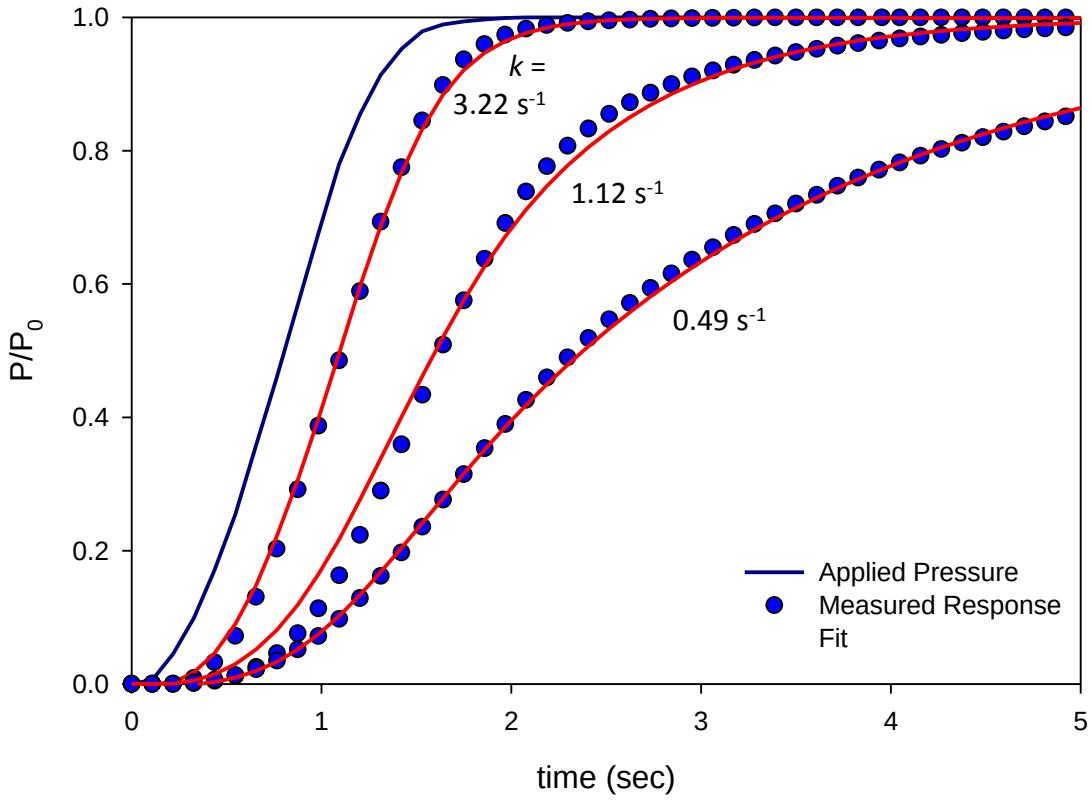


**Figure 3.2. Water sensor response for three different membrane-based sensors. Numbers correspond to sensor first-order response rate constants (*k*; Eq. 3.2)**

Following characterization of water-phase microsensor response, dynamic experiments were conducted as follows. All experiments made use of ramped pressure inputs, both for imbibition and drainage. For all porous media, a slow pressure ramp (approximately 0.05 cm water $s^{-1}$) was used to produce primary drainage and main imbibition. After main imbibition, a total of seven secondary drainage/imbibition cycles were performed, with drainage rates increasing from ~ 0.1 to ~7.5 cm water $s^{-1}$ (exact

values varied slightly depending on which servo-pressure regulator was used). Imbibition after each secondary drainage was conducted at a slow 0.1 cm water $s^{-1}$ rate. After each drainage and imbibition, pressure was held constant for 20 s to allow for any additional equilibration of fluids between cycles. Calculations exploring dynamic capillary effects were conducted using pressure measurements made during the secondary drainages. The inherent assumption of this approach is that the water configuration at the start of each drainage is essentially the same, regardless of previous cycles. This assumption is supported by the fact that the starting saturation for each secondary drainage was nearly the same for all experiments (within approximately 2%). Furthermore, preliminary experiments conducted with decreasing (fast to slow) instead of increasing (slow to fast) pressure rates produced results that were virtually identical to those presented here, providing confidence in the approach and the results.

A total of three different experiments were conducted for the work: two in F-95 sand (one with water, one with sucrose solution), and one in coarse glass beads with water (Table 3.2). All experiments made use of two fluid-selective pore pressure microsensors. One experiment (Expt. 1, F-95/water) included one water-phase microsensor and one gas-phase microsensor, while the other two experiments each included two water-phase microsensors, each with a different response rate. All experiments were conducted at room temperature (approximately 22 $\pm$ 1 ℃)

### *3.2.4 Calculations*

To better understand the impact of potential measurement artifacts on the calculation of $\tau$, we explore the magnitudes of quantitative corrections for sensor response, as well as pressure drop in the column due to gas flow. Corrections are used

to calculate estimates of true (corrected) pressures inside the cell based on either measured sensor or influent pressures.

**Table 3.2. Experiment conditions and sensor response rate constants.**

| Expt. No. | Medium | Wetting Fluid | Porosity, n | $P_g$ max (cm water) | Cycles ($2^o$ dr.) | Sensor rate constants ($s^{-1}$) | | |
|---|---|---|---|---|---|---|---|---|
| | | | | | | $k^g$ | $k^w$-A | $k^w$-B |
| 1 | F-95 Sand | Water | 0.36 | 190 | 7 | 3.0 | 3.2 | --- |
| 2 | F-95 Sand | Sucrose Soln. | 0.36 | 198 | 7 | --- | 0.59 | 0.40 |
| 3 | SI-BG05 Glass Beads | Water | 0.37 | 140 | 7 | --- | 1.12 | 0.49 |

Correction from sensor response is made using Eq. 3.3 (a rearrangement of Eq. 3.2):

$$P^i_{corr.(sens.)} = \frac{1}{k^i}\frac{\partial P^i_s}{\partial t} + P^i_s \qquad \text{(Eq. 3.3)}$$

where $P^i_{corr.(sens.)}$ is the estimated true pressure in the cell for phase *i* (water or gas). Because all of the items on the right hand side are known, it is possible to calculate $P^i_{corr.(sens.)}$ at every experimental time step. Note that this correction is identical to the approach described by Klute and Gardner (1962) for dynamic correction for tensiometer response. The impact of this correction is greatest for systems with slower sensors, and where rates of pressure change are greatest.

Correction for gas flow is made to better understand the impact of using influent gas pressures on calculation of $\tau$. Others have made measurements based on the assumption that gas can be considered infinitely mobile in the column. However, it was hypothesized that for some systems this assumption may not be satisfied. To correct for pressure drops in the gas, we ignore compressibility and assume that volumetric gas

flow into the cell is equal to volumetric water flow out of the cell, and then use Darcy's law to estimate the pressure drop between the top of the cell and the vertical midpoint of the cell (the location of the fluid-selective pore pressure microsensors) (Eq. 3.4):

$$P^{g}_{corr.(flow.)} = P^{g}_{inlet} - \frac{q_w L}{\kappa k_{rnw}(S)} \frac{\mu_g}{\rho_w g} \quad \text{(Eq. 3.4)}$$

where $P^{g}_{corr.(flow.)}$ and $P^{g}_{inlet}$ are the estimated true pressure in the cell and the measured inlet gas pressure at a given experimental time step, both in units of height of water ($\rho_w g$ converts the pressures to water height units). The Darcy velocity of water leaving the cell is given by $q_w$, the distance from the inlet of the cell to the vertical midpoint is $L$ (6.35 mm in this case), the permeability of the medium and gas viscosity are $\kappa$ and $\mu_g$, respectively (Table 3.1). Relative permeability of the nonwetting phase ($k_{rnw}$) was calculated using the relationship described by Brooks and Corey (1966) (a relationship that has been found to provide very good estimates of $k_{rnw}$ (e.g., (Fischer *et al.* 1997)):

$$k_{rnw} = (1 - Se)^2\left(1 - Se^{(1+(2/\lambda))}\right) \quad \text{(Eq. 3.5)}$$

where $Se$ is effective saturation ($Se = (S - Swr)/(Snwr - Swr)$, where $S_{nwr}$ is water saturation corresponding to nonwetting phase residual), and $\lambda$ is the pore size distribution index from the Brooks-Corey fit to the capillary pressure-saturation relationship. Eq. 3.4 can be considered approximate, and is most appropriate for a very small cell, where saturation can be expected to be near uniform at all but the highest saturations, particularly during secondary drainage; corrections in longer columns would require a more complex approach taking into account vertical gradients in saturation (and, as a result, gradients in gas permeability). The impact of the correction

described by Eq. 3.4 is greatest for systems with low permeabilities, but over saturation ranges where flow rates are high.

***Dynamic capillary pressures.*** Calculation of τ (Eq. 3.1) requires values of dynamic capillary pressure at each saturation where the calculation is conducted. For this work we define four different dynamic capillary pressures based on the corrections described in Eq. 3.3 and 3.4. Table 3.3 provides the definitions of the four dynamic capillary pressures. In cases where a second water phase sensor is used in place of a gas phase sensor (Expts. 2 and 3 (Table 3.2)), $P_c^d$-1 and $P_c^d$-1$^*$ are calculated for each of the two sensors, and are identified with A or B, to match the sensor designations in Table 3.2.

**Table 3.3. Definitions of the four different dynamic capillary pressures ($P_c^d = P_g^d - P_w^d$) used in calculations.**

| $P_c^d$ | Gas Pressure ($P_g^d$) | | | | Water Pressure ($P_w^d$) | |
|---|---|---|---|---|---|---|
| | Influent Gas Pressure | | Gas micro-sensor | | Water micro-sensor | |
| | Uncorrected | Corrected (Eq. 3.4) | Uncorrected | Corrected (Eq. 3.3) | Uncorrected | Corrected (Eq. 3.3) |
| $P_c^d$-1 | X | | | | X | |
| $P_c^d$-1$^*$ | | X | | | | X |
| $P_c^d$-2 | | | X | | X | |
| $P_c^d$-2$^*$ | | | | X | | X |

***Calculation of $\tau$.*** To calculate the dynamic capillary coefficient $\tau$, we rearrange Eq. 3.1 into Eq. 3.6:

$$P_c^d(S)|_j = -\tau(S) \cdot \frac{\partial S}{\partial t}(S)\Big|_j + P_c^s(S) \qquad \text{(Eq. 3.6)}$$

where the index *j* corresponds to data from a drainage curve conducted at a specific rate. Based on Eq. 3.6, it is apparent that plots of $P_c^d(S)$ vs $\frac{\partial S}{\partial t}(S)$ at a given saturation should give a linear relationship, with a slope equal to $-\tau(S)$ and an intercept equal to the static capillary pressure $P_c^s(S)$. Because the experiments conducted for this work do not involve direct measurement of $P_c^s$, Eq. 3.6 is used to measure $\tau$ based on the data from seven dynamic drainage curves. A program specifically written for the purpose conducts regressions across all saturations (at 0.001, or 0.1% saturation increments). The program also calculates standard error of the regression at each saturation. Calculated values of $\tau$ are reported as $\tau_1$, $\tau_1*$, $\tau_2$, $\tau_2*$, depending which $P_c^d$ value (Table 3.3) are used in the calculation.

## 3.3 Results and Discussion

### *3.3.1 F-95 sand/Water*

Figure 3.3 shows both the time evolution of saturation (dotted lines) and calculated $\frac{\partial S}{\partial t}$ as a function of saturation for the F-95 sand/water system (Expt. 1). Results shown correspond to seven secondary drainage curves conducted at ramped gas pressure rates spanning almost two orders of magnitude (~0.1 to ~7.6 cm water $s^{-1}$). Each curve corresponds to drainage that occurs during each ramp up to the specified maximum gas pressure (190 cm water in this case (Table 3.2)). These experimental conditions produce drainage curves that take between ~20 and 1000 s to complete, and maximum rates of saturation change ($\frac{\partial S}{\partial t}$) that vary from approximately -0.0013 $s^{-1}$ for the slowest drainage to -0.03 $s^{-1}$ for the fastest curve.

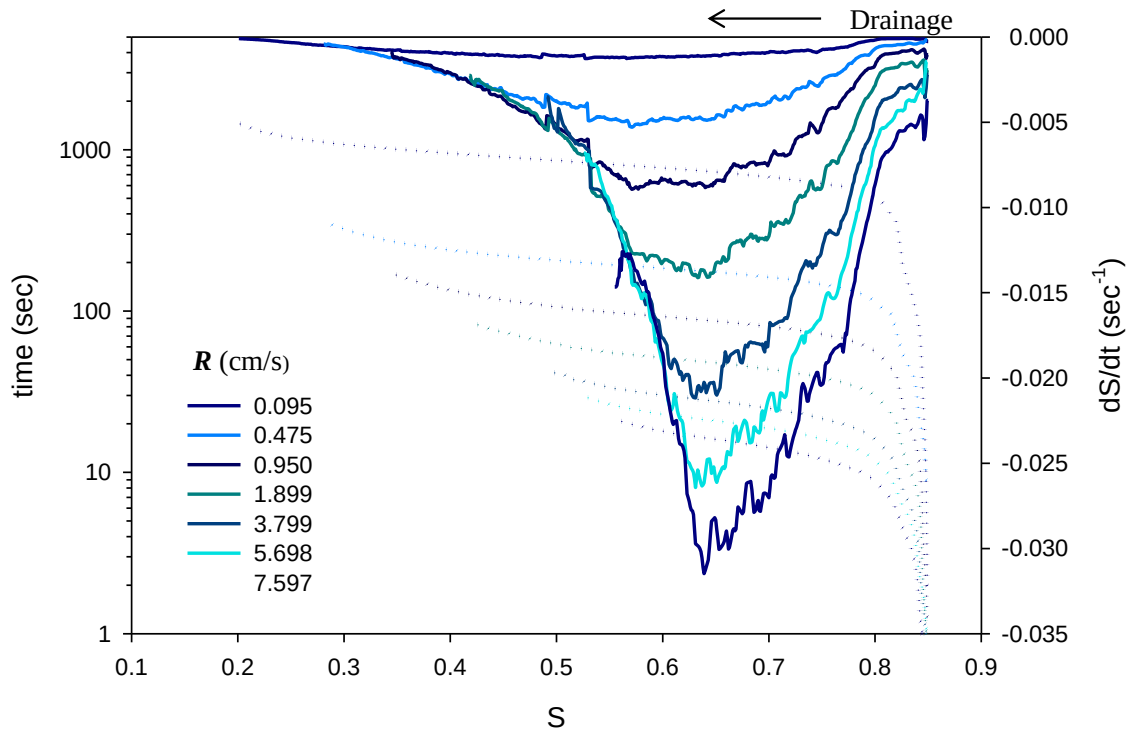


**Figure 3.3. $\partial S/\partial t$ (solid lines) and elapsed time (dotted lines) for drainage at different applied ramped gas pressure rates ($R$). Curves correspond to secondary drainages of F-95 sand initially saturated with water (Expt. 1).**

Figure 3.4 shows the uncorrected pressures for the F-95 sand/water system (Expt. 1) measured in the influent gas (solid lines) and by the water phase pore pressure microsensor (dotted lines) for the same seven drainage curves. Note that the use of a ramped pressure input with this system produces a case where both water and gas pressures increase during drainage. The flow-through system used by Bottero *et al.* (2011b) produces a similar result during the measurement process, with the pressures in both phases increasing with decreasing saturation. In contrast, the system used by Camps-Roach *et al.* (2010) (and others like it which use a constant gas pressure or water vacuum input) produces constant gas pressure and decreasing water pressures with decreasing saturations. In cases where temporal sensor response impacts measured

dynamic capillary effects, it is likely that the direction of pressure change is significant, as a lagging sensor will over- or under-predict pressures, depending on the direction of the lag.

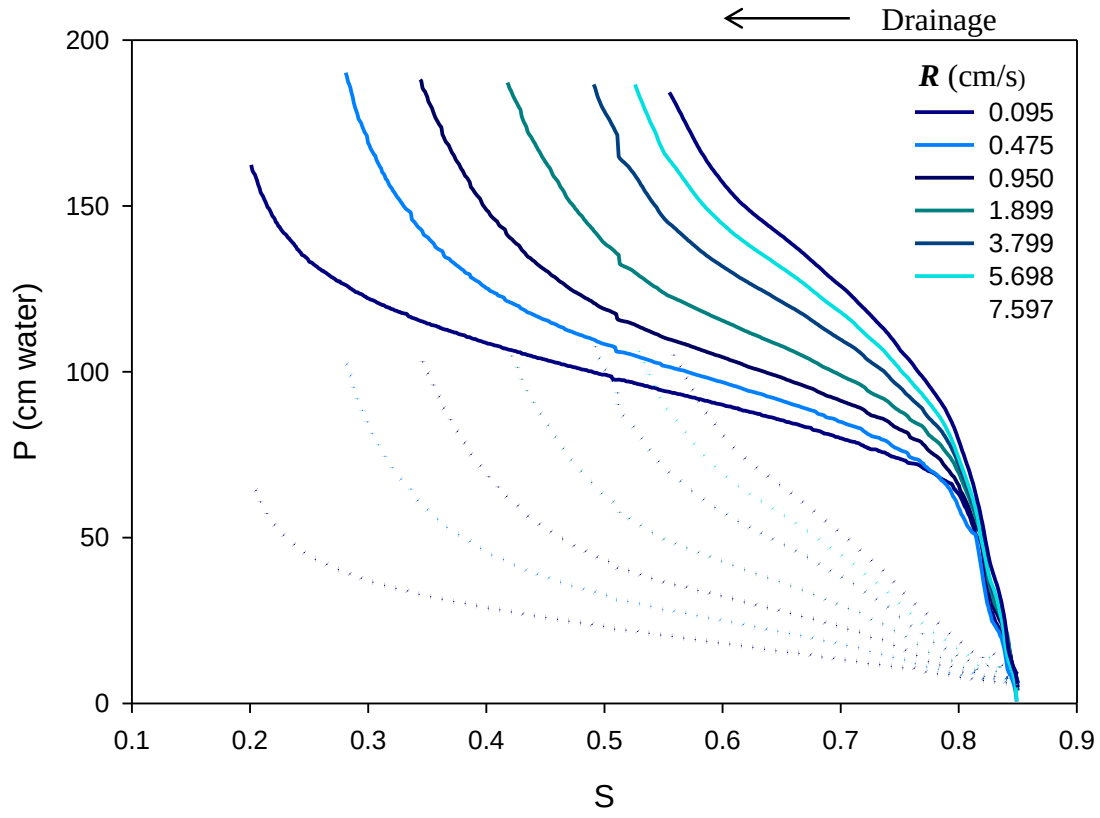


**Figure 3.4. Inlet gas pressures (solid lines) and measured water pressures (dotted lines) for drainage at different applied ramped gas pressure rates (*R*). Curves correspond to secondary drainages of F-95 sand initially saturated with water (Expt. 1).**

Figure 3.5 shows measured dynamic capillary pressures for the F-95 sand/water system (Expt. 1), calculated based on the definitions in Table 3.3. For comparison, apparent capillary pressures (the pressure difference between phases across the cell inlet and outlet) are also shown as an inset (Figure 3.5E, dotted lines). Note that apparent

capillary pressures are much greater than the other pressures because they include the pressure gradient in the water phase that results from flow.

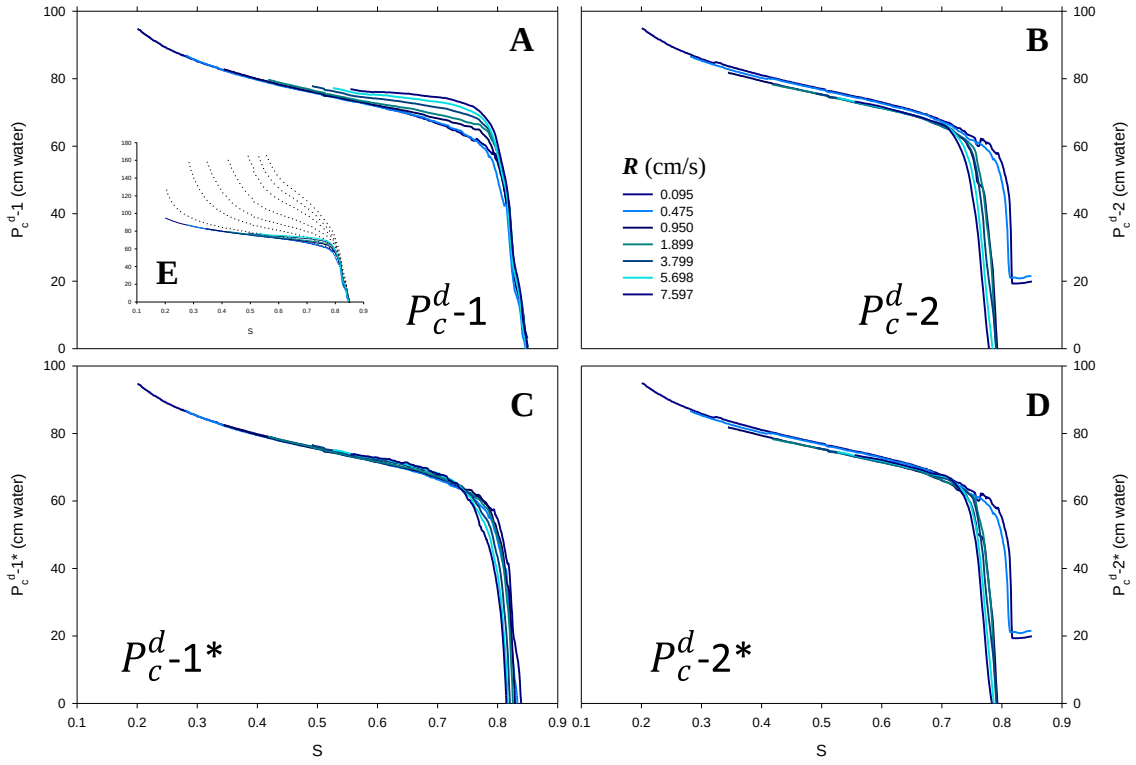


**Figure 3.5. (A and B) Uncorrected, (C and D) corrected, and (E) apparent dynamic capillary pressures, calculated based on the definitions in Table 3.3. Curves correspond to secondary drainages of F-95 sand initially saturated with water (Expt. 1).**

Figures 3.5A and B correspond to dynamic capillary pressures calculated based on uncorrected pressures. The dynamic capillary pressure based on influent pressure ($P_c^d$-1, Fig. 3.5A) looks like many (but not all) of the published dynamic capillary pressure curves from the past four decades, in that the curves deviate from one another to the greatest extent at higher saturations, but converge on a single curve at lower saturations (e.g., (Topp *et al.* 1967; Smiles *et al.* 1971; Vachaud *et al.* 1972; Stauffer 1978; Kalaydjian 1992; Bottero *et al.* 2011b)). In contrast, the dynamic capillary

pressure based on the two uncorrected internal sensors ($P_c^d$-2, Fig. 5B) shows very little difference between any of the curves, except at the highest saturations, where no gas sensor response is observed at the start of drainage. (As mentioned previously, measurements show that the gas sensors used for Expt. 1 do not respond until gas pressure difference across the PTFE membrane exceeds approximately 60-70 cm water.)

Figures 3.5C and D show corrected dynamic capillary pressures calculated using the corrections described in Eqs. 3.3 and 3.4. Examination of both figures shows that the corrected values come very close to collapsing onto the same curve. This is particularly notable for $P_c^d$-1* (Fig. 3.5C), given how far apart the $P_c^d$-1 curves were in Fig. 3.5A. Note that the magnitude of the correction in Fig. 3.5C can be attributed approximately 40% to water sensor response, and 60% to gas flow, when considered at S=0.7. However, the relative magnitudes of the two corrections differ at different saturations, with the flow correction decreasing monotonically with decreasing saturation (as a result of increasing gas permeability), and the sensor correction remaining relatively constant over much of the saturation range after an initial increase at high saturations.

In the case of $P_c^d$-2* (Fig. 3.5D), while the curves do come very close to collapsing on one another, there is little difference from the uncorrected $P_c^d$-2 (Fig. 3.5B). It is important to note that this situation is entirely due to the fact that the two sensors in this case happen to be very closely matched ($k^w$=3.2 $s^{-1}$, $k^g$=3.0 $s^{-1}$). That means that sensor lag in each of the two phase pressures essentially cancels the other out, causing uncorrected $P_c^d$-2 curves to closely approximate corrected $P_c^d$-2* curves. It

is important to emphasize, however, that any mismatch in sensor response could potentially cause significant differences. For example, even though both sensors are extremely fast ($k$=3.0 $s^{-1}$ corresponds to a 50% response to a stepped input in approx. 0.2 s), if one of the two were infinitely fast, the fastest uncorrected curve in Fig. 3.5D would shift up or down by approximately 3 cm water, depending on which sensor had the instantaneous response. Similarly, if one of the two sensors were much slower than the other (e.g., due to viscosity differences), the differences in measured $P_c^d$-2 curves could be much more significant.

As mentioned previously, calculation of $\tau$ is done by regression of Eq. 3.6 at 0.001 saturation intervals. Figure 3.6 illustrates the regression at three specific saturations for the F-95 sand/water system (Expt. 1), for calculation of $\tau_1$ from $P_c^d$-1 (separate regressions are conducted for each of the four different dynamic capillary pressures (Table 3.3)).

The results of regressions are shown in Figure 3.7. Note that error bars in Fig. 3.7 correspond to the standard error of the regression slope ($-\tau$) at each saturation. As such, it is important to emphasize that error bars are primarily a measure of the uncertainty of $\tau$ resulting from the regression itself (i.e., deviation from linearity), rather than a comprehensive indication of uncertainty in $\tau$.

From Fig. 3.7, it is apparent that $\tau_1$, the dynamic capillary coefficient calculated from uncorrected influent pressure and uncorrected water sensor pressure (i.e., $P_c^d$-1), has the greatest magnitude, approaching $10^5$ Pa·s at high saturations. It is also apparent that $\tau_1$ exhibits a decreasing trend with decreasing saturation; this trend is almost entirely attributable in this system to the use of influent gas pressure, because the

difference between influent gas pressure and pressure at the midpoint of the porous medium decreases with decreasing saturation. However when pressures are corrected for gas flow and water sensor response (i.e., $P_c^d$-1*), the corresponding dynamic capillary coefficient ($\tau_1 *$) is considerably lower, exhibiting a relatively constant magnitude of ~$5\times10^3$ Pa·s over much of the saturation range. Note that $\tau_1 *$ is actually calculated to be negative at the highest saturations; this is the result of the simplified gas flow correction (Eq. 3.4) over-predicting the correction for gas flow pressure drop at high saturations, causing inversion of $P_c^d$-1* curves at high saturations (Fig. 3.5C).

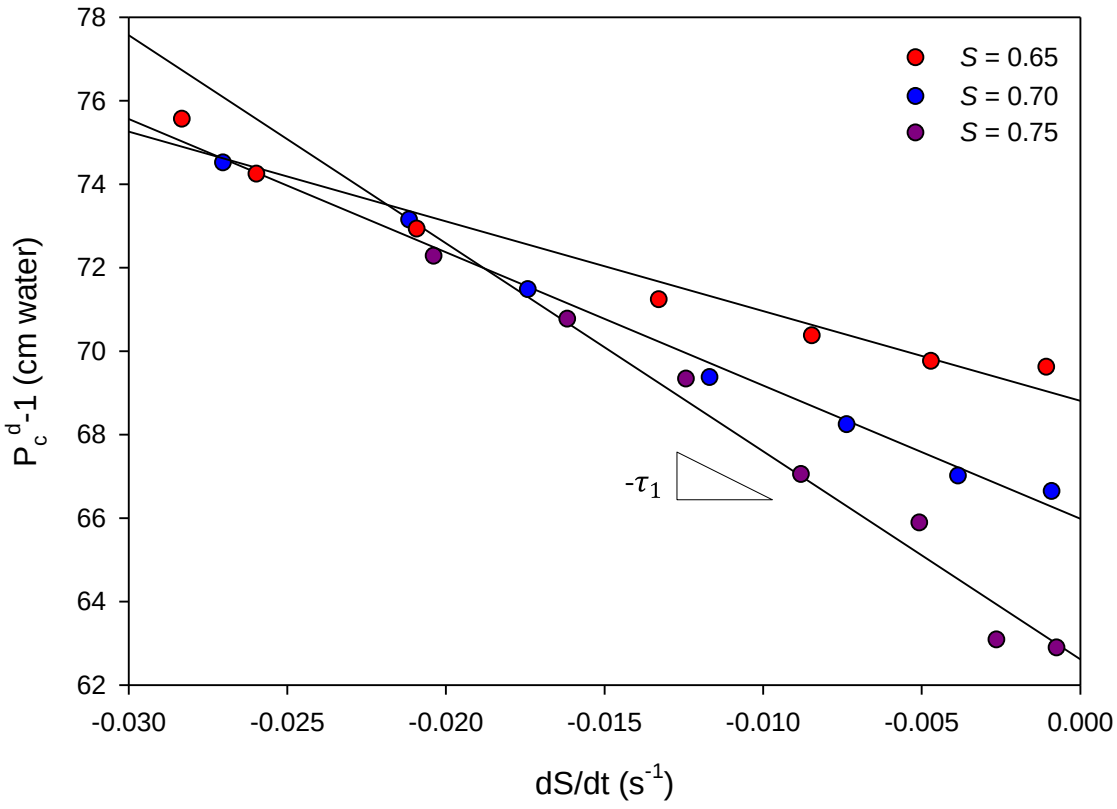


**Figure 3.6. Illustration of regressions used to determine $\tau$ values, shown for three saturations for F-95 sand initially saturated with water (Expt. 1). Actually analyses involve regressions at saturation intervals of 0.001.**

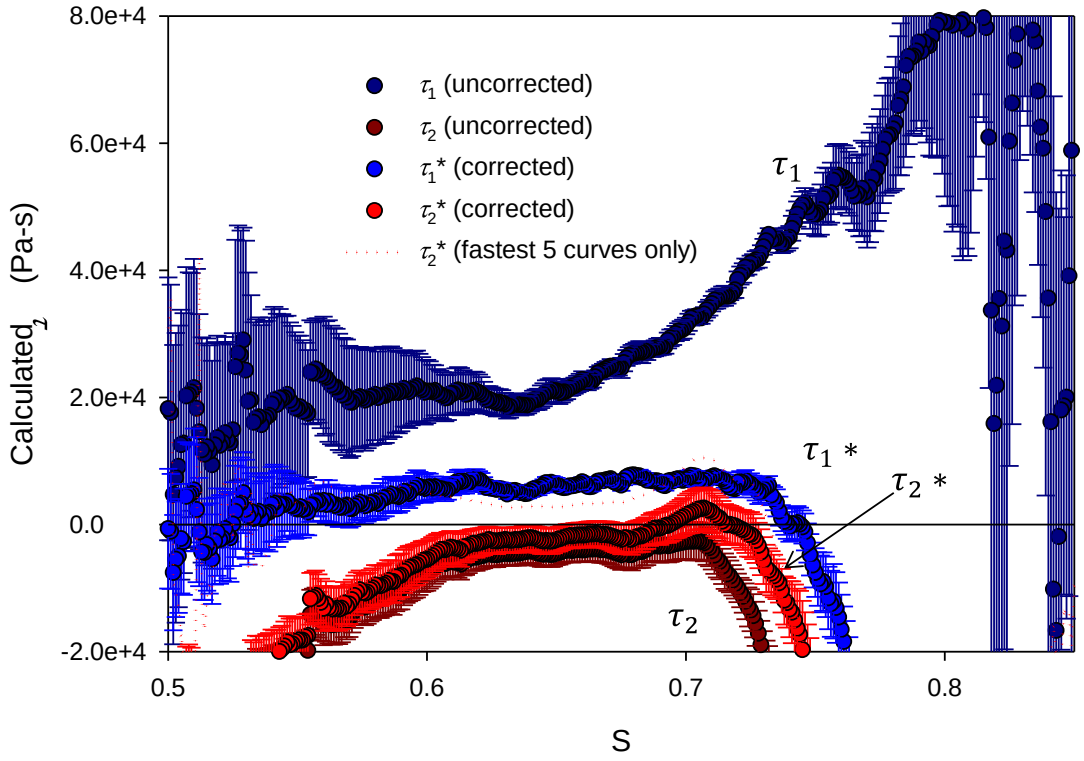


**Figure 3.7. Calculated uncorrected and corrected $\tau$ values for F-95 sand initially saturated with water (Expt. 1). Values correspond to the definitions of $P_c^d$ in Table 3.3. Error bars correspond to standard error of the regression at each saturation.**

Calculated values for $\tau_2$ and $\tau_2 *$ shown in Fig. 3.7 are very similar to one another. This might be expected because of the similarities between the corresponding dynamic capillary pressures used in their calculation ($P_c^d$-2 and $P_c^d$-2*, Figs. 3.5B and D). Because the gas sensor does not respond at high saturations (Fig. 3.5C), both calculated $\tau$ values exhibit significant negative magnitudes at the highest saturations. Note, however, that both values actually remain negative (although close to zero) over much of the saturation range. Close examination of the $P_c^d$-2 plots in Fig. 3.5B shows that the gas pressure microsensor may actually have experienced a small offset after the first two (the slowest two) secondary drainage curves, in that all curves after the first

two are approximately 2 cm water lower than the first two. This is an occasional issue with both types of sensors. (Also note the lower starting pressures in the five faster runs (Figs 3.5B and D).) When $\tau_2 *$ is recalculated using only the five faster drainages (Fig. 3.7, dotted red line), its shape and magnitude are *very* close to those of $\tau_1 *$.

The results in Fig. 3.7 suggest that the true magnitude of $\tau$ for the F-95 sand/water system studied here is likely on the order of ~$5\times10^3$ Pa·s at the most, and may actually be lower. Furthermore, the results in Fig. 3.7 highlight the potential for measurement artifacts to introduce order-of-magnitude errors in the calculation of $\tau$, even when extremely fast sensors are used.

### *3.3.2 F-95 sand/Sucrose solution*

Figure 3.8 shows measured dynamic capillary pressures for the F-95 sand/sucrose solution system (Expt. 2), calculated based on the definitions in Table 3.3. For comparison, apparent capillary pressures (the pressure difference between phases across the cell inlet and outlet) are also shown as an inset (Fig. 3.8E). For this experiment, a second wetting-phase sensor was used in place of a gas sensor. As such, the curves in Figs. 3.8A and C correspond to $P_c^d$-1A and $P_c^d$-1A*, respectively, and the curves in Figs. 3.8B and D correspond to $P_c^d$-1B and $P_c^d$-1B*, respectively. From the sensor response rate constants in Table 3.2, it can be seen that the sensor responses are considerably different from one another (A is faster than B), and are both considerably slower than the water sensor used in Expt. 1 ($k^w$ of 0.59, 0.40 vs. 3.2 $s^{-1}$ in Expt. 1). The slower rate compared with Expt. 1 can likely be attributed in part to the 3.5× higher viscosity of the sucrose solution (Table 3.1). Unlike Expt. 1 (Fig. 3.5), it can be seen that neither $P_c^d$-1A (Fig. 3.8A) or $P_c^d$-1B (Fig. 3.8B) completely converge at lower

saturations, but rather are shifted higher at higher rates. The differences between $P_c^d$-1A and $P_c^d$-1B are consistent with the differences in wetting-phase sensor response rate constants, with the slower sensor (Fig. 3.8B) creating the appearance of significantly higher dynamic capillary pressures for the same drainage process – a nearly 10 cm water difference at the fastest rate. It is important to emphasize that although these sensors are slower than the sensor used in Expt. 1, and differ considerably from one another, both are still very fast sensors. In fact, sensor A would exhibit a 50% response to a step input in only 1.2 seconds, while sensor B would exhibit a 50% response to a step input in only 1.7 seconds.

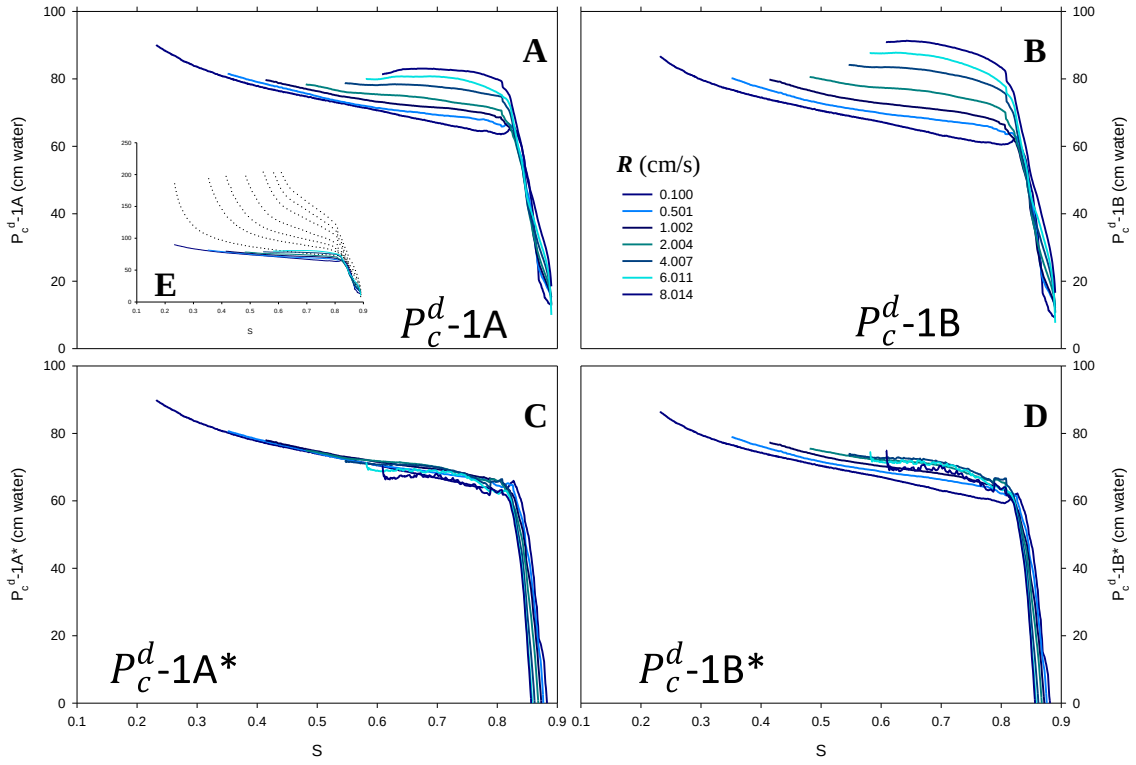


**Figure 3.8. (A and B) Uncorrected, (C and D) corrected, and (E) apparent dynamic capillary pressures, calculated based on the definitions in Table 3.3. Curves correspond to secondary drainages of F-95 sand initially saturated with sucrose solution (Expt. 2).**

Figs. 3.8C and D show the impact of correction for gas flow pressure drop and wetting phase sensor response for the two sensors. In the case of the faster sensor, where the required correction is smaller, the corrected curves to collapse onto one another (Fig. 3.8C). For the slower sensor, where the correction is larger, the curves do not completely collapse onto one another (Fig. 3.8D), but are considerably closer than the uncorrected curves (Fig. 3.8B). Note that the magnitude of the gas flow correction is slightly smaller to that for the F-95/water system (due to slower flow rates), but the slower sensor response in the F-95/sucrose means the sensor correction is much more significant. For the faster of the two sensors (A), the sensor pressure correction makes up approximately 90% of the total correction at S=0.7. This is in contrast to the 40% water sensor correction contribution in the F-95/water system.

Figure 3.9 shows calculated $\tau$ values corresponding to the four dynamic capillary pressures from Fig. 3.8. As might be expected, the $\tau$ values based on uncorrected dynamic capillary pressures ($\tau_{1A}$ and $\tau_{1B}$) are significantly greater than the $\tau$ values based on corrected dynamic capillary pressures ($\tau_{1A}$* and $\tau_{1B}$*). Furthermore, the uncorrected value corresponding to the slower of the two sensors ($\tau_{1B}$) is almost twice the magnitude of the uncorrected value corresponding to the faster of the two sensors ($\tau_{1A}$), and both values are considerably higher than the uncorrected values for the F-95/water system (Fig. 7). It is also interesting to note that neither uncorrected curve exhibits the decreasing $\tau$ with decreasing saturation that was observed in Fig. 3.7. The primary reason for this is the much greater contribution of slow sensor response (rather than gas flow) to creating the appearance of dynamic capillary effects in the

uncorrected F-95/sucrose solution system (Fig. 3.9) compared with the F-95/water system (Fig. 3.7).

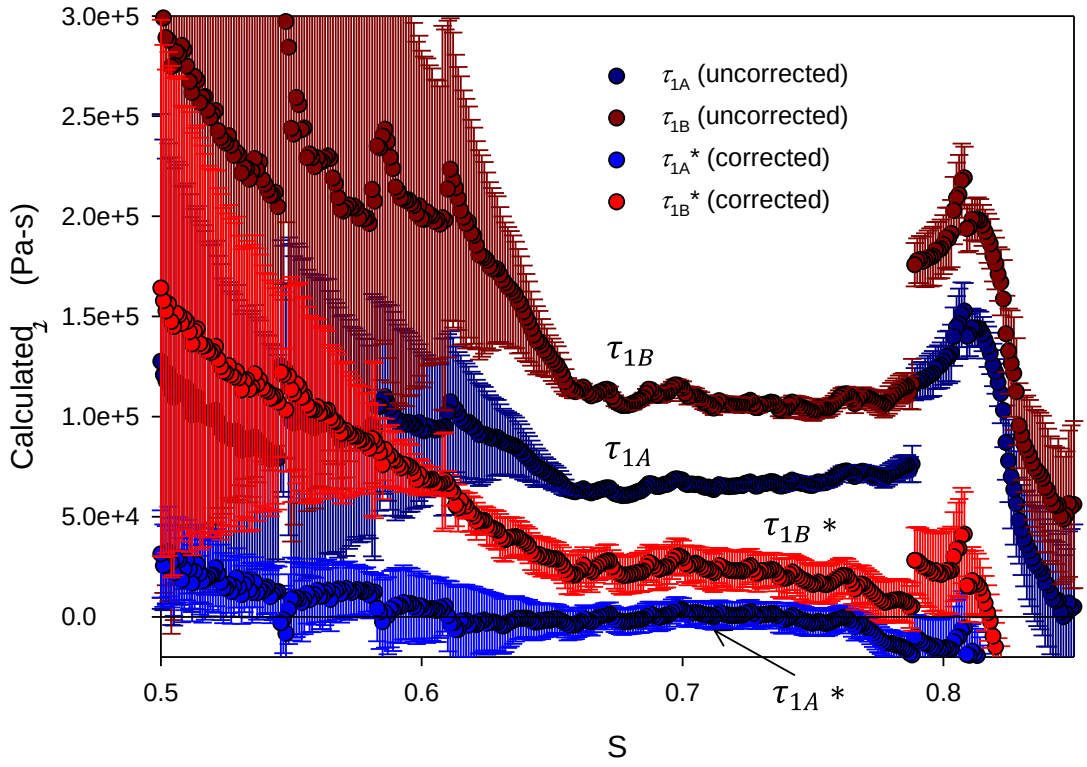


**Figure 3.9. Calculated uncorrected and corrected $\tau$ values for F-95 sand initially saturated with sucrose solution (Expt. 2). Values correspond to the definitions of $P_c^d$ in Table 3.3. Error bars correspond to standard error of the regression at each saturation.**

As might be expected from the corrected dynamic capillary pressures in Figs. 3.8C and D, the dynamic capillary coefficients calculated from the corrected pressures ($\tau_{1A}$* and $\tau_{1B}$*) are relatively small in magnitude. This is particularly true for $\tau_{1A}$*, which corresponds to the faster of the two sensors, and for which the corresponding corrected dynamic capillary pressures (Fig. 3.8C) come very close to collapsing to a single curve. The magnitude of $\tau_{1A}$* is between approximately 0 and ~$2\times10^3$ Pa·s over much of the saturation range shown, although the standard error of the regressions

overlaps 0 for nearly the entire range. The magnitude of $\tau_{1B}$* is higher, on the order of ~$2\times10^4$ Pa·s over much of the saturation range shown, but still small compared with the uncorrected value. It should also be noted that the 95% confidence intervals (not shown in Fig. 3.9 for clarity, but 2.57× the standard errors shown) for both corrected values ($\tau_{1A}$* and $\tau_{1B}$*) overlap one another, suggesting that the values not statistically different from one another.

### *3.3.3 SI-BG05 glass beads /Water*

Figure 3.10 shows measured dynamic capillary pressures for the SI-BG05 glass beads/water system (Expt. 3), calculated based on the definitions in Table 3.3. For comparison, apparent capillary pressures (the pressure difference between phases across the cell inlet and outlet) are also shown as an inset (Fig. 3.10E). As was the case for Expt. 2, a second wetting-phase sensor was used in place of a gas sensor for this experiment. As such, the curves in Figs. 3.10A and C correspond to $P_c^d$-1A and $P_c^d$-1A*, respectively, and the curves in Figs. 3.10B and D correspond to $P_c^d$-1B and $P_c^d$-1B*, respectively. As was the case in Expt. 2, the two water sensor responses are considerably different from one another (A is faster than B). The faster of the two sensors is slightly slower than the F-95/water system (Expt. 1), but faster than the faster sensor in the F-95/sucrose solution system (Expt. 2).

Like Expt. 2 (Fig. 3.8), it can be seen that neither $P_c^d$-1A (Fig. 3.10A) or $P_c^d$-1B (Fig. 3.10B) converge at lower saturations, but rather are shifted higher at higher rates. The differences between $P_c^d$-1A and $P_c^d$-1B are consistent with the differences in wetting-phase sensor response rate constants, with the slower sensor (Fig. 3.10B) creating the appearance of significantly higher dynamic capillary pressures for the same

drainage process – a nearly 15 cm water difference at the fastest rate. This error is approximately 50% greater than was observed for the slow sensor in the F-95/sucrose experiment (Expt. 2), primarily because the faster drainage rate in the glass beads/water system leads to more rapid water pressure changes, and consequently greater sensor lag, despite the faster sensor.

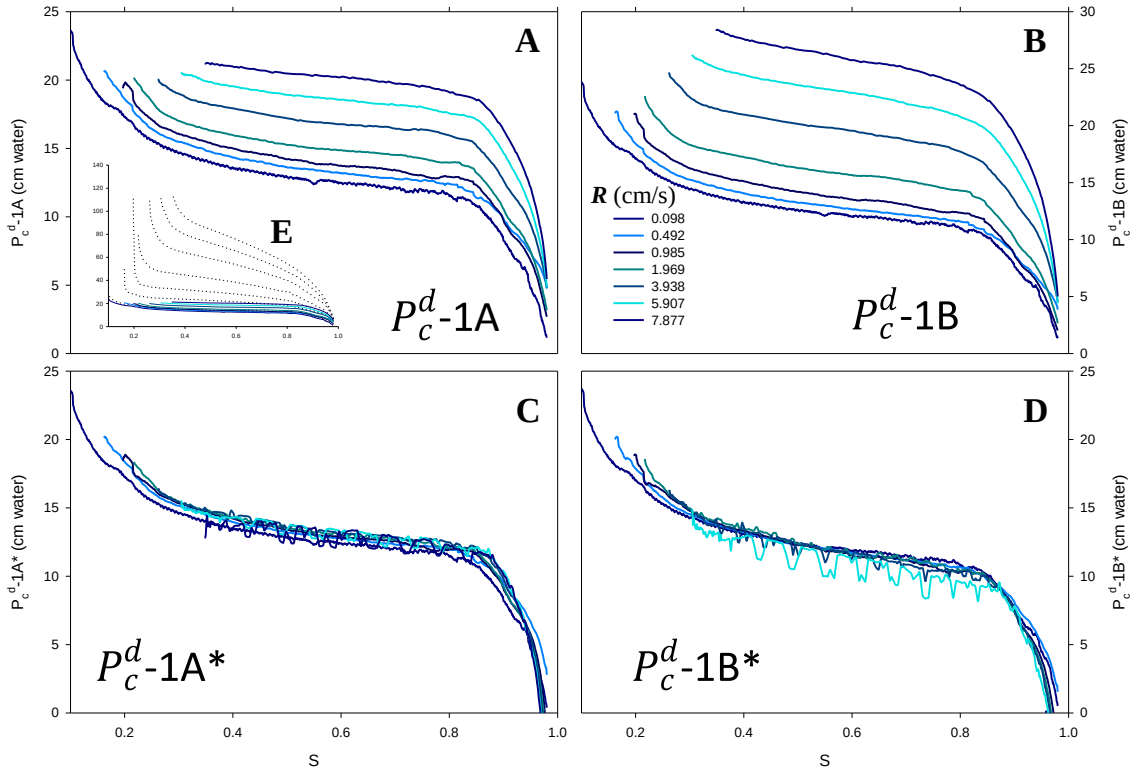


**Figure 3.10. (A and B) Uncorrected, (C and D) corrected, and (E) apparent dynamic capillary pressures, calculated based on the definitions in Table 3.3. Curves correspond to secondary drainages of SI-BG05 glass beads initially saturated with water (Expt. 3).**

Figures 3.10C and D show the impact of correction for gas flow pressure drop and wetting phase sensor response for the two sensors. In both cases, the corrected curves collapse onto one another. Note that the noise in the fast curves, most notable in the fastest curve of Fig. 3.10D, is simply amplification of signal noise in the sensor

pressure derivative (Eq. 3.3), apparent here because the correction is so significant (~15 cm water correction on a ~10 cm water $P_c$ – approximately 150% of the final value). Unlike the two experiments conducted in sand, the water sensor correction (Eq. 3.3) makes up nearly all of the correction (>99.7% at S=0.7). This is because the permeability of the glass beads is much greater, so the resistance to gas flow at the measured Darcy velocities is negligible.

Figure 3.11 shows calculated $\tau$ values corresponding to the four dynamic capillary pressures from Fig. 3.10. As might be expected, the $\tau$ values based on uncorrected dynamic capillary pressures ($\tau_{1A}$ and $\tau_{1B}$) are significantly greater than the $\tau$ values based on corrected dynamic capillary pressures ($\tau_{1A}$* and $\tau_{1B}$*). Furthermore, the uncorrected value corresponding to the slower of the two sensors ($\tau_{1B}$) is considerably greater than the magnitude of the uncorrected value corresponding to the faster of the two sensors ($\tau_{1A}$). Both uncorrected values are lower than the comparable $\tau$ value for the F-95/water system ($\tau_1$; Fig. 3.7). It is also apparent that, if viewed on the same scale, the uncorrected $\tau$ curves for the glass beads are considerably flatter than those for the sand – the result of the negligible gas flow correction. (Note that a slow sensor does impose a small decrease in $\tau$ with decreasing saturation at high saturations, but the effect is small compared with the gas flow correction.)

As might be expected from the corrected dynamic capillary pressures in Figs. 3.10C and D, the dynamic capillary coefficients calculated from the corrected pressures ($\tau_{1A}$* and $\tau_{1B}$*) are very small in magnitude. The magnitude of $\tau_{1A}$* is between approximately 0 and ~$1\times10^3$ Pa·s over much of the saturation range shown, while the magnitude of $\tau_{1B}$* is actually slightly negative.

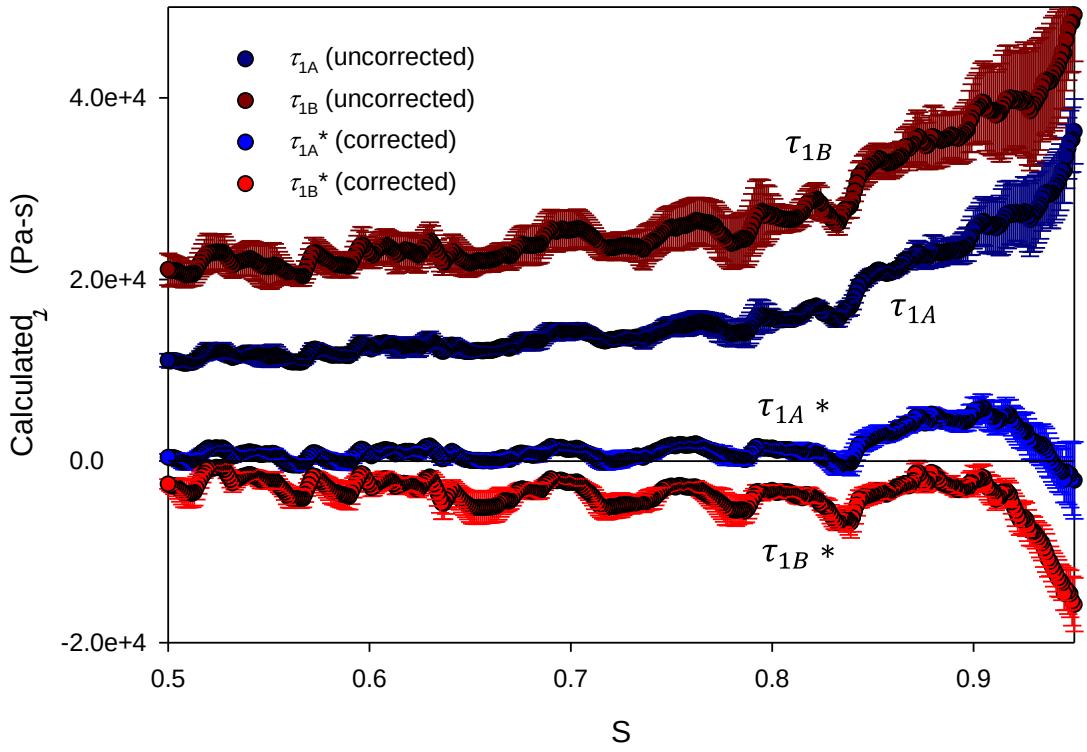


**Figure 3.11. Calculated uncorrected and corrected $\tau$ values for SI-BG05 glass beads initially saturated with water (Expt. 3). Values correspond to the definitions of $P_c^d$ in Table 3.3. Error bars correspond to standard error of the regression at each saturation.**

*3.3.4 Measurement artifacts in unsaturated systems*

The results of these experiments suggest that measurement artifacts may make a significant impact on the determination of the dynamic capillary coefficient $\tau$ from experimental data. Even extremely fast sensors have the potential to create the appearance of dynamic capillary effects if their rates are mismatched (or if a sensor is used in only one phase, creating the same effect as mismatched sensors). In cases where only a water phase sensor is used, an additional artifact which can impact calculations is pressure drops in the flowing gas. Our measurements with a stagnant water phase show very rapid response of gas sensors (e.g., Table 3.2, Expt. 1). However, when water is

draining, the accompanying flow of gas produces pressure drops that can be significant, depending on the permeability of the medium. For the work here, which used a very small soil cell, a simplified correction was used (Eq. 3.4) to correct for the pressure drop in the gas. The fact that calculations of $\tau$ made using that correction ($\tau_1$ $*$; Fig. 3.7) are in close agreement with the two-sensor measurements ($\tau_2$ $*$; Fig. 3.7), supports both the magnitude and underlying physics of the correction. In a larger column, where measurements are made on a moving front, pressure drops are likely to be most significant near the front. Preliminary unsaturated flow simulations conducted for this work show that, even for a porous medium with an order of magnitude higher permeability than F-95 sand (e.g., the sand used by Sakaki *et al.* (2010)), gas pressure drops of one to several cm water near the front are highly likely for typical Darcy velocities reported – an error that could create the appearance of a very large $\tau$.

It is interesting to note that the artifacts described here are themselves both scale dependent and system dependent, facts that may contribute to the significant variability in published $\tau$ values. In terms of system dependencies, the relationship between system backpressure and medium permeability can change the relative importance of sensor and flow artifacts. A system with a higher backpressure will artificially reduce the gas pressure drop in the medium compared with what would be observed for the same medium in a low-backpressure system, because the system itself (e.g., tubing, membranes) will dominate the water flow, creating a flatter $\tau$-S relationship.

In terms of scale dependence, it is very interesting to note that the relationship between water Darcy velocity at the outlet ($q$) (or, approximately equivalently, gas-phase Darcy velocity at the inlet) and the rate of saturation change $\frac{\partial S}{\partial t}$ can depend

significantly on column length for an unsaturated system. By mass balance, $q$ is related to the average saturation change over the entire column by Eq. 3.7:

$$q = nL\left.\frac{\partial S}{\partial t}\right|_{avg} \qquad \text{(Eq. 3.7)}$$

where $n$ is porosity, and $L$ is the length of the column. Although the local rate of saturation change can potentially be much larger than the average, in practice in air/water systems unless a column is very long (i.e., $L$>>air entry pressure) or the $P_c$-$S$ relationship is extremely flat, the maximum local rate of saturation change $\frac{\partial S}{\partial t}$ is likely to be reasonably well approximated by the maximum average rate of saturation change, $\left.\frac{\partial S}{\partial t}\right|_{avg}$. (This result has been verified with unsaturated flow modeling, and is because of the significant fluid viscosity differences in air/water systems; this result will *not* generally be true for liquid/liquid systems). For example, analysis of the outflow and $S$ versus time data published by Camps-Roach *et al.* (2010) for unsaturated drainage of a 20 cm long column packed with a coarse sand shows that the maximum local $\frac{\partial S}{\partial t}$ is only approx. 6% greater than the maximum $\left.\frac{\partial S}{\partial t}\right|_{avg}$ calculated from outflow data. (In contrast, the liquid/liquid data of Bottero *et al.* (2011b) show an order of magnitude difference between the local and average rates.) Taken together with Eq. 3.7, this result means that for a given $q$, a longer unsaturated column is likely to have a much lower maximum local $\frac{\partial S}{\partial t}$. Consider a comparison between the $q$ and $\frac{\partial S}{\partial t}$ of Camps-Roach *et al.* (2010) and the F-95/water data (Expt. 1) presented here. The $R$ = 0.95 cm s$^{-1}$ $\frac{\partial S}{\partial t}$ curve in Fig. 3.3 (Expt. 1, F-95/water) exhibits a maximum $\frac{\partial S}{\partial t}$ of approximately 0.008 s$^{-1}$, corresponding to a $q$ of ~3.5×10$^{-5}$ m s$^{-1}$. In contrast, the Camps-Roach *et al.* (2010) data (F32/50, 132

cm water gas pressure) exhibit a very similar $q$ (~$3.9\times10^{-5}$ m $s^{-1}$), but a maximum $\frac{\partial S}{\partial t}$ of approximately 0.00065 $s^{-1}$ – lower than our system by a factor that is very close to the ratio of column lengths (20 cm/1.27 cm = 15.7). The reasons this is important are that sensor artifacts are controlled by rates of pressure change, which closely track rates of saturation change, while gas flow artifacts are controlled by Darcy velocity. As such, changing the length of a column for the same material changes the potential contribution of different potential artifacts. Furthermore, the lower $\frac{\partial S}{\partial t}$ in a longer column for a given Darcy velocity means that any artifacts that impact $P_c^d$ will be amplified when $\tau$ is calculated, causing longer columns to give the appearance of higher $\tau$. For example, a 1 cm water error in $P_c^d$ in the $R$ = 0.95 cm/sec curve for our data (Expt. 1) would correspond to a $\tau$ error of approx. $1.2\times10^4$ Pa·s, while the same 1 cm error in a 20 cm long column with the same Darcy velocity would correspond to a $\tau$ error of approx. $1.5\times10^5$ Pa·s. (Numbers calculated in this way might realistically be considered to be an indication of the order of magnitude of the uncertainty in any measured $\tau$ value for a column of a given length and rate of saturation change.)

### *3.3.5 Magnitude of $\boldsymbol{\tau}$*

Considering the magnitudes of $\tau$ values in Figs. 3.7, 3.9 and 3.11 of this chapter, it is clear that the *uncorrected* values vary significantly between the different systems, with values as high as approximatly $10^5$ Pa·s. However, the uncorrected values also differ considerably between sensors where multiple sensors are used – a result that itself suggests the presence of measurement artifacts.

When the $\tau$ values in Figs. 3.7, 3.9 and 3.11are corrected to account for sensor response and pressure drop in flowing gas, the result is considerably different. If we

focus on the corrected $\tau$ values (i.e., $\tau$*) corresponding to the fastest sensors for each set of experimental conditions (i.e., the cases where the magnitude of correction for sensor response is the least), the measured $\tau$* values are very small, on the order of $10^3$ Pa·s or less. Even considering the $\tau$* values from the slower sensors, it would be difficult to say conclusively from these data that $\tau$* is nonzero for any of the three systems studied. Furthermore, no trends are apparent between the three (very different) systems.

To put the magnitude of our measured $\tau$* values into context, note that they are 2 to 4 orders of magnitude lower than nearly all of the recently published experimental values determined in larger columns (typically $10^5$-$10^7$ Pa·s). While some of this difference may result from uncorrected artifacts in some of the published data, it is also probable that there are some additional scale-related issues contributing to the different results. Note that although our soil cell is smaller than the columns used in most published dynamic experiments, it is absolutely large enough to contain a representative elementary volume (REV). The length of the cell, its shortest dimension, is more than 1000× the mean diameter of the F-95 sand grains, and more than 250× the mean diameter of the SI-BG05 glass beads, factors that are orders of magnitude larger than the thresholds suggested by the microtomography work of Costanza-Robinson *et al.* (2011) for an REV. If there is a fundamental relationship between $P_c^d$ and $\frac{\partial S}{\partial t}$, it should be measurable at this scale.

Both Camps-Roach *et al.* (2010) (gas/liquid) and Bottero *et al.* (2011b) (liquid/liquid) considered the effects of upscaling point measurements on the magnitude of $\tau$, with Camps-Roach *et al.* (2010) observing negligible scale effects, and Bottero *et al.* (2011b) observing an order of magnitude increase in $\tau$ with increasing scale. The

difference between these results is very likely the result of the difference in the relationship between $\frac{\partial S}{\partial t}$ and $\frac{\partial S}{\partial t}\Big|_{avg}$ for unsaturated versus liquid/liquid systems, as described in Sec. 3.3.4 above. While the data of Camps-Roach *et al.* (2010) show almost no difference between the local and average values, the data of Bottero *et al.* (2011b) show a local $\frac{\partial S}{\partial t}$ that is an order of magnitude greater than $\frac{\partial S}{\partial t}\Big|_{avg}$. Consequently, the scale effect that Bottero *et al.* (2011b) observe is mathematically the result of averaging over much more nonuniform saturation field than exists in the gas/liquid experiments of Camps-Roach *et al.* (2010).

Still, interestingly, even the point $\tau$ measurements of both Camps-Roach *et al.* (2010) and Bottero *et al.* (2011b) are two orders of magnitude greater than the measurements reported in this work, despite the similar sensor size (Bottero *et al.* (2011b) report the scale of their point measurements as 0.7 cm). One possible reason for this is that there may be a spatial mismatch in sensor response that is truncated in a smaller soil cell used here. (That is, the different fluid-selective pressure sensors may actually detect pressure in different spatial regions above or below the moving front, simply because of the need for flow to sensors to create sensor response.) Alternately, it may be that the dynamic capillary effect that creates an observed relationship between $P_c^d$ and $\frac{\partial S}{\partial t}$ is not a continuum phenomenon at all, but rather is caused by microheterogeneities in packing that have an impact on flow and pressure gradients that are only apparent at a larger scale (e.g., (Oliviera *et al.* 1996)). Additional work exploring these factors is needed to fully understand and predict dynamic capillary effects in porous media.

## 3.4 Conclusions

Results of this work show that experimental artifacts can have a profound impact on measurement of the dynamic capillary coefficient $\tau$, causing measured values to appear orders of magnitude greater than true values. Artifacts can also superimpose trends with saturation and system properties. The nature and magnitude of errors introduced by experimental artifacts are both system and scale dependent. When corrected for sensor response and gas pressure gradients, $\tau$ values measured in this work were found to be very small in magnitude, and largely independent of system properties. In contrast, uncorrected values were orders of magnitude larger, differed considerably between systems, and exhibited trends with saturation. Because of the small size of the experimental system used, the results of this work suggest that the dependence of measured capillary pressure on rate of saturation change may be less significant than previously thought at the REV scale.

# Chapter 4. Understanding the Magnitude of Gas Pressure Gradients in Unsaturated Media Experiencing Dynamic Drainage

## 4.1 Introduction

The capillary pressure-saturation ($P_c$-$S_w$) relationship is a constitutive equation that is necessary to understand and predict multiphase flow in porous media. A precise characterization of the $P_c$-$S_w$ relationship in various multiphase flow systems is essential for addressing a wide range of practical problems, such as design of remediation strategies for groundwater contamination caused by organic substances.

$P_c$-$S_w$ relationships have been measured for almost a century. Because equilibrium measurements can be time-consuming, methods of measuring the $P_c$-$S_w$ relationship under dynamic conditions were explored. However, many researchers observed that $P_c$-$S_w$ relationships measured dynamically often differed from equilibrium measurements, especially in the high saturation region (e.g., (Topp *et al.* 1967; Smiles *et al.* 1971; Vachaud *et al.* 1972; Stauffer 1978)). This phenomenon has been referred to as a dynamic capillary effect (Hassanizadeh *et al.* 2002).

There are many controversies surrounding dynamic capillary effects in terms of their magnitude, the physical factors that they depend on, or even whether or not they actually exist. Many studies have investigated dynamic effects (e.g., (Topp *et al.* 1967; Stauffer 1978; Wildenschild *et al.* 2001; Oung *et al.* 2005; Wildenschild *et al.* 2005; Camps-Roach *et al.* 2010; Sakaki *et al.* 2010; Bottero *et al.* 2011b; Goel and O'Carroll 2011; Civan 2012; Hou *et al.* 2012; Hou *et al.* 2014)). However, the results in terms of both the magnitude and system dependencies have been extremely inconsistent in

different studies. To better understand the impact of dynamic effects on multiphase flow, it is critical to uncover the sources that result in the inconsistences.

One factor that may explain some of the variability in reported dynamic effect measurements is the accuracy of gas pressures in calculation of dynamic capillary pressure. Capillary pressures ($P_c$) are experimentally determined by subtracting the wetting phase pressure ($P_w$) from the non-wetting phase pressure ($P_{nw}$) (in this case, the gas pressure, $P_g$). In many early studies, gas pressure was taken to be the applied pressure (either atmospheric, in a vacuum system, or some applied pressure in a pressure system) (e.g., (Topp *et al.* 1967; Smiles *et al.* 1971; Vachaud *et al.* 1972; Stauffer 1978)). The assumption was that air viscosity was low enough that gas pressure drops in the column would be negligible. Some experiments also included column vents in an effort to eliminate any gas pressure gradients; however, data exploring their performance were not reported. While some studies, both recent, e.g., (Camps-Roach *et al.* 2010), and older (Watson and Whisler 1968; Vachaud *et al.* 1973), included separate sensors to measure gas pressure, a large fraction of the early studies of dynamic capillary effects did not, and the assumption of infinite gas mobility is still widely accepted (e.g., (Wildenschild *et al.* 2001; O'Carroll *et al.* 2005; Sakaki *et al.* 2010)).

The pressure drops in a horizontal column are dictated by the boundary conditions and the permeabilities of porous medium and system, as illustrated in Figure 4.1.

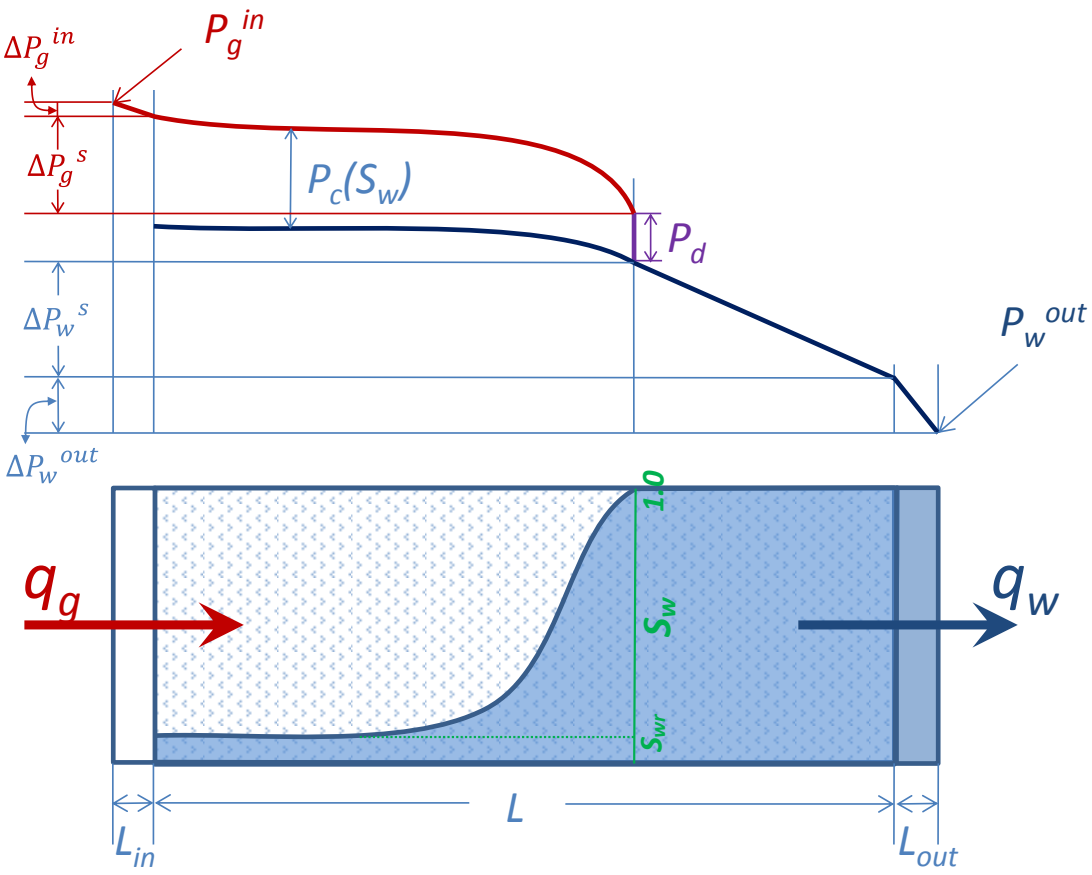


**Figure 4.1. A diagram of pressure drops**

Figure 4.1 shows the pressure drops through a horizontal column where gas pressure is fixed at one end and water pressure is fixed at the other, and where the wetting front is present at some point within the column. The total pressure drop from inlet to outlet is the sum of pressure drops within the system, i.e.:

$$P_g^{in} - P_w^{out} = \Delta P_g^{in} + \Delta P_g^{s} + P_d + \Delta P_w^{s} + \Delta P_w^{out} \qquad \text{(Eq. 4.1)}$$

where $P_g^{in}$ and $P_w^{out}$ are the applied gas and water boundary pressures, respectively, $\Delta P_g^{in}$ is the gas pressure drop in the inlet, $\Delta P_g^{s}$ is the gas pressure drop in the soil up to the wetting front, $P_d$ is the air entry pressure at the wetting front, $\Delta P_w^{s}$ is the water pressure drop in the saturated portion of the column, and $\Delta P_w^{out}$ is the water pressure

drop in the outlet of the column (a sum of any pressure drops in the saturated outlet and tubing).

The important point of Eq. 4.1 is that pressure drops within the gas ($\Delta P_g^{in}$, $\Delta P_g^{s}$) *must* exist for flow to occur. Furthermore, although not explored in this chapter, Eq. 4.1 suggests that it should be possible to estimate the total magnitude of expected gas pressure drops in a system by difference, since the applied pressures and $P_d$ are known, and the water pressure drops can be directly calculated from Darcy's Law, given outlet flow rates and permeabilities. (Note that the water pressure drops in Eq. 4.1 correspond to saturated flow.) An important implication of Eq. 4.1 is that any dynamic experiments measuring capillary pressures that assume gas pressure drops to be zero will necessarily overpredict $P_d$. The remainder of this chapter explores the factors that likely impact the magnitude of the overprediction.

The objective of the work described in this chapter was to explore the effect of gas pressure gradients and gas pressure drops during dynamic drainage in unsaturated porous media. The intent was to better understand conditions where internal gas pressure gradients and pressure drops might impact the value of $P_c$ calculated during dynamic measurements. Unsaturated drainage experiments were conducted to study the intensity of gas pressure drops under different conditions, and their impact on the dynamic capillary pressure obtained. Simulations were subsequently performed to better understand experimental data, and to further illustrate the effects of different flow conditions on gas pressure gradients and drops.

## 4.2 Experiments

### *4.2.1 Materials*

US Silica F-95 Ottawa fine sand (Berkeley Spring, WV) was used in this work. The permeability of the F-95 sand was determined using the falling head method, and slightly refined in the simulations to best fit measured data and account for experiment-to-experiment variations in packing. Note that measured permeability of F-95 sand determined in this work was higher than previous measured values determined in our laboratories, likely as a result of difficulty separating system backpressures in earlier small column measurements. (Measurements for this work were done in larger columns with very low backpressure, as described below.) Measured air entry ($P_d$) values also varied slightly between different runs due to packing differences.

Prior to use, the sand was rinsed with deionized water several times to remove fines, and then oven-dried. All experiments were conducted in unsaturated air-water systems. Degassed deionized water was used as the wetting phase, while compressed air was used as the non-wetting phase. The properties of F-95 sand and fluids used in this work are summarized in Table 4.1.

**Table 4.1. Properties of the porous medium and fluids used in the work.**

| Medium | $d_{50}$ (mm) | *Permeability* $\kappa$ ($m^2$) | *Porosity* $\phi$ | $Pd^a$ (m) | $\lambda^a$ |
|---|---|---|---|---|---|
| F-95 Sand | 0.140 | $1.03\sim1.10\times10^{-11}$ | 0.395 | 0.66~0.70 | 8.5 |
| Fluid[b] | | *Density* $\rho$ ($kg/m^3$) | *Viscosity* $\mu$ (cP) | *Surface tension* $\sigma$ *(mN/m)* | |
| Water (w) | | 998 | 1.002 | -- | |
| Air (nw, g) | | 1.2 | 0.018 | 72.9 | |

[a]Brooks-Corey parameters for unsaturated drainage system
[b]Fluid properties correspond to 20 °C, at atmospheric pressure

### *4.2.2 System Description*

Experiments were conducted using an automated system modified from systems previously described by Chen and Kibbey (2006), Chen *et al*. (2007) and Hou *et al*. (2012). Figure 4.2 shows a diagram of the measurement system used in this work. The system uses a custom-designed membrane-based cylindrical Plexiglas column for rapid measurement of $P_c$-$S_w$ relationship in unconsolidated media. For unsaturated drainages, a servo-pressure regulator (type 3110, Marsh Bellofram Corp., Newell, WV) is used to apply gas pressure to the top of the soil column. The servo-pressure regulator is controlled by a computer through a program specifically written for the measurement. Gas pressure can be applied in pre-programed ramp (e.g., for slow, pseudo-static drainage) or step (e.g., for rapid dynamic drainage) inputs. Experiments start with a known saturation, typically fully-saturated, with draining liquid collected in a vertical tube below the level of the column outlet. A pressure sensor is placed at the bottom of the vertical tube to calculate outflow volumes based on hydrostatic pressures recorded. Then real-time average saturations of the porous medium can be determined by

calculation from measured outflow volume. Gas inflow is introduced into the column using a nylon 11 tubing (6.5 mm OD by 4.5 mm ID). The same type of tubing is also used to lead outflow water into the vertical reservoir tube.

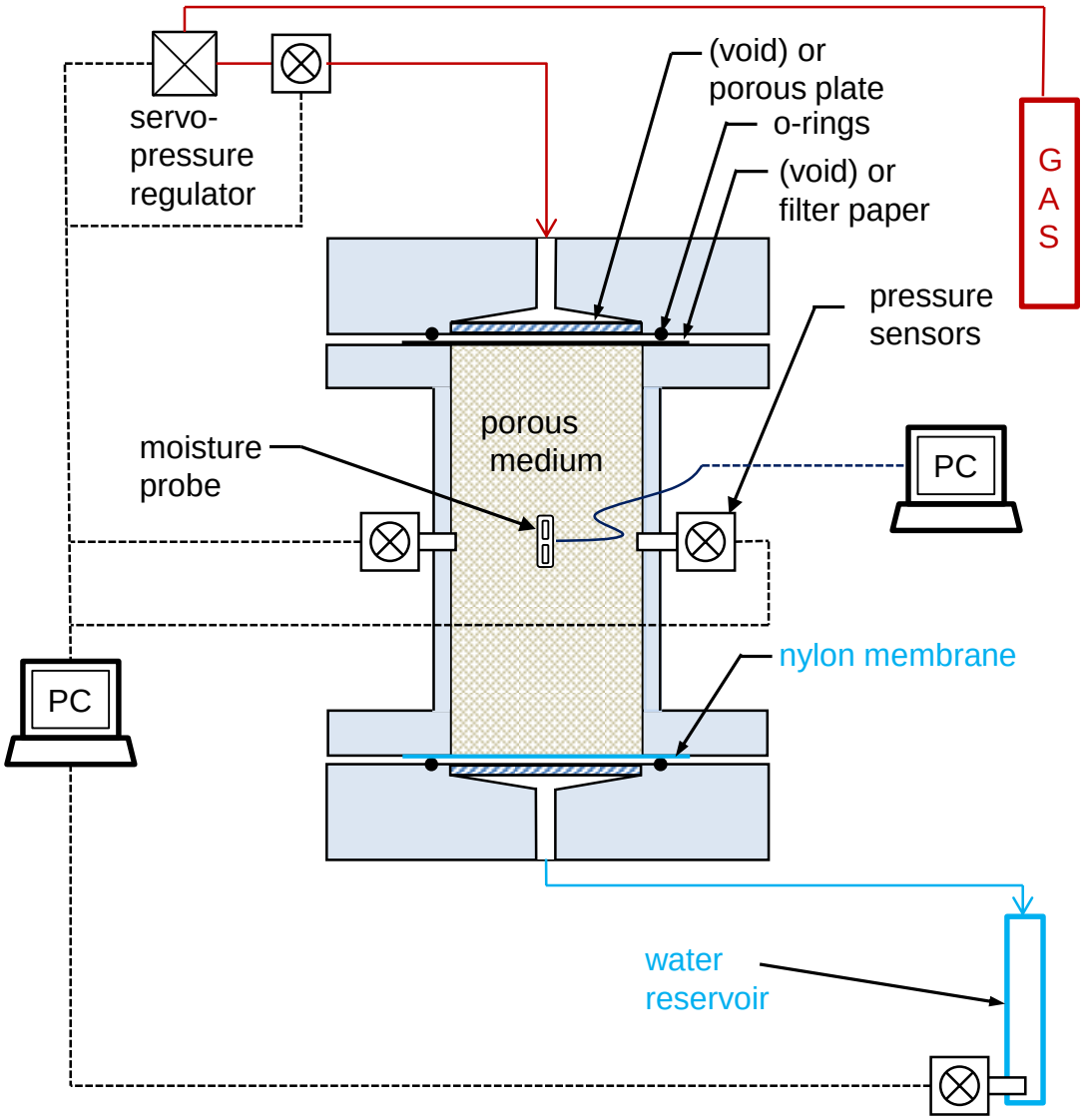


**Figure 4.2. A diagram of the experimental setup**

Unlike the small-volume soil cell previously used by Chen *et al*. (2007) and Hou *et al*. (2012), a larger column was used for this work to better understand spatial gas pressure gradients or pressure drops along a distance in unsaturated flow. The cylindrical columns used in this work were 15.24 cm long and 5.48 cm in diameter.

During drainage experiments, a nylon membrane (20 μm pore size; GE Osmonics, Inc., Minnetonka, MN) was used at the bottom of the column as a water-wet capillary barrier. No membrane or porous material was used on the top of the column to eliminate uncontrolled inlet pressure drops. (Specific experiments explored inlet pressure drops through addition of inlet restrictions, as described below.)

Two pore pressure sensors and a soil moisture probe were placed at the vertical midpoint of the column, 7.62 cm from the top of the column. The pressure sensors were installed on opposite sides of the column, while the moisture probe (Type EC-5, described below) was inserted on edge across the column at the same level as the pressure sensors, and at a 90 °angle to the line formed between the two sensors. The sensors were based on commercial pressure transducers (PX481A or PX181, Omega Engineering, Inc., Stamford, CT). Each transducer was integrated into the soil column through an aluminum housing specifically designed for this work. One end of the housing extended into the column approximately 4 mm, while the other end was threaded for the transducer. The sensor housings were machined to have minimum internal dead volume. The two pressure sensors were used to measure water pressure and gas pressure in the pores, respectively. The water sensor was a fluid-selective sensor, because it incorporated a hydrophilic nylon membrane (20 μm pore size) glued to the end of the end of the housing in contact with medium (See (Hou *et al.* 2012)). The gas sensor did not incorporate any membrane, so actually measured water pressure until gas reached the sensor allowing the contained water to drain; once the front passed, the sensor measured gas pressure. This arrangement for the gas sensor eliminates sensor rate effects which are always present in sensors with membranes (Hou

*et al.* 2012). For all experiments, the dead volume between the transducer diaphragm and the membrane in the water pressure sensor was filled with degased, deionized water. Although no membrane was used on the gas pressure sensor, Teflon beads (0.24 cm ID; Small Parts, Inc., Logansport, IN) were used to fill the dead volume of the sensor to reduce the volume of water initially in the sensor and aid with its drainage once the front reached the sensor. Sensor rate corrections for the water pressure sensors were applied using the methods described by Hou *et al*. (2012).

For this work, local saturations at the vertical midpoint of the column were estimated using an EC-5 soil moisture probe (Decagon Devices, Inc., Pullman, VA). The EC-5 probe makes use of the capacitance technique to measure the dielectric permittivity of surrounding media. Local saturations were estimated based on voltage readings and a two-point model developed by Sakaki *et al*. (2008). Careful analysis of EC-5 data, including comparisons with resistance measurements conducted in selected experiments found the EC-5 to be extremely insensitive at high saturations, often recording no saturation change until local $S_w$ dropped below ~0.8. Similar results have been reported by others ((Mittelbach *et al.* 2011; Mittelbach *et al.* 2012)). This fact made the EC-5 data unusable for exploring gas pressure effects, which typically occur at higher saturations, where gas relative permeability is low. As such, local saturation data obtained in this work were used only for determining $P_c$-$S_w$ parameters.

Applied pressures were controlled by adjusting voltage to the servo-pressure regulator at 0.1 s intervals. Data from all pressure sensors were collected and stored at 0.1 s intervals. Full descriptions of system design and data collection are given by Chen *et al*. (2007) and Hou *et al*.(2012).

### *4.2.3 Experimental procedures*

Dry packing procedures were employed for all columns used. A polyethylene (PE) porous plate (5.48 cm ID×0.16 cm H; Bel-Art products, Wayne, NJ) was placed in the recessed area of the bottom cap, and a nylon membrane with 20 μm pore size was placed across the plate. The main column was then carefully fastened to the bottom cap to avoid air gaps between the membrane and plate caused by deformation of the membrane. The sand was initially poured into the column to a height of 0.5 cm, and then a stirring rod with a flat head was used to mix sand grains to prevent stratified deposition. Care was taken to prevent damage to the bottom membrane. The column was then rapidly tapped against the bench 80~100 times to promote settling. Before pouring more sand, the surface of the medium was scratched unevenly using the stirring rod to prevent particle-size segregation caused by particle bounce. The sand was then sprinkled into the column in layers of 0.3 cm, with each layer carefully mixed using the stirring rod, firmly tapped, and scratched. Although this dry packing procedure does not result in a dense medium packing, it produces a uniform packing which minimizes preferential flow or layering artifacts.

After packing, a qualitative filter paper (#1, GE Whatman, Piscataway, NJ) was placed on the top of the sand, and the top cap, with another PE porous plate in it, was bolted to the cell. The whole column was flushed with $CO_2$ from the bottom for 15 min with a total volume flushed of at least 20 pore volumes. The column was then flushed upward with degased deionized water at rate of 1.2 ml/min for at least 10 h to displace $CO_2$. Prior to drainage experiments, the top porous plate and wet filter paper were removed, and the water outlet was set at the same level as the bottom of the medium. It

should be noted that some experiments made use of resaturated columns to improve the reproducibility between different experiments. When reusing, new clean filter paper and porous plate were placed on the top of the column; other procedures, such as $CO_2$ flushing and upward water displacement, were the same as described above.

The static $P_c$-$S_w$ relationship, needed for simulations, was obtained by applying a slow dynamic (pseudo-static) technique, with applied air pressure gradually increased up to 256 cm water at a pressure ramp of 0.0026 cm water/s. Four dynamic drainage experiments were conducted with a sudden air pressure increase of approximate 256 cm water. The four dynamic experiments included one experiment without any inflow and outflow restrictions added (Expt. 1), one without inflow and outflow restrictions but with a 1.0 mm ID vent (connected to the gas pressure source) located at the vertical midpoint (Expt. 2), one with only inflow restriction by introducing a 5 cm blue PEEK tube (0.2 mm ID) (Expt. 3), and one with only outflow restriction by introducing a 22.5 cm gray PEEK tube (1.0 mm ID) (Expt. 4). Note that for all four experiments, the combination of bottom nylon membrane and PE porous plate has hydraulic resistance slightly lower than the sand (up to one order of magnitude lower); to some extent the combination works as a weak outflow restriction. For the experiments with vent added, a 1.6 mm hole was drilled at the vertical central level, approximately 2 cm far away from the gas sensor along the cross-section circumference. The hole was connected to the air inlet through a 2 cm long gray PEEK tubing (1.6 mm OD ×1.0 mm ID) attached to a longer section of nylon 11 tubing (6.5 mm OD ×4.5 mm ID) and a series of adaptors (with minimum diameter up to 1.0 mm for a short distance) to connect the PEEK tubing

with the nylon 11 tubing. All experiments were conducted at room temperature of 22 ± 1 ℃.

### 4.3 Numerical Methods

A three-dimensional, three-phase, multi-component finite difference simulator, CompSim, was used in this work (Sleep and Sykes 1993a; 1993b). CompSim has been used in a range of subsurface multiphase flow and transport problems (Sleep and Sykes 1993b; Sehayek *et al.* 1999; O'Carroll and Sleep 2007). The model solves Equations 2.8, 2.10a and 2.10b, and incorporates a number of equations describing the $P_c$-$S_w$ relationship including Brooks-Corey (Eq. 2.13) and van Genuchten (Eq. 2.14) relationships, with extensions to include three-phase systems. Relative permeabilities are described by Eq. 2.15a, Eq. 2.15b and Eq. 2.16. The robust Newton-Raphson method is applied to linearize the highly nonlinear terms in the discretized multiphase flow and transport equations. A variety of implicit and explicit numerical discretization methods are coupled in the model, of which employed here is the fully implicit upstream weighted method. Spatial discretization of the parameters is achieved by one-point upstream weighting.

One-dimensional simulations were conducted to model the results of Expts. 1,3, and 4, and to explore the impact of system permeabilities in phase boundaries on gas pressure drops in dynamic unsaturated drainages. Each simulation included up to defined four porous medium types, as needed to simulate inlet restriction, sand, default system backpressure, and additional added outlet restriction. System permeability used in the simulations ranges 6.5-15 $\times 10^{-14}$ $m^2$ (all permeabilities reported here, except for the sand, correspond to a simulated length of 0.1 cm, 2 grid blocks high, as described

below). For resaturated columns, system permeability was observed to decrease slightly after each run due to fine particles accumulating on the bottom membrane. The permeabilities of inflow and outflow restriction layers are $1.06\times10^{-15}$ $m^2$ and $3.06\times10^{-14}$ $m^2$, respectively. In addition to modeling experimental results, the permeability of either inflow or outflow restriction layer was adjusted orders of magnitude to explore how system permeability in phase boundaries influence the gas drops or gradients.

Brooks-Corey parameters were determined based on the best fit to local $P_c$-$S_w$ curve measured in the pseudo-static experiments. Due to the insensitive response of the EC-5 probe at high saturations, the part of $P_c$-$S_w$ curve where local saturation is above 0.8 was excluded from the fitting. The parameters used in simulations are shown in Table 4.1.

The F-95 sand layer was discretized into 237 grids with spacing $\Delta h = 0.0635$ cm except the first and last grids, whose height was $1.5\times\Delta h$. This grid division ensured the center of the porous medium simulated was located right on a node. Each of the other three layer types was assigned a height of 0.1 cm, which was divided into two grids. The permeabilities used in the inlet or outlet restrictions are therefore normalized values corrected to account for to the layer height and cross-sectional area rather than the actual permeabilities measured or calculated. Constant head boundary conditions were applied for gas at the first grid block of the column, and for water in the last grid block of the column (i.e., $P_g(0) = P_g^{applied}$, $P_w(L) = 0$). No flow boundaries were applied for the opposite phases at each end of the column (i.e., $\frac{\partial h_w}{\partial z}(0) = 0$, $\frac{\partial h_g}{\partial z}(L) = 0$). All simulations were conducted using properties evaluated at room temperature

(293.15 K). Water was considered incompressible, while air was compressible with density following the ideal gas law.

## 4.4 Results and Discussion

### *4.4.1 System without inflow and outflow restrictions*

Figure 4.3 shows the observed and simulated local pressures of the non-wetting and wetting phases, $P_g$ and $P_w$ (a), and average saturation, $S_{avg}$, (b) over time for an F-95 sand unsaturated drainage experiment without any inlet or outlet restrictions except baseline system resistance (Expt. 1). The simulated average saturation and local saturation at the midpoint of the column, $S_{avg}$ and $S_{mid}$, and applied gas pressure are also included in Figure 4.3a for reference. From Figure 4.3, it can be seen that the simulation results of both phase pressures are in very good agreement with measured values. As mentioned, the Brooks-Corey model for the $P_c$-$S_w$ relationship was used in the CompSim simulator. Simulations based on the van Genuchten model were also conducted (results not shown). Although both van Genuchten and Brooks-Corey models present a good performance in fitting measurement data, the van Genuchten model showed a slightly better agreement with $S_{avg}$-$t$ data, particularly at early times, while the Brooks-Corey model showed a slightly better agreement with $P_g$-$t$ and $P_w$-$t$ data. As the main purpose of this work is to investigate the gas pressure drops and gradients, only results calculated based on the Brooks-Corey model discussed for the remainder of this chapter.

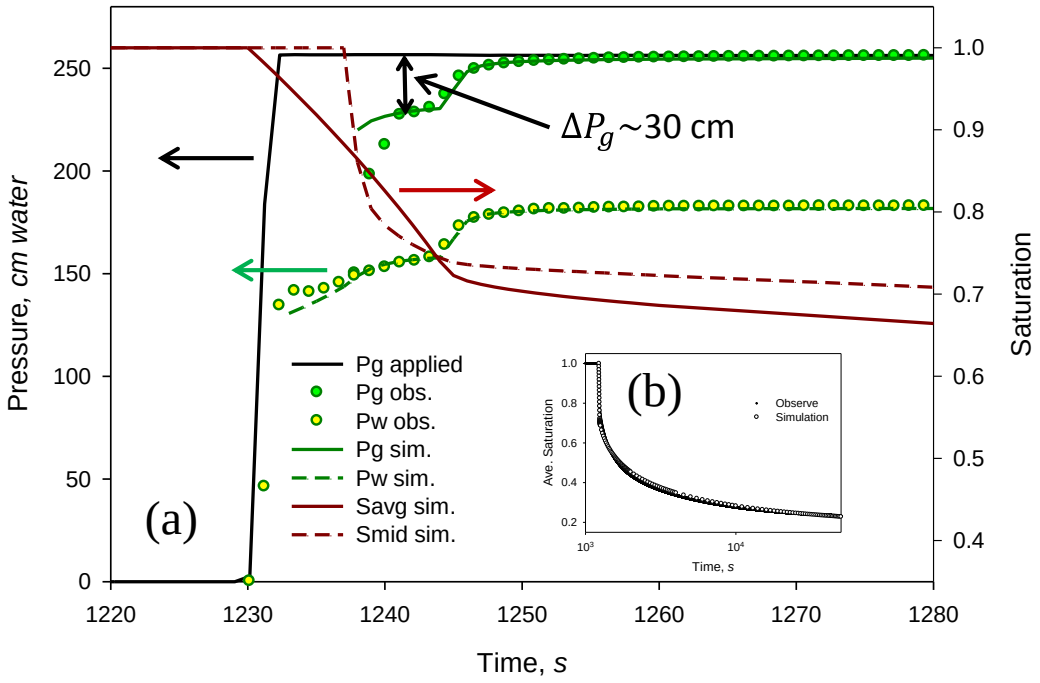


**Figure 4.3. Observed and simulated (a) local phase pressures and (b) average saturation at the midpoint of the column varied with time for Expt. 1.**

Results in Figure 4.3a show a significant gas pressure gradient existing at a certain time period and saturation range between the gas inlet and column midpoint where the gas pressure sensor lies. In a number of studies reported, gas is considered to mobile instantaneously through the porous media due to its low viscosity. However, in this study, a gas pressure gradient of approximately 30 cm water was observed at high saturations when applying a 256 cm water gas pressure to the top of the column, and the observed gas pressure gradient was found to be completely consistent with values simulated using conventional multiphase flow concepts. Using inlet gas pressures instead of gas phase pressures to calculate capillary pressure for this system would result in an overestimation of capillary pressure by tens of cm water at high saturations. Note that although this result was obtained from a pressurized flow system, a vacuum

system with the same pressure difference between column boundaries would have a virtually identical result in terms of the pressure drops and gradients.

The generation of the high gas pressure gradients in Fig. 4.3 is due to the very low gas relative permeability at high saturations, especially when saturations are greater than 0.8, as shown in Figure 4.4. According to generalized Darcy's law, although the dynamic viscosity of gas is very small compared with the liquids (0.018 Pa s), if $k_{rnw}$(S) is very small as well, the gas pressure gradient through porous medium could be substantial for a dynamic drainage scenario. The pressure drop mostly occurs near the front, where the porous medium is nearly fully saturated.

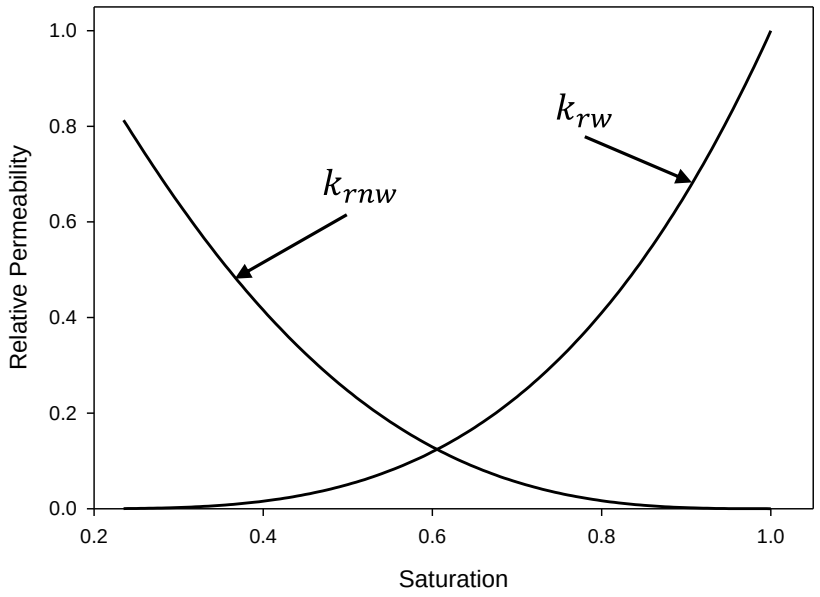


**Figure 4.4. The Brooks-Corey model of relative permeability of water and gas as functions of saturation for F-95 sand used in this work**

A break point is observed at $t$ = 1241 s in Fig. 4.3. This is because the fluid front reaches the bottom membrane. Due to the capillary barrier of the bottom hydrophilic membrane in this study, gas cannot pass through the membrane. When the

fluid front contacts the bottom membrane, Darcy velocity of the gas suddenly drops, causing a decreasing gas pressure gradient observed. Both $k_{rnw}$(S) and $q$ are the key points to influence the magnitude of gas pressure gradient through a sand column in dynamic unsaturated drainages.

### *4.4.2 System adding a vent but no inflow or outflow restrictions*

In some unsaturated drainage studies reported, vents have been used in an effort to prevent internal gas pressure gradients (e.g., (Rogers and Klute 1971; Smiles *et al.* 1971; Vachaud *et al.* 1972; Vachaud *et al.* 1973; Stauffer 1978)). While few papers provide details about the size of vents used, Vachaud *et al*. (1973) describe the use of vents based on 5 cm syringe needles with 0.07 cm ID, and Smiles *et al*. (1971) mention the addition of supplemental 0.1 cm OD vents, suggesting that that dimension could be consistent with vents used by others in the same laboratory and contemporaries at other laboratories. The question arises about whether the introduction of vents can help reduce gas pressure gradients between the gas inlet and the position of gas sensor. To investigate this, a vent with 0.1 cm inner diameter and 2 cm length was added at the same level as the gas sensor, as described at the methods section. The measurement data are shown in Figure 4.5, in comparison with results from Expt. 1, for which no vent was added. Results show that the observed $S_{avg}$-$t$ relationships for both experiments with vent and without vent are almost identical, indicating the average saturation is not affected by adding a vent. In addition, the $P_g$-$t$ relationships for both experiments show no significant difference, suggesting that simply adding a vent cannot guarantee an enhanced instantaneously gas mobile to the place where tensiometer lies. Caution should be used when interpreting experiments that rely on vents, because this result

indicates that differences between outside and pore gas pressures could still be considerable.

It should be noted that it is probable that a sufficiently large vent could presumably have an impact on internal gas pressures. After all, a vent is nothing more than another gas input point, so if flow possible through the vent is sufficiently high, internal gas pressures should respond to its presence. Still, however, the results of this experiment demonstrate that vents consistent with those used in the past by others are likely not large enough to allow equilibration of internal gas pressures during rapid drainage.

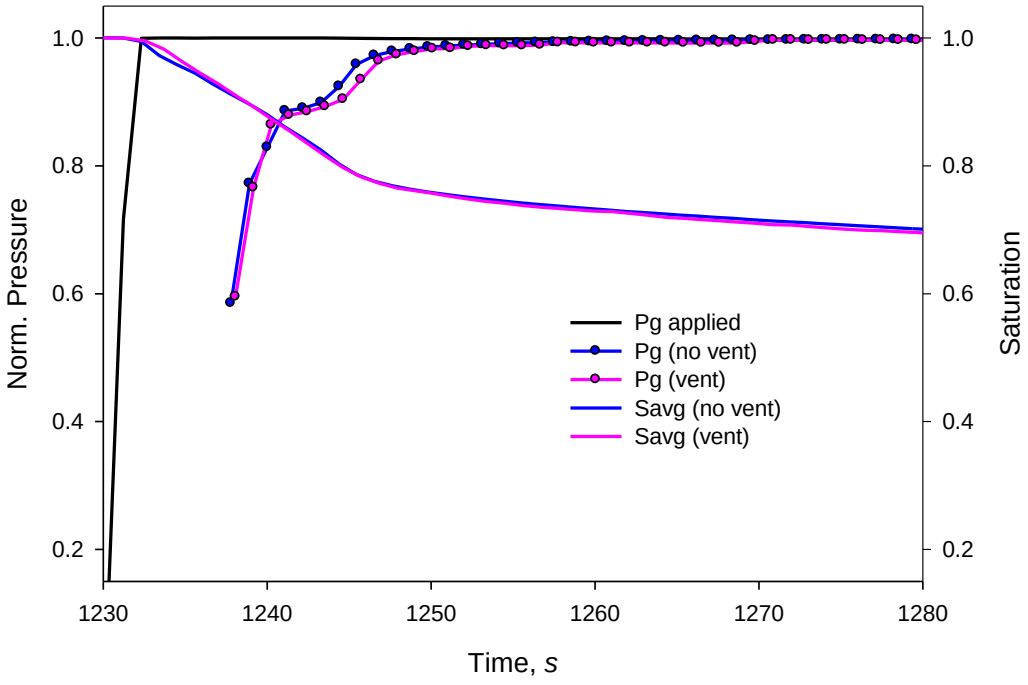


**Figure 4.5. Observed gas pressure at the midpoint of the column and average saturation varied with time for Expt. 2. Corresponding results for Expt. 1 are shown for comparison. Pressures are expressed as a normalized value (ratio of pressure at given time to maximum pressure) to facilitate comparison between different experiments.**

### *4.4.3 System with inflow restrictions*

In some systems for dynamic unsaturated drainage, inflow restrictions might be intentionally or unintentionally introduced, for example, by placing a water-wet porous plate or membrane before the sand, or by using too small of an access vent at the top of the column. An experiment was conducted (Expt. 3) to investigate the gas pressure drops and gradients affected by inflow restrictions by adding a short section of PEEK tubing (5 cm long $\times$ 0.13 cm ID) in the inlet gas line. The observed and simulated results of time evolution of saturation and phase pressures are shown in Figure 4.6. Again, the simulation results of both saturation and pressures fit the measurements well. The rate of saturation change for Expt. 3 is slower than that for Expt. 1 in the first 200 s after applying gas pressure, but the difference is relatively subtle. For example, in Expt. 1, it takes 50 sec for the system to reach an average saturation of 0.7, while Expt. 3 takes 70 sec to reach the same average saturation. If other conditions are same, the gas pressure difference between the applied pressure and the pressure measured at the midpoint shown in Expt. 3 would be expected to be smaller than that in Expt. 1 due to the lower drainage rate. However, astonishingly large gas pressure drops are observed at high saturations in Fig. 4.6 ($S>0.74$), with magnitudes on the order 100 cm water pressure difference between applied and internal pressures. If approx. 30 cm water of the observed gas pressure difference is due to the gas pressure gradient through sand (Expt. 1), then approx. 70 cm water (70% of the total pressure drop) gas pressure drop is caused by the less permeable medium covered on the top of the sand (in this case, a small diameter inlet). Of particular interest is the fact that, despite the significantly different gas pressure inlet, and the resulting 100 cm gas pressure drop, the flow rates

between Expt. 1 and 3 are only slightly different. That means that a significant inlet restriction might easily go undetected in an experimental system and yet create a significant deviation in apparent capillary pressure if capillary pressure were calculated based only on water pressures.

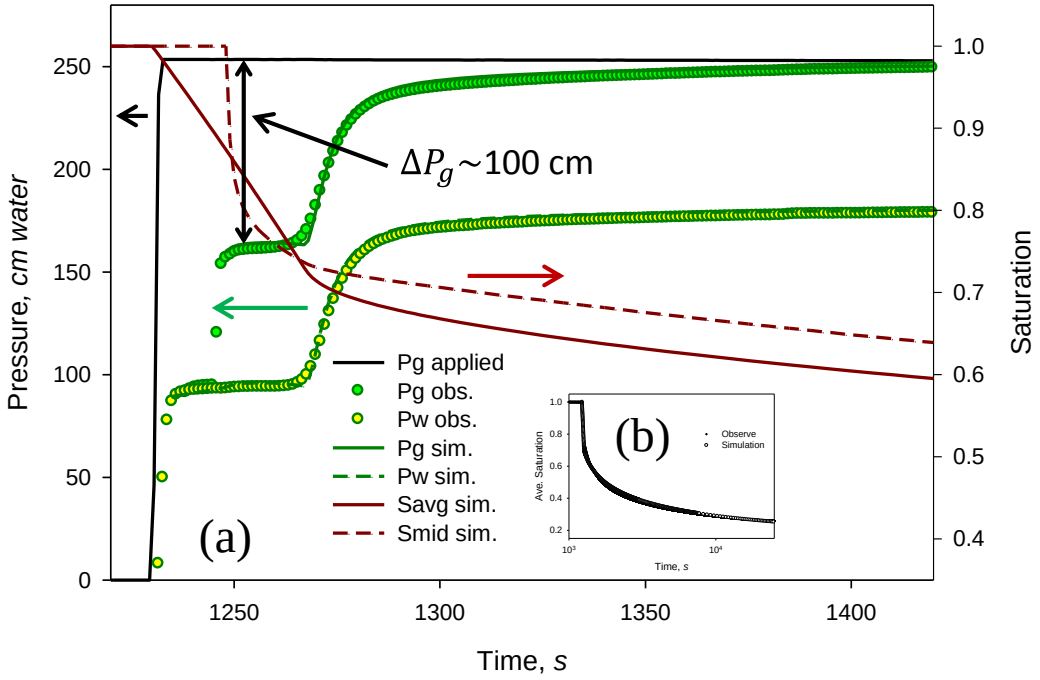


**Figure 4.6. Observed and simulated (a) local phase pressures and (b) average saturation at the midpoint of the column varied with time for Expt. 3.**

Another interesting observation can be made from Fig. 4.6. After presenting the initial gap in the first 35 s, local gas pressures slowly reach the applied pressure in the following 300 s. The same process in Expt. 1 takes less than 10 s. Comparing the pressure drops observed in Expts. 1 and 3, it can be concluded that the existence of inflow restrictions can enhance the gas pressure gradients and drops observed, in both magnitudes and durations. If inlet gas pressures are used to determine dynamic capillary

pressures under such circumstance, great error can be introduced in interpreting measured values.

### *4.4.4 System with outflow restrictions*

Some experimental configurations may include high system outlet resistance, either from the use of low permeability water-wet plates in the outlet, or from flow limitations in the outlet tubing or valves. This scenario is investigated by intentionally adding an outflow restriction using 22.5 cm long $\times$0.51cm ID PEEK tubing (Expt. 4) in this study. The observed and simulated results of time evolution of saturation and phase pressures are shown in Figure 4.7. The simulation results of both saturation and pressures fit the measurements well. After applying gas pressures, the rate of saturation change for Expt. 4 is considerably slower than that for Expt. 1 in the first 50 s until the front reaches the outflow boundary; then the rates of saturation change for the two experiments become identical. Due to the slow drainage rate of Expt. 4, the gas pressure gradients observed are much smaller: approximately 10 cm water at high saturations, in comparison with approximately 30 cm water for the system without any inlet or outlet restrictions, or approximately 100 cm water for the system with an inlet restriction.

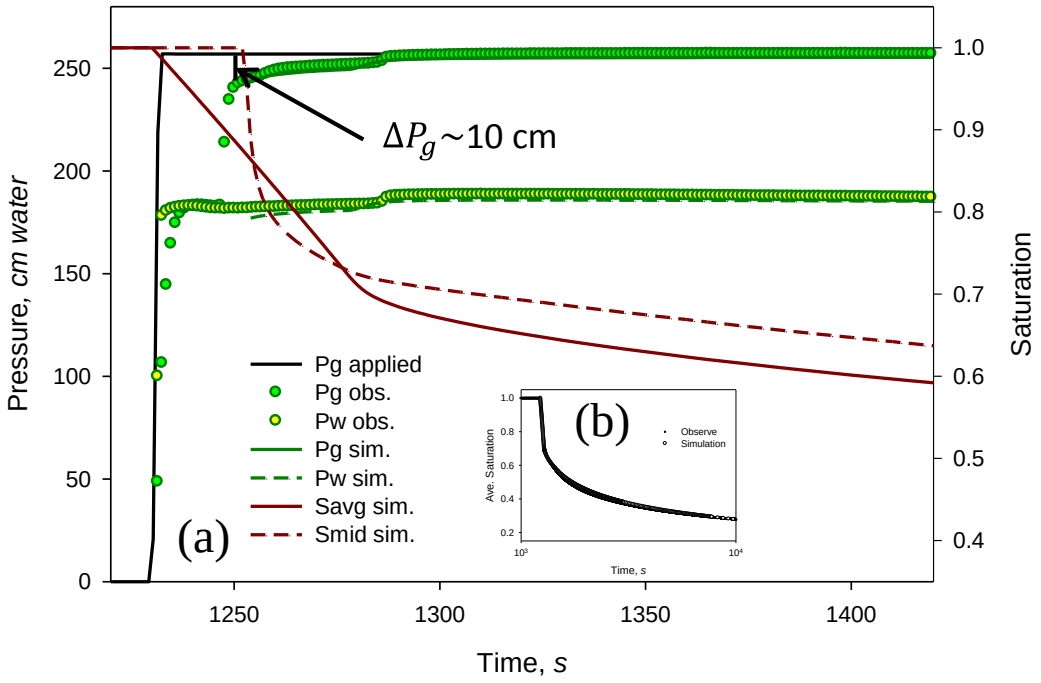


**Figure 4.7. Observed and simulated (a) local phase pressures and (b) average saturation at the midpoint of the column varied with time for Expt. 4.**

*4.4.5 Calculated apparent capillary pressures for non-vented systems*

As discussed previously, due to the significant gas pressure drops or gradients observed within porous media, using inlet gas pressures to calculate capillary pressures can potentially introduce great errors. Capillary pressures calculated based on inlet gas pressures are referred to as apparent capillary pressures herein. The simulated apparent $P_c$-$S_w$ relationships for different scenarios in non-vented system are shown in Figure 4.8. The static $P_c$-$S_w$ relationship is also shown for reference. From Figure 4.8, it is apparent that both inflow restriction and outflow restriction strongly affect the apparent $P_c$-$S_w$ relationship measured. Even though the porous material remains the same, a decreasing permeability of the inlet flow boundary enhances trends in gas pressure drops and gradients (by greater than 2 times in this case), while a decreasing permeability of the outflow boundary reduces such trends (by approximate 1/3 in this case).

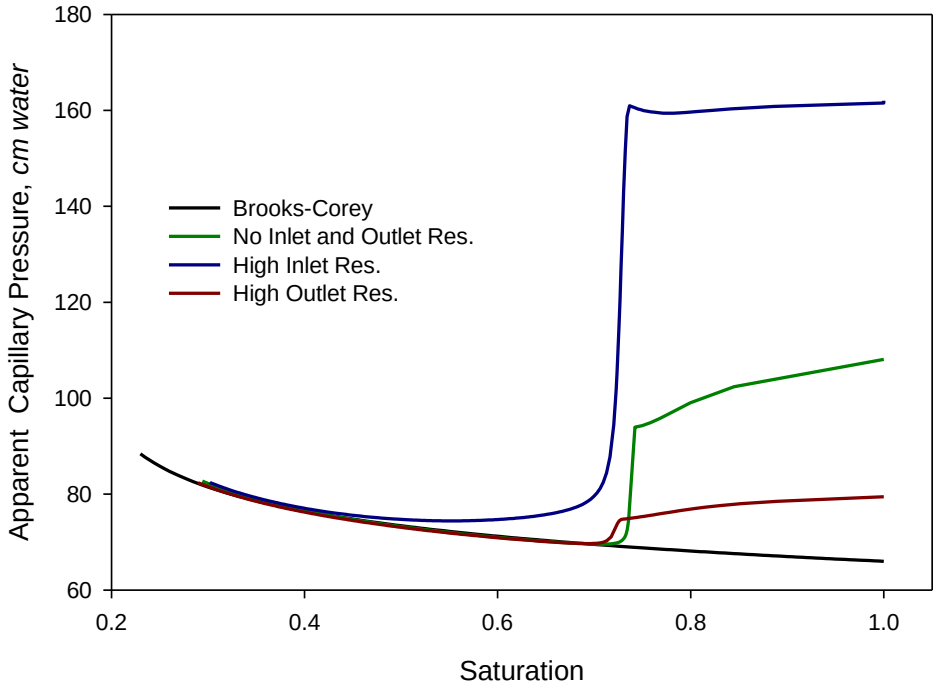


**Figure 4.8. Calculated apparent $P_c$-$S_w$ relationships for experiments with non-venting system. Brooks-Corey $P_c$-$S_w$ model of F-95 sand shown for reference.**

*4.4.6 Calculated apparent capillary pressures under various conditions*

Based on modeling parameters determined from simulating observed data, the effect of different boundary conditions on the determination of apparent $P_c$-$S_w$ relationship were investigated using CompSim. Figure 4.9 shows the simulation results of apparent $P_c$-$S_w$ relationships for different applied gas pressures.

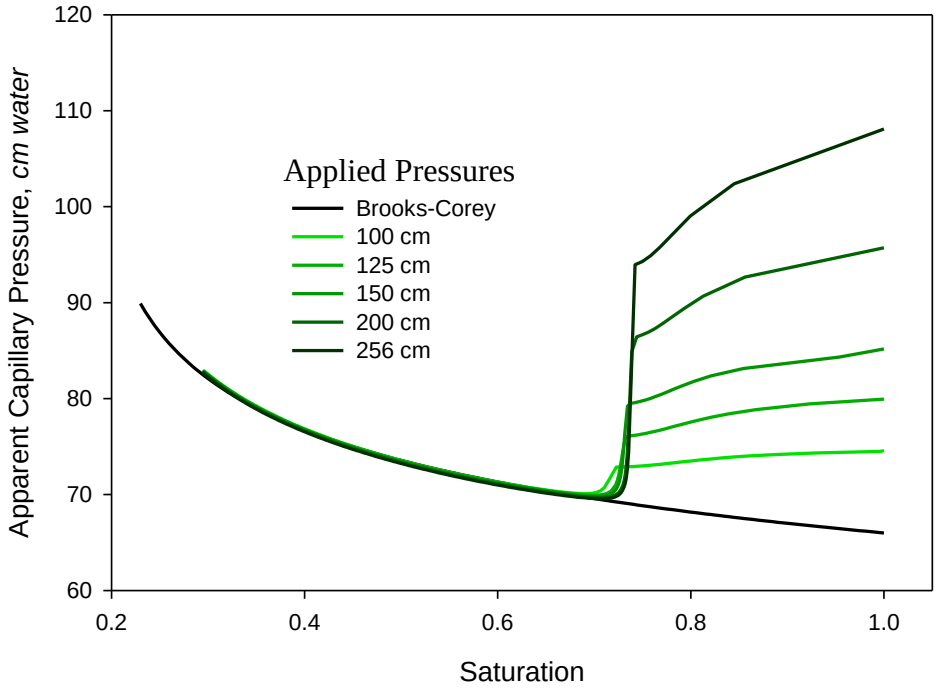


**Figure 4.9. Calculated apparent $P_c$-$S_w$ relationships under different applied gas pressures. Brooks-Corey $P_c$-$S_w$ model of F-95 sand shown for reference.**

It should be noted that although all phenomena of gas drops and gradients occur at high saturation range (i.e., $S_w$ >0.7) in this work, this finding is simply a result of the length of the column used (15.24 cm) that causes the front hits the bottom boundary at an early stage when the midpoint saturation is still high. Simulation work shows if the column length is extended by four times to 60 cm, gas gradients can be observed to influence apparent capillary pressures to saturations less than 0.6. However, since extending column length decrease the flow rate, all else being equal, the gas gradients observed correspondingly decrease due to the reduction in Darcy velocity.

Figure 4.10 shows simulation results of apparent $P_c$-$S_w$ relationships for different permeabilities of inflow restriction. The permeability of the inflow boundary used was varied in one-order-of-magnitude steps, ranging from $1.06\times10^{-13}$ to $1.06\times10^{-16}$ $m^2$. The

result of simulation without inflow restriction added is also shown in the figure. Before the front reaches the system boundary, it can be seen that increase of inflow boundary permeability significantly influences gas pressure drops and gradients, with greater restrictions causing greater pressure drops. As mentioned before, flow of water dominates the flow rate in media, so significant variation in inlet restrictions can produce little difference in flow rate while still producing significant differences in pressure drops.

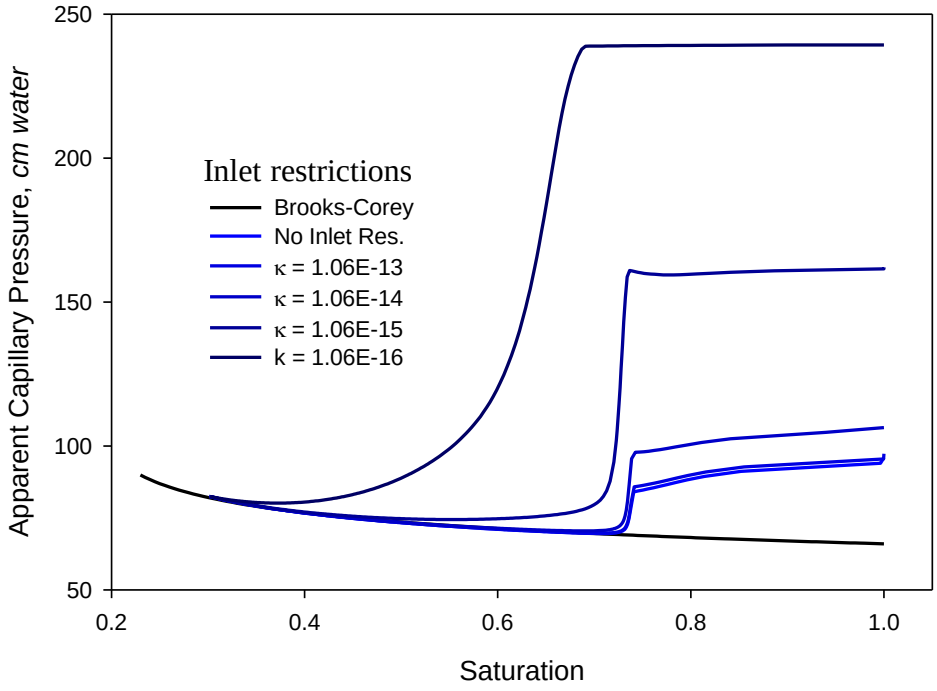


**Figure 4.10. Calculated apparent $P_c$-$S_w$ relationships under different inflow restrictions. Permeabilities varied in one-order-of-magnitude steps for each condition. Brooks-Corey $P_c$-$S_w$ model of F-95 sand and curve without inflow restrictions shown for reference.**

Figure 4.11 shows simulation results of apparent $P_c$-$S_w$ relationships for different permeabilities of outflow restriction. The permeability of outflow boundary used varied in one-order-of-magnitude steps, ranging from $3.06\times10^{-12}$ to $3.06\times10^{-15}$ $m^2$. The result of simulation without restriction added is also shown in the figure. Before the front reaches the boundary, it can be seen that increase of outflow boundary permeability influences gas pressure drops and gradients, with greater restrictions reducing gas pressure gradients by reducing flow rates.

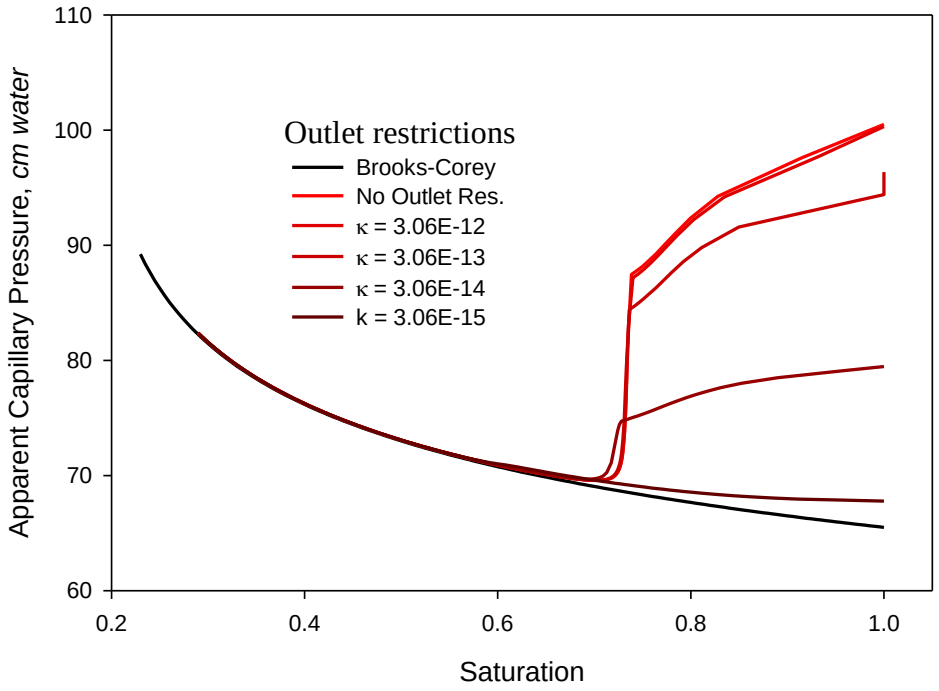


**Figure 4.11. Calculated apparent $P_c$-$S_w$ relationships under different outflow restrictions. Permeabilities varied in one-order-of-magnitude steps for each condition. Brooks-Corey $P_c$-$S_w$ model of F-95 sand and curve without inflow restrictions shown for reference.**

## 4.5 Conclusions

A combination of experimental measurements and simulations were conducted to investigate the effect of gas pressure gradients or drops under different flow

conditions during dynamic drainage. Results show that significant gas pressure gradients are observed and simulated in unsaturated flow system without any restrictions added. Simply adding a vent around pressure sensors does not necessarily eliminate internal gas pressure gradients. System permeabilities in column boundaries also strongly influence trends in gas pressure drops and gradients, with greater inflow restrictions enhancing the drops and gradients, and greater outflow restrictions reducing the gradients. The results have significant implications for determining apparent capillary pressures, suggesting that subtle difference in boundary properties can cause seemingly very different flow behaviors and measured capillary pressures for the same porous medium in different experimental setups. As a result, caution should be used interpreting measured values of apparent capillary pressure in systems where internal gas pressure is not measured directly.

# Chapter 5. The Influence of Saturation Averaging Caused by the Spatial Measuring Window of Saturation Probe on the Measurement of $\tau$[†]


## Abstract

Many studies over the past four decades have observed that capillary pressure-saturation ($P_c$-$S_w$) relationships are often different when measured dynamically under rapidly changing pressure inputs. This phenomenon has been referred to as a dynamic capillary effect, and its magnitude is often quantified by the dynamic capillary coefficient, $\tau$. Experimentally-reported values of $\tau$ have varied by orders of magnitude, even for seemingly similar experimental systems. The purpose of the present work is to numerically explore the likely impact of fluid properties on the calculation of $\tau$ from experimental measurements. Specifically, the emphasis is on understanding how spatial averaging of the saturation profiles resulting from different fluid combinations contributes to the apparent magnitude of $\tau$ derived from experimental measurements.

Simulations of dynamic drainage in a packed sand column were conducted using the CompSim multiphase flow simulator. Four nonwetting phase fluids with viscosities spanning four orders of magnitude were studied. Comparison between local and spatially-averaged rates of saturation change show significant differences, with the magnitude of the difference increasing with increasing viscosity to interfacial tension ratio and increasing drainage rate. Results show that at averaging scales likely to be experienced during experimental saturation measurements, this effect is likely to


[†] This chapter has been published as "The influence of unavoidable saturation averaging on the experimental measurement of dynamic capillary effects: A numerical simulation study" by L. Hou, B. E. Sleep and T. C. G. Kibbey in *Advances in Water Resources*, 2014.

produce significant differences in the ultimate magnitude of the calculated $\tau$ values for different fluid systems and drainage rates. This result means that conventional flow phenomena may produce an inherent systematic bias in experimental measurements of $\tau$, amplifying measured values for high viscosity or low interfacial tension systems and for experiments where higher drainage rates are used.

## 5.1 Introduction

Multiphase flow in porous media plays a central role in a number of industrial and environmental phenomena. Examples include enhanced oil recovery, remediation of non-aqueous phase liquids (NAPLs) in groundwater, and $CO_2$ geological sequestration. A quantitative understanding of the fundamental mechanisms underlying multiphase flow is essential to precisely describing and accurately modeling these phenomena.

The capillary pressure-saturation relationship ($P_c$-$S_w$ relationship) is a constitutive relationship that influences the movement and distribution of immiscible fluids in porous media. The $P_c$-$S_w$ relationships for a variety of soil types have been examined under steady-state conditions for over six decades. Many empirical equations have been developed to describe the equilibrium relationships between capillary pressure ($P_c$, the difference between the non-wetting and wetting phase pressures) and wetting phase saturation ($S_w$, the fractional volume of pores filled with wetting phase). For example, the Brooks-Corey (1966) and van Genuchten (1980) equations are among the most widely used equations. These empirical equations have been found to fit data from equilibrium $P_c$-$S_w$ experiments well.

Many studies have observed that $P_c$-$S_w$ relationships measured during dynamic drainage or imbibition (i.e., where capillary pressure is changed too rapidly to allow saturation to reach an equilibrium value) can differ from equilibrium $P_c$-$S_w$ relationships (Topp *et al.* 1967; Smiles *et al.* 1971; Vachaud *et al.* 1972; Stauffer 1978; Oung *et al.* 2005; Camps-Roach *et al.* 2010; Sakaki *et al.* 2010; Bottero *et al.* 2011b; Goel and O'Carroll 2011; Civan 2012; Hou *et al.* 2012; Mirzaei and Das 2013). The observed rate-dependence of capillary pressure in porous media experiencing dynamic saturation change is often referred to as a dynamic capillary effect. Many efforts have been made to quantitatively investigate dynamic effects in $P_c$-$S_w$ relationships, and a number of different parameters have been used to describe the observed effects. One of the most common parameters used to describe dynamic capillary effects in recent studies is the dynamic capillary coefficient, $\tau$. The dynamic capillary coefficient, $\tau$, is given by Eq. 5.1 (Hassanizadeh and Gray 1993a; Hassanizadeh and Gray 1993b; Hassanizadeh *et al.* 2002):

$$\tau = -\frac{P_c^d - P_c^s}{(\partial S_w/\partial t)} \qquad \text{(Eq. 5.1)}$$

where $P_c^d$ is dynamic capillary pressure (i.e., the observed pressure difference between non-wetting and wetting phases when saturation is changing), $P_c^s$ is static capillary pressure (pressure difference between phases under static conditions (no flow)), and $\partial S_w/\partial t$ is the rate of saturation change. It should be noted that some authors have suggested that the term "dynamic capillary pressure" is misleading because $P_c^d$ is an observed pressure difference between phases rather than a true capillary pressure (Bottero *et al.* 2011b). However, we adopt this widely-used terminology in the interest of concise discussion.

Although a large number of values of $\tau$ have been reported, remarkable uncertainty in its magnitude exists. In general, reported experimentally-measured $\tau$ values have spanned more than three orders of magnitude, even for seemingly similar systems (e.g. (Hassanizadeh *et al.* 2002; Oung *et al.* 2005; Camps-Roach *et al.* 2010; Sakaki *et al.* 2010; Bottero *et al.* 2011b; Goel and O'Carroll 2011)). Our previous experimental study in a small-volume unsaturated (air-water) sand system (Hou *et al.* 2012) suggested that experimental artifacts (i.e. finite sensor response and flow-induced gas pressure gradients) may account in part for the considerable uncertainty in $\tau$ values; further study is needed to uncover other contributors.

Variability in $\tau$ has been observed not only in its magnitude, but also in its dependence on system properties (e.g., porous medium grain size, fluid properties). Even reported results examining the effect of volume averaging on $\tau$ have been contradictory. For example, Camps-Roach et al. (2010) reported little dependence of $\tau$ values on averaging volume for an air-water system. In contrast, Bottero et al. (2011b) reported an order of magnitude difference in values of $\tau$ for different averaging volumes in a tetrachloroethylene (PCE)-water system with a similar sand. In our previous work (Hou *et al.* 2012), we used calculations to show that the difference between the scaling behavior of those two specific systems was primarily the result of the different fluids used (air-water vs. PCE-water), and their effect on the saturation profile. Using Eq. 5.1 to calculate $\tau$ requires measurement of the rate of change in $S_w$ (i.e., $\partial S_w/\partial t$). If $\partial S_w/\partial t$ obtained in a small domain (e.g. for a point) differs significantly from that obtained in a large domain, the difference in $\tau$ calculated can be remarkable.

The objective of this study is to explore scale dependence of dynamic capillary effects during drainage in air-water and organic-water multiphase flow systems. In particular, the emphasis is on understanding how the fluid properties in the system influence the saturation profile, and the resulting impact on the magnitude of measured $\tau$. While a number of experimental and modeling studies have examined the effect of volume averaging on observed dynamic capillary effects ((Bourgeat and Panfilov 1998; Das *et al.* 2004; Dahle *et al.* 2005; Gielen *et al.* 2005; Manthey *et al.* 2005; Camps-Roach *et al.* 2010; Bottero *et al.* 2011b; Goel and O'Carroll 2011; Joekar-Niasar and Hassanizadeh 2011)), few have directly explored the impact of fluid properties on the spatial distribution of fluids, and the resulting implications for experimental measurement of $\tau$. In this study, a series of primary drainage curves are simulated for air-water or organic liquid-water flow in a fine sand to investigate the difference in saturation-related properties (i.e., the $S_w$ and $\partial S_w/\partial t$ profiles) between different fluid systems. The purpose of the work is to investigate how a small difference between $P_c^d$ and $P_c^s$ – either resulting from an experimental or sensor artifact (e.g., (Hou *et al.* 2012)) or from a true dynamic capillary effect – would be amplified in the calculation of $\tau$ by fluid- and scale-specific impacts on $\partial S_w/\partial t$ (the denominator of Eq. 1). Because experimental sensors and other methods used to measure saturation have a finite spatial range (i.e., they detect an averaged saturation over some volume), a quantitative understanding of this relationship is of critical importance to understanding the effect of fluid properties on measured $\tau$ values.

It is important to emphasize that while this work examines the effect of saturation averaging on determination of $\tau$, it does not explore the results of averaging

in capillary pressure. While the effects of pressure averaging are of interest in numerical models where the impact of different grid resolutions must be understood, it is critical to recognize that, from an *experimental measurement* standpoint, an average pressure in a porous medium has no physical meaning. A transducer-based pressure sensor used to determine a phase pressure needed to calculate capillary pressure measures a single pressure value representing the force of fluid acting on a small internal semiconductor diaphragm within the pressure transducer. While that pressure may or may not be equivalent to the pore pressure in a given phase at a given time or location with a porous medium, depending on issues of fluid continuity and porous membrane conductivity (e.g., (Hou *et al.*)), it is not possible to design a pressure sensor based on a single pressure transducer that measures an 'averaged' pressure over any scale within a porous medium. (In contrast, all measurements of saturation are spatial averages with varying domain sizes, depending on the method used (e.g., time-domain reflectometer (TDR) or other sensor, gamma ray attenuation, outflow volume tracking) and the details of the specific application.) Because nearly all reported studies of dynamic capillary effects have used direct pressure measurements from transducer-based pressure sensors to indicate phase pressures (e.g., (Topp *et al.* 1967; Smiles *et al.* 1971; Stauffer 1978; Camps-Roach *et al.* 2010; Sakaki *et al.* 2010; Bottero *et al.* 2011b; Goel and O'Carroll 2011; Hou *et al.* 2012)), the approach used here is appropriate for interpreting the effects of fluid properties on the experimental measurement of dynamic capillary effects.

## 5.2 Numerical Simulations

### *5.2.1 Description of the simulator*

The CompSim simulator was used in this work. CompSim is a three-dimensional, three-phase, multi-component finite difference model developed for subsurface multiphase flow and transport problems (Sleep and Sykes 1993a; 1993b). A detailed description of CompSim is provided in Chapter 4 of this dissertation.

It is noted that this work uses conventional multiphase flow calculations to explore how unavoidable saturation averaging during experimental measurements could emulate dynamic effects, impacting the magnitude of measured $\tau$ values. As such, no dynamic capillary effects are explicitly included in the simulations, and no assumptions are made about the underlying causes of observed dynamic capillary effects.

### *5.2.2 Simulation parameters*

One-dimensional vertical simulations were conducted in a simulated sand column 15.24 cm (6 in) high, for the reason that a majority of reported dynamic $P_c$-$S_w$ measurements have been conducted in columns between 10 and 20 cm in length. The simulated column was subdivided to 1187 grid blocks, with each block 0.127 mm high except the grid at the two ends, which were 0.9525 mm. CompSim uses a block-centered finite difference scheme for all nodes, with the exception of the nodes on domain boundaries, which are located on the domain boundary. The grid division used for the work ensured that the center of the simulated column (7.62 cm from the bottom) would lie on a node, and the height of the simulated column would be exactly 15.24 cm (i.e., all block dimensions would be rational numbers). Selected simulations conducted

with a 5× higher grid spacing produced virtually identical results, indicating that the spacing was sufficiently small for the work.

The porous medium used in the simulations had the same properties as used by our previous experiment studies (US Silica F-95 Ottawa fine sand) (Hou *et al.* 2012). Air-water van Genuchten parameters were taken from fits to data from that earlier work (Hou *et al.* 2012); parameters for other systems were scaled from air-water values by Leverett scaling (Lenhard and Parker 1987). Four non-wetting phases were used to explore the effects of non-wetting phase properties on $\tau$ upscaling: air, hexane, tetrachloroethylene (PCE), and a silicone oil with a viscosity of 193.21 cP. These fluids were selected to cover the range of properties of fluids used in reported experimental measurements of $\tau$. With the exception of hexane, which is included to provide an additional intermediate data point, the specific fluids selected for this work have been studied by others in experimental measurements. For example, air-water experiments are perhaps the most widely reported (e.g., (Topp *et al.* 1967; Smiles *et al.* 1971; Vachaud *et al.* 1972; Stauffer 1978; Camps-Roach *et al.* 2010; Hou *et al.* 2012)), while both Sakaki *et al.* (2010) and Bottero *et al.* (2011b) report experiments conducted using PCE, and Das and Mirzaei (2012) and Mirzaei and Das (2013) report experiments with the high viscosity silicon oil used in these simulations. All simulations conducted for this work used water as the wetting phase. The properties of the porous medium and fluids used are shown in Table 5.1. Note that Table 5.1 includes a calculated value of the ratio of viscosity to interfacial tension – the portion of capillary number (*Ca*, the ratio of viscous forces to interfacial tension forces during flow) that depends on fluid properties. Because capillary number has a significant impact on fluid behavior during

multiphase flow, this ratio is used as a starting point to explore the impact of fluid properties on measured $\tau$ values.

**Table 5.1. Properties of the porous medium and fluids used in simulations. Fluid properties correspond to 20 °C, at atmospheric pressure.**

| Medium | $d_{50}$ (mm) | *Permeability* $K$ ($m^2$) | *Porosity* $\phi$ | $S_{wr}$ | $\alpha^a$ | $n^a$ |
|---|---|---|---|---|---|---|
| F-95 Sand | 0.140 | $2.27\times10^{-12}$ | 0.39 | 0.125 | 1.5064 | 12 |

| Fluid | *Density* $\rho$ ($kg/m^3$) | *Viscosity* $\mu$ (cP) | *Interfacial tension*[c] $\sigma$ *(mN/m)* | $\mu/\sigma$ *(s/m)* |
|---|---|---|---|---|
| Water (w) | 998 | 1.002 | -- | -- |
| Air (nw, g) | 1.2 | 0.018 | 72.9 | $2.47\times10^{-4}$ |
| Hexane (nw) | 658 | 0.31 | 51.9 | $5.97\times10^{-3}$ |
| PCE (nw) | 1623 | 0.89 | 45.7 | $1.95\times10^{-2}$ |
| Silicone oil[b] (nw) | 966 | 193.21 | 21.0 | 9.20 |

[a]van Genuchten parameters for the air-water system
[b]Reference: Clearco Products, Bensalem, PA.
[c]Interfacial tension of the liquid in contact with water

Many studies of dynamic capillary effects have used membranes or other capillary barriers to prevent breakthrough of the non-wetting phase (e.g., (Topp *et al.* 1967; Smiles *et al.* 1971; Chen *et al.* 2007; Camps-Roach *et al.* 2010; Goel and O'Carroll 2011; Hou *et al.* 2012)), while others have used membrane-free systems (e.g., (Vachaud *et al.* 1972; Bottero *et al.* 2011b)). The work described here uses a sink/source boundary condition for the wetting and nonwetting phases to maintain a constant water pressure at the bottom of the column (Sleep and Sykes 1993a). Fluxes of each phase are weighted by the respective relative permeabilities to avoid imposition of an outflow condition on a phase which is not present. This boundary condition simulates the effect of conducting a drainage in a column without an outlet capillary

barrier, similar to the experimental boundary condition used by Bottero et al. (2011b). It should be noted, however, that preliminary simulations conducted with a wetting phase capillary barrier bottom boundary condition showed quantitatively similar results in terms of the impacts of scaling and fluid properties on $\tau$. For this reason, the results of this work can be considered quantitatively applicable to either type of experimental boundary condition.

All simulations were conducted using properties evaluated at room temperature (293.15 K). The viscosities and densities of all fluids were held constant with pressure change during simulations except air density, which was allowed to vary with pressure.

### *5.2.3 Drainage simulations*

Simulations were started from a fully water-saturated condition. Non-wetting phase was introduced into the column through the top, while water flowed out of the column at the bottom (the total pressure boundary). The capillary pressure was imposed by incrementally increasing the pressure of the non-wetting phase at the top boundary up to a maximum pressure of 19.6 kPa (2.0 m water). Two different ramped pressure input rates were used: slow ($R$ = 0.001 cm water/s) and fast ($R$ = 0.016 cm water/s). Ramped inputs were modeled in CompSim as multiple small stepped inputs, with pressure increments at 5-50 s intervals for the duration of the ramp for all systems. Ramped inputs extended to 12,500 s (3.5 h) for all fast drainage simulations, and 200,000 s (12.5 h) for all slow drainage simulations – times required to reach the target nonwetting phase boundary pressure. In all systems except the silicone liquid, these times also corresponded to the systems at or near residual water saturation. In the case of the silicone liquid, the fast drainage simulation was extended an additional 20,000 s

at a constant non-wetting-phase boundary pressure (2.0 m water) to allow drainage to proceed to completion.

Saturation at the local scale was represented by simulated saturation at the midpoint of the column. Average saturations were calculated over four different length scales about the midpoint: 1.27, 2.54, 5.08 and 15.24 cm (0.5, 1, 2 and 6 in). Time derivatives of saturation (both local and at the different averaged length scales) were calculated by central difference.

## 5.3 Results and Discussion

### *5.3.1 Effect of fluid properties and rate on saturation profiles*

Figures 5.1 and 5.2 show the evolution of saturation profiles with drainage time in air-water (a) and organic-water (b-d) flow systems where slow (Fig. 5.1) or fast (Fig. 5.2) ramped pressure inputs were applied. Two major observations can be made from the results in Figs. 5.1 and 5.2. First, for a given ramped pressure rate, the saturation profiles are sharper (i.e., a more abrupt transition between fluids) for fluids with a higher ratio of viscosity to interfacial tension (Table 5.1). Second, a higher driving force for drainage (i.e., a higher ramped pressure input rate) corresponds to a sharper saturation profile for a given fluid.

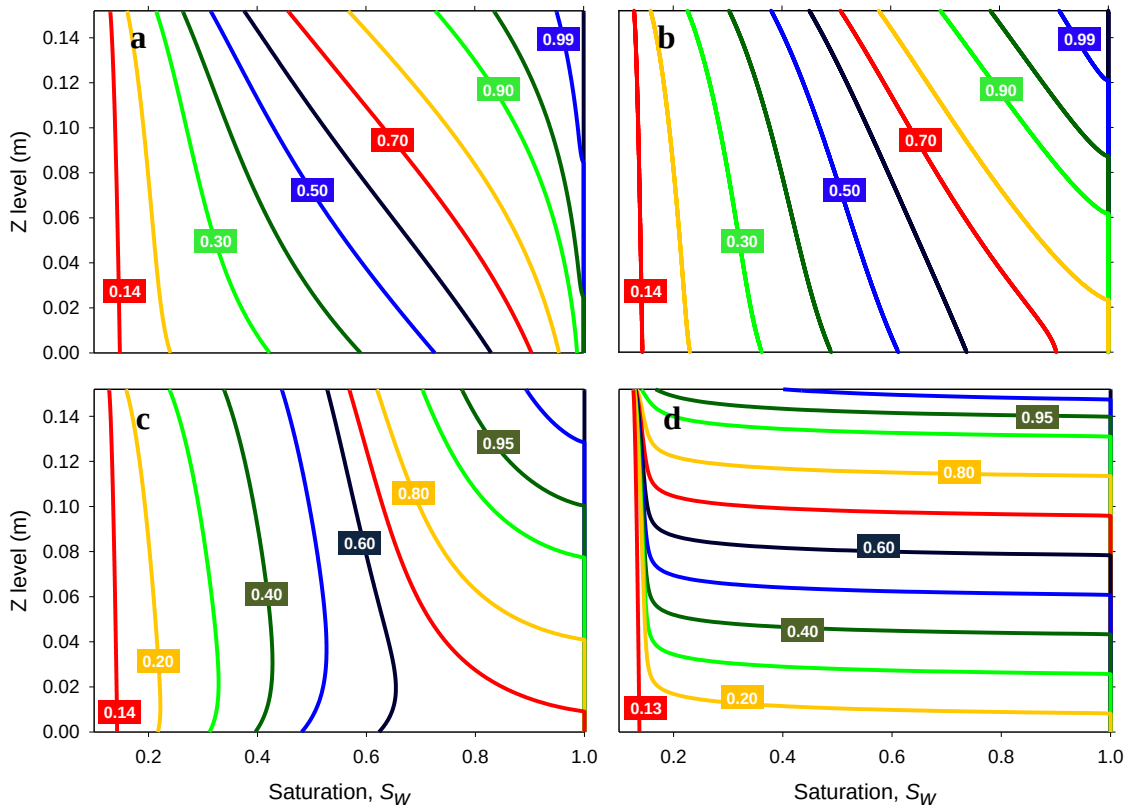


**Figure 5.1. Calculated water saturation profile evolution during drainage for slow (0.001 cm water/s) ramped pressure inputs. Shown for two-phase flow systems with (a) air, (b) hexane, (c) PCE, and (d) silicone oil as the non-wetting phase. Numbers correspond to average saturation of the profile with same color. (From right to left, the average saturations for each system in order are: 1.0, 0.99, 0.95, 0.9, 0.8, 0.7, 0.6, 0.5, 0.4, 0.3, 0.2, and saturation at the end of drainage simulation.)**

Regarding the effect of fluid properties, it is apparent from the figures that higher viscosity/lower interfacial tension fluids (e.g., the silicone liquid) exhibit more piston-like displacement of water, while lower viscosity/higher interfacial tension fluids (e.g., air) tend to produce drainage of water that is more gradually-distributed over a larger vertical portion of the column. This behavior is most notable at moderate-to-high average water saturations, before the non-wetting phase breaks through at the bottom of the column (interaction with the bottom boundary influences the shape of the profile).

The effect is also particularly notable when comparing the profiles of the high viscosity silicone liquid (Figs. 5.1d and 5.2d), with its extremely sharp profiles, with the other three non-wetting fluids (Figs. 5.1 a-c and 5.2 a-c), all of which exhibit more gradual profiles. Quantitatively, this effect can be seen by comparing the slopes of the saturation curves at the midpoint of the column as the front passes (i.e., just as the midpoint saturation drops below 1.0). Slopes of saturation as a function of elevation ($\partial S/\partial z$) calculated in slow drainage are -1.28, -6.14, -15.2, and -167 $m^{-1}$ corresponding to air-water ($\mu_{air}$ = 0.018 cP), hexane-water ($\mu_{hexane}$ = 0.31 cP), PCE-water ($\mu_{PCE}$ = 0.89 cP) and silicone oil-water ($\mu_{silicone}$ = 193.2 cP) flow systems, respectively.

Regarding the effect of the magnitude of the ramped pressure input, midpoint slopes for the fast drainage as the front passes are -2.86, -22.1, -43.4, and -219 $m^{-1}$ for air-water, hexane-water, PCE-water and silicone oil-water, respectively – approx. two-to-three times the slopes at the slower rate for all but the silicone oil-water case, which shows a factor of 1.3 difference between the fast and slow cases.

It should be emphasized that the results in Figs. 5.1 and 5.2 are not unexpected – they are simply the result of conventional multiphase flow phenomena. However, the different shapes of the profiles have quantitative implications for scale effects in the measurement of dynamic capillary effects. The remainder of this paper explores that relationship.

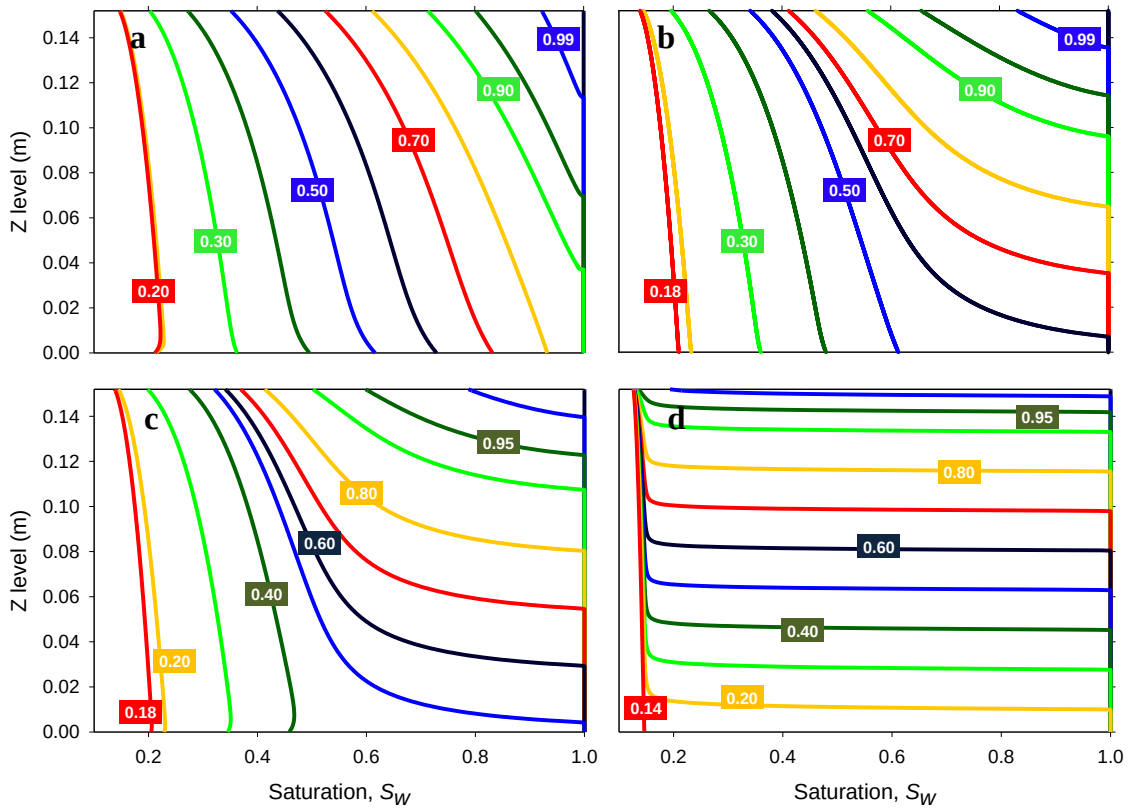


**Figure 5.2. Calculated water saturation profile evolution during drainage for fast (0.016 cm water/s) ramped pressure inputs. Shown for two-phase flow systems with (a) air, (b) hexane, (c) PCE, and (d) silicone oil as the non-wetting phase. Numbers correspond to average saturation of the profile with same color. (From right to left, the average saturations for each system in order are: 1.0, 0.99, 0.95, 0.9, 0.8, 0.7, 0.6, 0.5, 0.4, 0.3, 0.2, and saturation at the end of drainage simulation.)**

### *5.3.2 Differences between local and average saturations*

The fact that fluids are not uniformly distributed in porous media suggests that the saturation at any point within the column during drainage is likely different from the average saturation over some finite length centered on that point. In addition, because the fluids differ in the shapes of their saturation profiles, it is likely that the difference between the local and average saturation is a function of fluid properties. Figure 5.3 shows the comparison between the midpoint saturations and column-averaged saturations for each system at the slow and fast pressure rates. The horizontal axis of the

figure is the saturation over the entire column, while the vertical axis is the saturation at a single point at the midpoint of the column. Deviation of the curves from the 1:1 line is an indicator of conditions where the local and averaged saturations differ from one another. From the figure, it is apparent that the midpoint saturation is quite close to the column-averaged saturation for the air-water system, but with increasing fluid viscosity to interfacial tension ratio the differences become increasingly significant. For the hexane (Fig. 5.3b) and PCE (Fig. 5.3c) the greatest differences between the local and averaged saturations occur at higher saturations; the two saturations converge at lower saturations (this occurs because after fluid breakthrough for both fluids, the profiles are approximately linear between the top and bottom of the column). The most significant differences between local and averaged saturations are observed for the silicone oil-water system (Fig. 5.3d), which exhibits local saturations significantly greater than average saturations at high average saturations, and significantly lower than average saturations at low saturations. This phenomenon is purely the result of the very sharp saturation profiles. Quantitatively, the largest saturation difference is 2.28% for air-water, 6.94% for hexane-water, 10.2% for PCE-water, and 41.1% for silicone oil-water flow system at slow rate ($R$ = 0.001 cm water/s). The differences are 4.16%, 16.1%, 21.4%, and 42.4% for the corresponding systems at the fast rate ($R$ = 0.016 cm water/s). Thus, the difference is a function of both the fluid properties and drainage rate, with the differences in fluid properties between the systems studied producing a more significant impact than the difference in drainage rates studied.

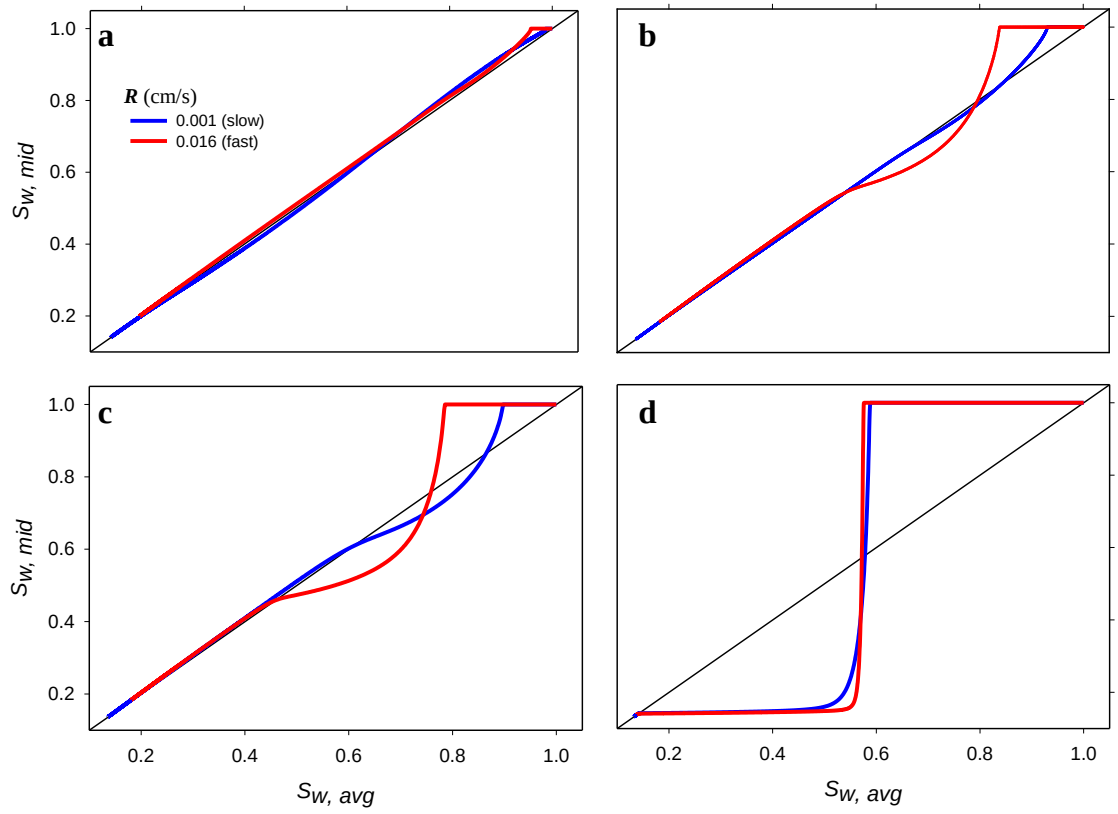


**Figure 5.3. Comparison of local (mid-point) and column average saturation for two-phase flow system with (a) air, (b) hexane, (c) PCE, and (d) silicone oil as the non-wetting phase. The black line is a 1:1 line.**

*5.3.3 Differences between local and average rates of saturation change*

If local and averaged saturations differ as they do in Fig. 5.3, it is reasonable to expect that local and averaged rates of saturation change ($\partial S_w/\partial t$) will also differ from one another. Figures 5.4 and 5.5 show both the local (midpoint) and column-averaged rates of saturation change as a function of saturation at slow (Fig. 5.4) and fast (Fig. 5.5) drainage rates. The figures also show the ratio in $\partial S_w/\partial t$ between the two values (i.e., mid-point values divided by column-averaged values). Results show that both fluid properties of the non-wetting phase and drainage rate affect the magnitude of the difference between local and averaged $\partial S_w/\partial t$. As might have been expected from Figs.

5.1 and 5.2, the impact of properties on the averaging is more significant than the impact of drainage rate for the range of properties and rates studied, with the fluids with the greatest ratio of viscosity to interfacial tension exhibiting the greatest difference between local and average rates of saturation change. In addition, note that the magnitude of the difference is a strong function of saturation, with quantitatively different behavior with saturation observed for the different fluids. While the $\partial S_w/\partial t$ ratios are nearly constant near 1.0 for air-water over much of the saturation range (Figs. 5.4a and 5.5a), the other fluids exhibit significant variation with saturation. Both hexane and PCE systems exhibit ratios near 1.0 at lower saturations. However, both exhibit significantly higher ratios at high saturations, with decreasing magnitudes with decreasing saturation. The ratio for the silicone liquid passes through a maximum at intermediate saturations.

It should be noted that the shape of the relationship between $\partial S_w/\partial t$ and saturation is a function of the type of pressure input used. For example, a step input instead of a ramped input will produce a $\partial S_w/\partial t$ maximum (and consequently, a $\partial S_w/\partial t$ ratio maximum) at different saturation values than the ramped inputs used here. However, the relationship between magnitude of the ratio and system properties will be quantitatively similar.

It should also be noted that while the results shown in Figs. 5.3-5.5 correspond to averaging over the entire 15.24 cm column length, behaviors observed for saturation averaging over smaller length scales are similar, but exhibit smaller magnitudes. The impact of averaging scale is explored in greater detail in the next section.

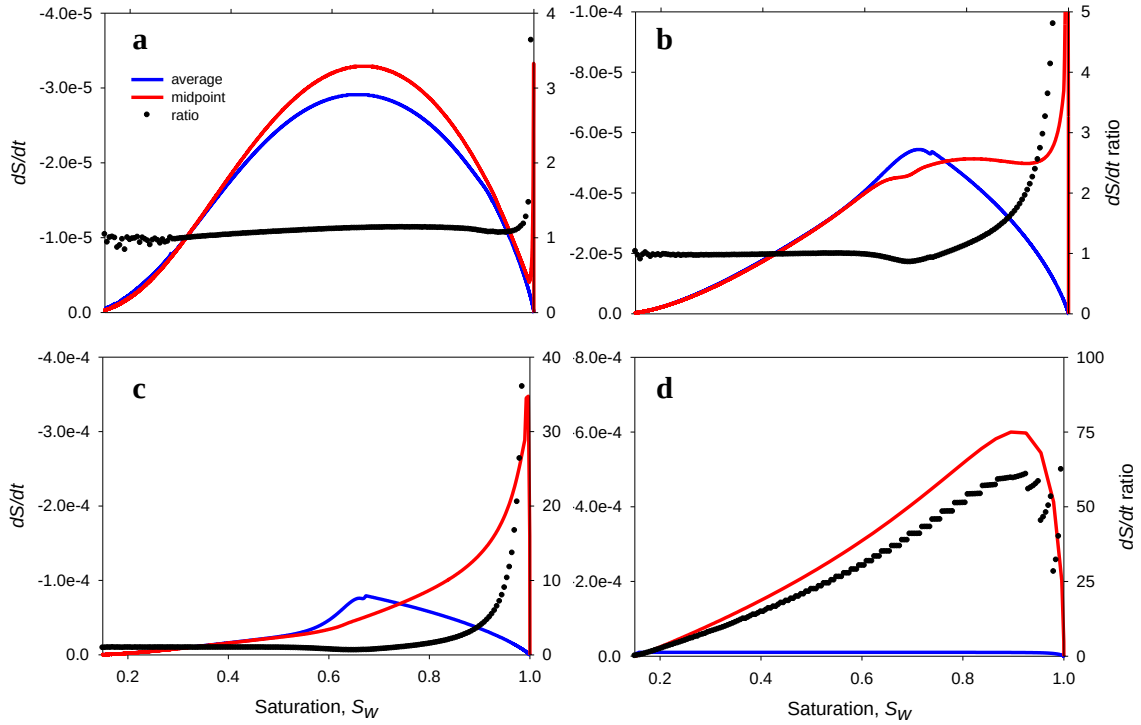


**Figure 5.4. Local (midpoint) and column-averaged $\partial S_w/\partial t$ as a function of $S_w$ for drainage in two-phase flow system with (a) air, (b) hexane, (c) PCE, and (d) silicone oil as the non-wetting phase. Curves correspond to slow ramped pressure inputs ($R$ = 0.001 cm water/s).**

### *5.3.4 Scale and fluid property effects in the τ multiplier*

As mentioned previously, because $\partial S_w/\partial t$ is in the denominator of Eq. 5.1, any averaging effects that influence the magnitude of a calculated $\partial S_w/\partial t$ will directly impact the value of $\tau$ calculated with Eq. 5.1. That means that the $\partial S_w/\partial t$ ratio described in Figs. 5.4 and 5.5 can be described as a $\tau$ multiplier:

$$\tau\ multiplier = \frac{\langle \partial S_w/\partial t \rangle_{local}}{\langle \partial S_w/\partial t \rangle_{avg}} \qquad \text{(Eq. 5.2)}$$

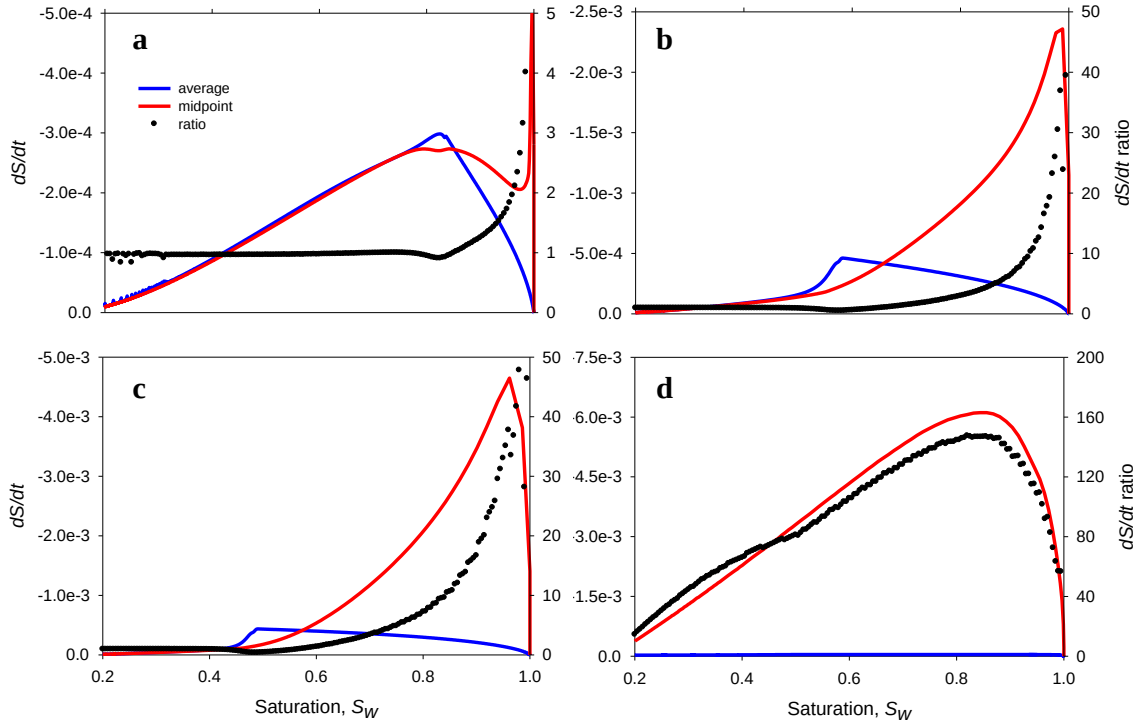


**Figure 5.5. Local (midpoint) and column-averaged $\partial S_w/\partial t$ as a function of $S_w$ for drainage in two-phase flow system with (a) air, (b) hexane, (c) PCE, and (d) silicone oil as the non-wetting phase. Curves correspond to fast ramped pressure inputs ($R$ = 0.016 cm water/s).**

That is, if there is a difference between $P_c^d$ and $P_c^s$, either due to a measurement artifact (e.g., (Hou *et al.* 2012)) or a true dynamic capillary effect, then any averaging in the saturation profile will cause the measured value of $\tau$ to be amplified by the ratio in Eq. 5.2.

Figure 5.6 shows a quantitative comparison of the maximum $\tau$ multipliers for all of the systems studied. The $\tau$ multipliers were calculated at a range of different averaging scales. (Note that in a few systems, brief spikes were calculated in local midpoint $\partial S_w/\partial t$ values at the onset of drainage from the midpoint (e.g., Fig. 5.5a, $S_w$~1.0) as a result of numerical noise. Maximum $\tau$ multipliers for each system were selected to exclude the spikes.) As might be expected, the values in Fig. 5.6 vary with

fluid properties (higher viscosity to interfacial tension ratio yields a higher $\tau$ multiplier), drainage rate (higher rate yields a higher $\tau$ multiplier), and averaging length (larger averaging length yields a higher $\tau$ multiplier).

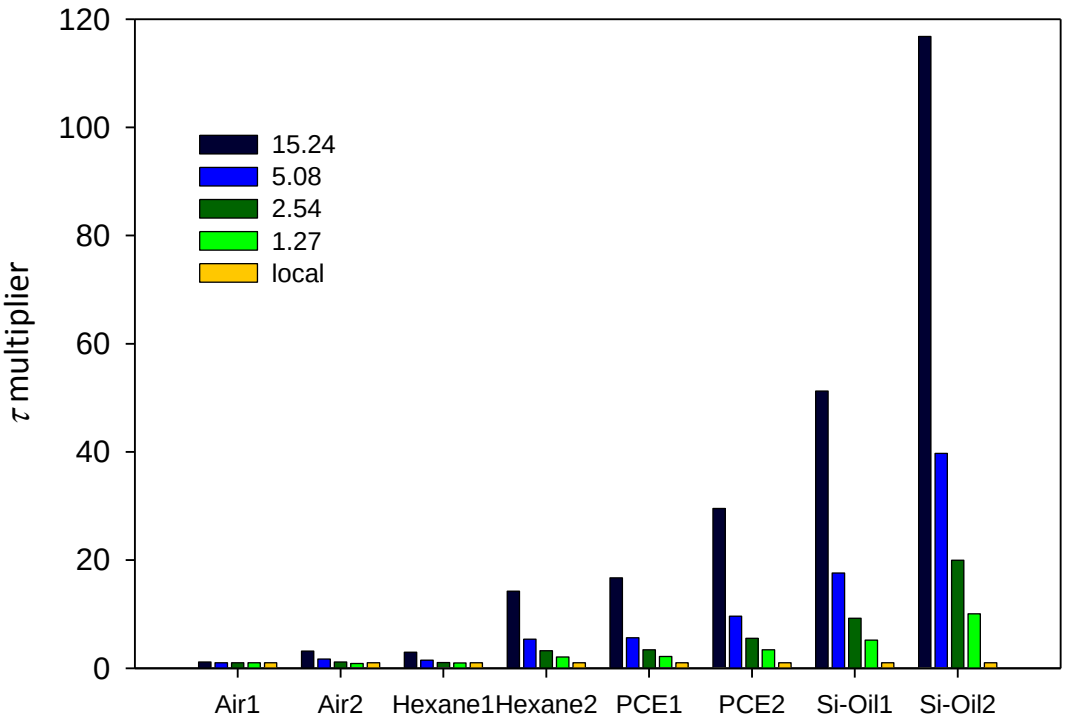


**Figure 5.6. Maximum $\tau$ multiplier ($<\partial S_w/\partial t>_{local}/<\partial S_w/\partial t>_{avg}$) at different averaging scales in two-phase flow systems under slow ($R$ = 0.001 cm water/s) and fast ($R$ = 0.016 cm water/s) input pressure rates.**

The effect of averaging scale length is important as no saturation sensor or saturation measurement method can measure saturation at a point; rather, all methods for measuring saturation measure saturation over some finite spatial range. Saturation values based on outflow measurements correspond to average saturations over the length of a column. Although little quantitative information is available regarding the spatial detection range of commercial moisture sensors, a range of one- to several cm is probable for typical sensor designs, based on the physical dimensions of the sensors

used (e.g., (Camps-Roach *et al.* 2010; Sakaki *et al.* 2010; Bottero *et al.* 2011b)). Consider, for example, a sensor that provides saturation values of over a 2.54 cm (1 inch) range – a very realistic estimate of the spatial range for a small commercial moisture sensor (e.g., (Limsuwat *et al.* 2009)). The results in Fig. 5.6 show that if experiments are conducted with the same sensor and pressure inputs, then spatial averaging by the saturation sensor would multiply measured PCE-water $\tau$ by ~6 compared with a value based on a point measurement, and would multiply a high viscosity silicone-water $\tau$ by as much as ~20 compared with a value based on a point measurement. In contrast, air-water experiments would be expected to exhibit very little impact from sensor averaging on calculated $\tau$ values under almost all conditions. This result highlights the extreme sensitivity of observed dynamic capillary effects to experimental measurements, and may in part explain some of the significant variability in values of $\tau$ reported to date for various measurement systems. Furthermore, the result highlights a potential source of systematic error in exploring the effect of fluid properties on $\tau$: even if two fluids systems have the same true $\tau$, measurements with a given column and set of measurement sensors will likely cause the measured $\tau$ in the high viscosity to surface tension ratio system to appear higher – perhaps many times higher – simply as a result of unavoidable volume averaging in the saturation measurement.

### *5.3.5 Capillary number and τ multiplier*

To get a better quantitative understanding of how fluid properties and drainage rates impact the measurement of $\tau$, calculations were conducted to explore the

relationship between capillary number and $\tau$ multiplier. For this work, we use the definition of capillary number given in Equation 5.3:

$$Ca = \frac{\mu q}{\sigma} \qquad \text{(Eq. 5.3)}$$

where $\mu$ is nonwetting fluid viscosity, $q$ is average water Darcy velocity (determined at a column average saturation of 0.8 for this comparison between systems from $q = -nL(\partial S_w/\partial t)_{avg}$ , where $n$ is porosity and $L$ is column length), and $\sigma$ is fluid interfacial tension.

Figure 5.7 shows calculated $\tau$ multiplier data at $S_w$ = 0.8 from all four fluid systems and two drainage rates studied in this work. Also shown are curves corresponding to calculated multipliers in a fluid system with a nonwetting-fluid density equal to that of water (determined by running simulations with synthetic fluid properties selected to cover the approx. five-order-of-magnitude range in *Ca* represented by these data). The figure shows the relationship between $\tau$ multiplier and capillary number at both the 15.24 cm (full column) and 2.54 cm scales. From the figure, it is apparent that the trends are similar at the two scales, but the magnitudes of the effect increases with increasing averaging scale. In general, at low capillary numbers (e.g., low flow rates, low viscosity, or high interfacial tension), the $\tau$ multiplier approaches 1.0, and scaling will have little impact on calculated $\tau$ values. As capillary number increases beyond some threshold value, the $\tau$ multiplier increases monotonically, with increases in capillary number producing order-of-magnitude increases in $\tau$ multiplier.

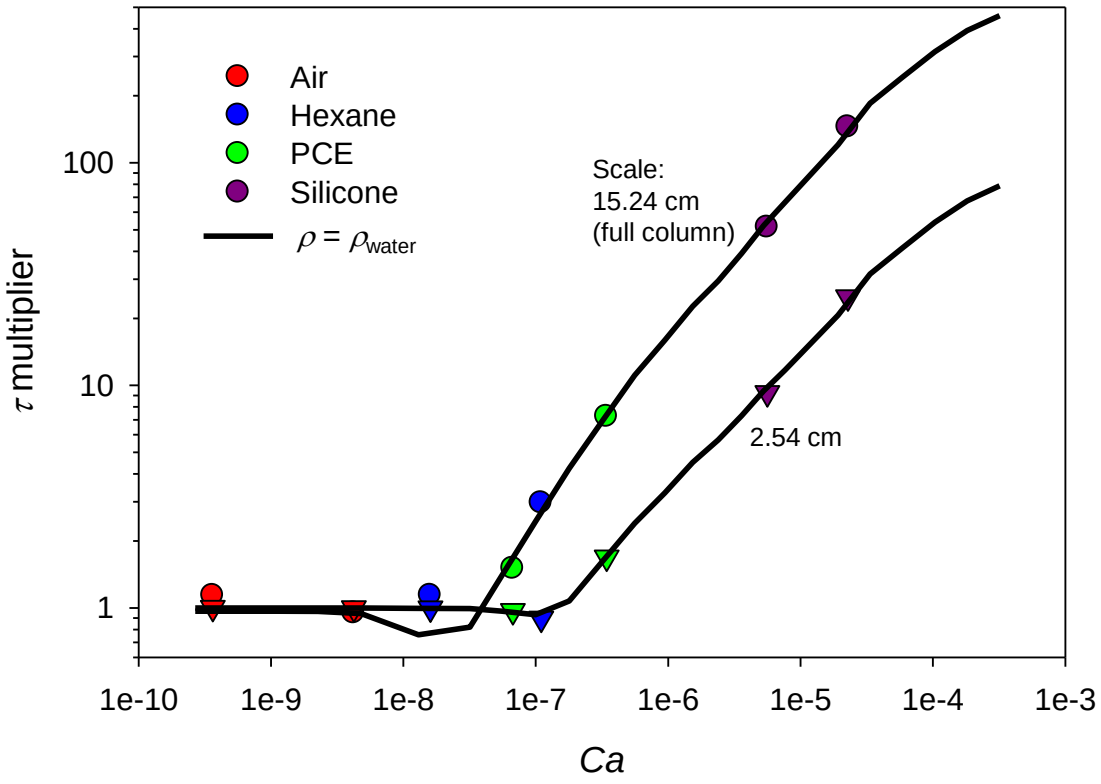


**Figure 5.7. τ multiplier ($\langle \partial S_w / \partial t \rangle_{local} / \langle \partial S_w / \partial t \rangle_{avg}$) at $S_w$=0.8 for all systems studied, shown as a function of capillary number (*Ca*). Circles correspond to full column (15.24 cm) averaging, while triangles correspond to averaging over 2.54 cm. Curves correspond to calculated τ multiplier over the range of *Ca* values with $\rho=\rho_{water}$.**

It is interesting to note that despite the very different densities of the fluids studied here, density appears to have little impact on the relationship between $\tau$ multiplier and capillary number, as evidenced by the very good agreement between the various fluids and the calculated curves in Fig. 5.7. However, it is important to note the one aspect of these results that is impacted by density: the small dip in the $\tau$ multiplier to values slightly below 1.0 observed near $Ca = 10^{-8}$, particularly for the full column averaging. This dip results entirely from a minor boundary effect in these simulations, and occurs when the nonwetting phase breaks through at the bottom of the column,

briefly increasing drainage rate from the bottom of the column. (The source of this boundary effect can also be seen in Figs. 5.4 and 5.5 where the average rate of saturation change briefly exceeds the local midpoint rate of saturation change over a small saturation range in several of the simulations. Comparison with Figs. 5.1 and 5.2 shows that the onset of this phenomenon corresponds to breakthrough of the nonwetting phase at the bottom of the column.) Density impacts this phenomenon by shifting the average saturation at which breakthrough occurs at a given capillary number, leading to differences in the magnitude of the dip at any given saturation. It should be emphasized that this effect is significantly reduced when averaging is conducted over only a portion of a column (e.g., the 2.54 cm scale in Fig. 5.7). Furthermore, it should be emphasized that the fact that this phenomenon only occurs in regions where $\tau$ multiplier is near 1.0 means that it is of less importance for interpreting experimental measurements than the order-of-magnitude increases in $\tau$ multiplier observed with increasing capillary number at high capillary numbers in Fig. 5.7.

## 5.4 Conclusions

Using the CompSim multiphase flow simulator, a series of numerical experiments was conducted to explore the effect of fluid properties on fluid saturation averaging. The objective of the work was to better understand implications of unavoidable spatial averaging for experimental measurement of dynamic capillary effects. Four different non-wetting phase fluids were examined, with viscosities covering four orders of magnitude, consistent with the range of viscosities of fluids used in published experimental studies of dynamic capillary effects.

Results show that differences exist between local values of saturation and spatially averaged values of saturation. The differences become more significant as viscosity to interfacial tension ratio of the non-wetting phase increases. Differences are also more significant for more rapid drainage rates. Similarly, the differences between local and averaged rates of saturation change ($\partial S_w/\partial t$) are more significant for larger non-wetting phase viscosity to interfacial tension ratios and greater drainage rates.

A $\tau$ multiplier was defined as the ratio of local and averaged $\partial S_w/\partial t$ values. The $\tau$ multiplier is an indicator of the extent to which spatial averaging in a system will influence the calculated $\tau$ by changing the apparent $\partial S_w/\partial t$. Systems with high capillary number (e.g., high viscosity, low interfacial tension, high drainage rate) are more sensitive to averaging artifacts, and are more likely to exhibit measurements which significantly overstate the values of $\tau$. This effect may be the source of some of the significant variability in reported $\tau$ values, and could potentially produce systematic errors in experiments conducted with different fluids.

# Chapter 6. Summary and Conclusions

A quantitative understanding of dynamic capillary effects in $P_c$-$S_w$ relationships could be critical for accurate modeling of multiphase flow through porous media. However, reported results about the magnitudes and system dependencies of dynamic effects have been contradictory, even for seemingly very similar systems. In this study, experiments and simulations were conducted to investigate the experimental factors that could possibly mimic dynamic capillary effects, resulting in erroneous interpretation of data. The main findings are described as follow.

In Chapter 3, dynamic drainage experiments were conducted in different unsaturated flow systems in a small-volume cell with two pore-pressure sensors added. The flow systems involved two porous materials with different grain size, and two wetting phases with different viscosities. In all experiments, inlet gas pressures were recorded. The two pore-pressure sensors were used to record either a combination of gas pressures and water pressures, or two water pressures. Uncorrected and corrected dynamic capillary pressures and corresponding $\tau$ values were determined. Up to two corrections about the pressures measured were made. First, phase pressures were corrected based on the response rates of the pore-pressure sensors determined. Second, for gas pressures measured at the inlet, pore gas pressures at the vertical central level were calculated based on Darcy's Law and relative gas permeability. Results show that uncorrected $\tau$ values vary significantly between different systems, with values as high as $10^5$ Pa·s. In regard to corrected results, $\tau$ values measured in this work were found to be very small in magnitude, and largely independent of system properties. Results of

this work suggest that experimental artifacts can have a profound impact on measurement of the $\tau$.

In Chapter 4, gas pressure gradients and drops in porous media were further examined using experiments and simulations in large columns. In the experiments, average saturations and phase pressures at the vertical midpoint as well as applied gas pressures were measured during dynamic drainage. Results show that significant gas pressure drops or gradients were observed in system without any boundary restrictions. Adding inflow restrictions enhances the gas pressure drops, while adding outflow restrictions reduces the drops. Introducing a vent near the phase pressure sensors was not observed to diminish the pressure drops within the porous media.

In Chapter 5, the impact of fluid properties on the scale-dependences of $\tau$ and experimentally-determined $\tau$ values were numerically studied. Previous work (Chapter 3) suggested that scale dependence of $\tau$ may depend on the properties of fluids, as a result of the shape of the saturation profile. Simulations in Chapter 5 explored this question using four non-wetting phase fluids and two drainage rates. Local and average saturations were computed, as well as corresponding rates of saturation change. Results show that different flow behaviors were observed in systems with different non-wetting phase fluids. This difference in behavior causes the experimentally-obtained $\tau$ presenting very different dependence on system scales for different systems. Specifically, accurate values of $dS_w/dt$ are necessary to precisely determine values of $\tau$ at given saturations. Scale-dependence of $\tau$ can be evaluated by comparing local and average $dS_w/dt$ values, the ratio of which is affected by both drainage rates and fluid properties. The ratio of local to spatial average $dS_w/dt$ increases with increasing

drainage rate and fluid viscosity-to-interfacial tension ratio, suggesting that the scale-dependence of $\tau$ is more significant in systems with greater drainage rate or with greater fluid viscosity-to-interfacial tension ratios (e.g., PCE vs. air). Because soil moisture sensors can only record saturation for certain spatial ranges rather than for a local point, the results have important implications on understanding the scale-dependent of $\tau$ for different systems and on evaluating variations of measured $\tau$ in different studies. To compare the magnitude and system dependence of $\tau$ obtained through different experiment set-ups, their differences in drainage rate and spatial measurement range of soil moisture sensor should be taken into account.

# References


Adamson, A. W. and A. P. Gast (1997). Physical chemistry of surfaces. A Wiley-Interscience publication. New York, Wiley**:** 1 online resource (xxi, 784 pages).

Armstrong, R. T., M. L. Porter, et al. (2012). "Linking pore-scale interfacial curvature to column-scale capillary pressure." Advances in Water Resources **46**: 55-62.

Barenblatt, G. I., T. W. Patzek, et al. (2003). "The mathematical model of nonequilibrium effects in water-oil displacement." SPE Journal **8**(4): 409-416.

Bear, J. (1972). Dynamics of Fluids in Porous Media. New York, American Elsevier Pub. Co.

Bhattarai, S. P., N. H. Su, et al. (2005). "Oxygation unlocks yield potentials of crops in oxygen-limited soil environments." Advances in Agronomy, Vol 88 **88**: 313-+.

Bottero, S. (2009). Advances in the Theory of Capillarity in Porous Media. Doctor of Philosophy Ph.D. Thesis, Universiteit Utrecht.

Bottero, S., S. M. Hassanizadeh, et al. (2011a). "From Local Measurements to an Upscaled Capillary Pressure-Saturation Curve." Transport in Porous Media **88**(2): 271-291.

Bottero, S., S. M. Hassanizadeh, et al. (2011b). "Nonequilibrium Capillarity Effects in Two-phase Flow Through Porous Media at Different Scales." Water Resources Research **47**.

Bourgeat, A. and M. Panfilov (1998). "Effective Two-phase Flow through Highly Heterogeneous Porous Media: Capillary Nonequilibrium Effects." Computational Geosciences **2**(3): 191-215.

Brooks, R. H. and A. T. Corey (1966). "Properties of Porous Media Affecting Fluid Flow." Journal of the Irrigation and Drainage Division **92**(2): 61-90.

Burdine, N. T. (1953). "Relative Permeability Calculations from Pore Size Distribution Data." Transactions of the American Institute of Mining and Metallurgical Engineers **198**: 71-78.

Butters, G. L. and P. Duchateau (2002). "Continuous Flow Method for Rapid Measurement of Soil Hydraulic Properties: I. Experimental Considerations." Vadose Zone Journal **1**(2): 239-251.

Camps-Roach, G., D. M. O'Carroll, et al. (2010). "Experimental Investigation of Dynamic Effects in Capillary Pressure: Grain Size Dependency and Upscaling." Water Resources Research **46**.

Chen, J., J. W. Hopmans, et al. (1999). "Parameter estimation of two-fluid capillary pressure-saturation and permeability functions." Advances in Water Resources **22**(5): 479-493.

Chen, L. X. and T. C. G. Kibbey (2006). "Measurement of air-water interfacial area for multiple hysteretic drainage curves in an unsaturated fine sand." Langmuir **22**(16): 6874-6880.

Chen, L. X., G. A. Miller, et al. (2007). "Rapid Pseudo-static Measurement of Hysteretic Capillary Pressure-saturation Relationships in Unconsolidated Porous Media." Geotechnical Testing Journal **30**(6): 474-483.

Civan, F. (2012). "Temperature dependency of dynamic coefficient for nonequilibrium capillary pressure-saturation relationship." Aiche Journal **58**(7): 2282-2285.

Class, H., A. Ebigbo, et al. (2009). "A benchmark study on problems related to CO2 storage in geologic formations." Computational Geosciences **13**(4): 409-434.

Costanza-Robinson, M. S., B. D. Estabrook, et al. (2011). "Representative elementary volume estimation for porosity, moisture saturation, and air-water interfacial areas in unsaturated porous media: Data quality implications." Water Resources Research **47**.

Dahle, H. K., M. A. Celia, et al. (2005). "Bundle-of-tubes Model for Calculating Dynamic Effects in the Capillary-pressure-saturation Relationship." Transport in Porous Media **58**(1-2): 5-22.

Dane, J. H. and J. W. Hopmans (2002). Water Retention and Storage: Laboratory. Methods of Soil Analysis. J. H. Dane and G. C. Topp. Madison WI, Soil Science Society of America. **Part 4:** 675-720.

Das, D. B., S. M. Hassanizadeh, et al. (2004). "A Numerical Study of Micro-Heterogeneity Effects on Upscaled Properties of Two-phase Flow in Porous Media." Transport in Porous Media **56**(3): 329-350.

Das, D. B. and M. Mirzaei (2012). "Dynamic Effects in Capillary Pressure Relationships for Two-phase Flow in Porous Media: Experiments and Numerical Analyses." AIChE Journal **58**(12): 3891-3903.

Davidson, J. M., D. R. Nielsen, et al. (1966). "Dependence of Soil Water Uptake and Release Uoon Applied Pressure Increment." Soil Science Society of America Proceedings **30**(3): 298-&.

Diamantopoulos, E., S. C. Iden, et al. (2012). "Inverse modeling of dynamic nonequilibrium in water flow with an effective approach." Water Resources Research **48**.

Eching, S. O. and J. W. Hopmans (1993). "Optimization of Hydraulic Functions from Transient Outflow and Soil-Water Pressure Data." Soil Science Society of America Journal **57**(5): 1167-1175.

Eching, S. O., J. W. Hopmans, et al. (1994). "Unsaturated Hydraulic Conductivity from Transient Multistep Outflow and Soil-Water Pressure Data." Soil Science Society of America Journal **58**(3): 687-695.

Farrell, D. A. and W. E. Larson (1972). "Modeling Pore Structure of Porous Media." Water Resources Research **8**(3): 699-&.

Fetter, C. W. (2001). Applied hydrogeology. Upper Saddle River, N.J., Prentice Hall.

Fischer, U., O. Dury, et al. (1997). "Modeling nonwetting-phase relative permeability accounting for a discontinuous nonwetting phase." Soil Science Society of America Journal **61**(5): 1348-1354.

Friedman, S. P. (1999). "Dynamic contact angle explanation of flow rate-dependent saturation-pressure relationships during transient liquid flow in unsaturated porous media." Journal of Adhesion Science and Technology **13**(12): 1495-1518.

Gardner, W. (1920). "The Capillary Potential and Its Relation to Soil Moisture Constants." Soil Science **10**(5): 357-360.

Gardner, W. R. (1956). "Calculation of Capillary Conductivity from Pressure Plate Outflow Data1." Soil Sci. Soc. Am. J. **20**(3): 317-320.

Gardner, W. R. (1958). "Some Steady-state Solutions of the Unsaturated Moisture Fow Equation with Application to Evaporation from a Water Table." Soil Science **85**(4): 228-232.

Gielen, T., S. M. Hassanizadeh, et al. (2005). Dynamic Effects in Multiphase Flow: A Pore-scale Network Approach. Upscaling Multiphase Flow in Porous Media. D. B. Das and S. M. Hassanizadeh, Springer Netherlands 217-236.

Goel, G. and D. M. O'Carroll (2011). "Experimental Investigation of Nonequilibrium Capillarity Effects: Fluid Viscosity Effects." Water Resources Research **47**.

Hassanizadeh, S. M., M. A. Celia, et al. (2002). "Dynamic Effect in the Capillary Pressure-Saturation Relationship and its Impacts on Unsaturated Flow." Vadose Zone Journal **1**(1): 38-57.

Hassanizadeh, S. M. and W. G. Gray (1990). "Mechanics and Thermodynamics of Multiphase Flow in Porous-Media Including Interphase Boundaries." Advances in Water Resources **13**(4): 169-186.

Hassanizadeh, S. M. and W. G. Gray (1993a). "Thermodynamic Basis of Capillary-Pressure in Porous-Media." Water Resources Research **29**(10): 3389-3405.

Hassanizadeh, S. M. and W. G. Gray (1993b). "Toward an Improved Description of the Physics of 2-Phase Flow." Advances in Water Resources **16**(1): 53-67.

Helmig, R., A. Weiss, et al. (2007). "Dynamic capillary effects in heterogeneous porous media." Computational Geosciences **11**(3): 261-274.

Hiemenz, P. C. and R. Rajagopalan (1997). Principles of colloid and surface chemistry. New York, Marcel Dekker.

Hou, L. L., L. X. Chen, et al. (2012). "Dynamic Capillary Effects in a Small-volume Unsaturated Porous Medium: Implications of Sensor Response and Gas Pressure Gradients for Understanding System Dependencies." Water Resources Research **48**.

Hou, L. L., B. E. Sleep, et al. (2014). "The influence of unavoidable saturation averaging on the experimental measurement of dynamic capillary effects: A numerical simulation study." Advances in Water Resources **66**: 43-51.

Huyakorn, P. S. and G. F. Pinder (1986). Computational methods in subsurface flow.

Joekar-Niasar, V. and S. M. Hassanizadeh (2011). "Effect of Fluids Properties on Non-equilibrium Capillarity Effects: Dynamic Pore-network Modeling." International Journal of Multiphase Flow **37**(2): 198-214.

Joekar-Niasar, V., S. M. Hassanizadeh, et al. (2010). "Non-equilibrium effects in capillarity and interfacial area in two-phase flow: dynamic pore-network modelling." Journal of Fluid Mechanics **655**: 38-71.

Juanes, R. (2008). "Nonequilibrium effects in models of three-phase flow in porous media." Advances in Water Resources **31**(4): 661-673.

Kalaydjian, F. (1992). Dynamic capillary pressure curve for water/oil displacement in porous media: theory vs. experiment. . Richardson, Texas, Society of Petroleum Engineers**:** 16.

Klute, A. and W. R. Gardner (1962). "Tensiometer Response Time." Soil Science **93**(3): 204-207.

Kool, J. B., J. C. Parker, et al. (1985). "Determining Soil Hydraulic-Properties from One-Step Outflow Experiments by Parameter-Estimation .1. Theory and Numerical-Studies." Soil Science Society of America Journal **49**(6): 1348-1354.

Kuang, X. X. and J. J. Jiao (2011). "A new model for predicting relative nonwetting phase permeability from soil water retention curves." Water Resources Research **47**.

Lenhard, R. J. and J. C. Parker (1987). "Measurement and Prediction of Saturation-pressure Relationships in Three-phase Porous Media Systems." Journal of Contaminant Hydrology **1**(4): 407-424.

Leverett, M. C. (1941). "Capillary behavior in porous solids." Transactions of the American Institute of Mining and Metallurgical Engineers **142**: 152-169.

Limsuwat, A., T. Sakaki, et al. (2009). Experimental Quantification of Bulk Sampling Volume of ECH2O Soil Moisture Sensors. 2009 Annual American Geophysical Union Hydrology Days, Colo. State Univ., Fort Collins, Colorado.

Manthey, S., S. M. Hassanizadeh, et al. (2005). "Macro-scale Dynamic Effects in Homogeneous and Heterogeneous Porous Media." Transport in Porous Media **58**(1-2): 121-145.

Mirzaei, M. and D. B. Das (2013). "Experimental Investigation of Hysteretic Dynamic Effect in Capillary Pressure–Saturation Relationship for Two-phase Flow in Porous Media." Aiche Journal **59**(10): 3958-3974.

Mittelbach, H., F. Casini, et al. (2011). "Soil moisture monitoring for climate research: Evaluation of a low-cost sensor in the framework of the Swiss Soil Moisture Experiment (SwissSMEX) campaign." Journal of Geophysical Research-Atmospheres **116**.

Mittelbach, H., I. Lehner, et al. (2012). "Comparison of four soil moisture sensor types under field conditions in Switzerland." Journal of Hydrology **430**: 39-49.

Mualem, Y. (1976). "New Model for Predicting Hydraulic Conductivity of Unsaturated Porous-Media." Water Resources Research **12**(3): 513-522.

Muraleetharan, K. K. and C. F. Wei (1999). "Dynamic behaviour of unsaturated porous media: Governing equations using the theory of mixtures with interfaces (TMI)." International Journal for Numerical and Analytical Methods in Geomechanics **23**(13): 1579-1608.

Nielsen, D. R., J. W. Biggar, et al. (1962). "Experimental Consideration of Diffusion Analysis in Unsaturated Flow Problems1." Soil Sci. Soc. Am. J. **26**(2): 107-111.

O'Carroll, D. M., T. J. Phelan, et al. (2005). "Exploring dynamic effects in capillary pressure in multistep outflow experiments." Water Resources Research **41**(11).

O'Carroll, D. M. and B. E. Sleep (2007). "Hot Water Flushing for Immiscible Displacement of a Viscous NAPL." Journal of Contaminant Hydrology **91**(3-4): 247-266.

Oliviera, I. B., A. H. Demond, et al. (1996). "Packing of Sands for the Production of Homogeneous Porous Media." Soil Sci. Soc. Am. J. **60**(1): 49-53.

Oung, O., S. M. Hassanizadeh, et al. (2005). "Two-phase Flow Experiments in a Geocentrifuge and the Significance of Dynamic Capillary Pressure Effect." Journal of Porous Media **8**(3): 247-257.

Parker, J. C., J. B. Kool, et al. (1985). "Determining Soil Hydraulic-Properties from One-Step Outflow Experiments by Parameter-Estimation .2. Experimental Studies." Soil Science Society of America Journal **49**(6): 1354-1359.

Parker, J. C., R. J. Lenhard, et al. (1987). "A Parametric Model for Constitutive Properties Governing Multiphase Flow in Porous-Media." Water Resources Research **23**(4): 618-624.

Plug, W. J. and J. Bruining (2007). "Capillary pressure for the sand-CO2-water system under various pressure conditions. Application to CO2 sequestration." Advances in Water Resources **30**(11): 2339-2353.

Richards, L. A. (1928). "The usefulness of capillary potential to soil moisture and plant investigators." Journal of Agricultural Research **37**: 0719-0742.

Richards, L. A. (1949). "Methods of Measuring Soil Moisture Tension." Soil Science **68**(1): 95.

Rogers, J. S. and A. Klute (1971). "Hydraulic Conductivity-Water Content Relationship during Nonsteady Flow through a Sand Column." Soil Science Society of America Proceedings **35**(5): 695-&.

Rosen, M. J. (2004). Surfactants and interfacial phenomena. A Wiley-Interscience publication. Hoboken, N.J., Wiley-Interscience**:** 1 online resource (xiii, 444 pages).

Sakaki, T., A. Limsuwat, et al. (2008). "Empirical two-point alpha-mixing model for calibrating the ECH(2)O EC-5 soil moisture sensor in sands." Water Resources Research **44**.

Sakaki, T., D. M. O'Carroll, et al. (2010). "Direct Quantification of Dynamic Effects in Capillary Pressure for Drainage-Wetting Cycles." Vadose Zone Journal **9**(2): 424-437.

Sehayek, L., T. D. Vandell, et al. (1999). "Investigation and Remediation of a 1,2-dichloroethane Spill Part I: Short and Long-term Remediation Strategies." Ground Water Monitoring and Remediation **19**(3): 71-81.

Selker, J., P. Leclerq, et al. (1992). "Fingered Flow in 2 Dimensions .1. Measurement of Matric Potential." Water Resources Research **28**(9): 2513-2521.

Selker, J. S., C. K. Keller, et al. (1999). Vadose zone processes. Boca Raton, Fla., Lewis Publishers.

Simunek, J. and J. R. Nimmo (2005). "Estimating soil hydraulic parameters from transient flow experiments in a centrifuge using parameter optimization technique." Water Resources Research **41**(4).

Sleep, B. E. and J. F. Sykes (1993a). "Compositional Simulation of Groundwater Contamination by Organic-Compounds .1. Model Development and Verification." Water Resources Research **29**(6): 1697-1708.

Sleep, B. E. and J. F. Sykes (1993b). "Compositional Simulation of Groundwater Contamination by Organic-Compounds .2. Model Applications." Water Resources Research **29**(6): 1709-1718.

Smiles, D. E., G. Vachaud, et al. (1971). "A Test of Uniqueness of Soil Moisture Characteristic during Transient Nonhysteretic Flow of Water in a Rigid Soil." Soil Science Society of America Proceedings **35**(4): 534-539.

Stauffer, F. (1978). Time dependence of the relations between capillary pressure, water content and conductivity during drainage of porous media. Thessaloniki, Greece.

Todd, D. K. and L. W. Mays (2005). Groundwater hydrology. Hoboken, NJ, Wiley.

Topp, G. C., A. Klute, et al. (1967). "Comparison of Water Content-Pressure Head Data Obtained by Equilibrium Steady-State and Unsteady-State Methods." Soil Science Society of America Proceedings **31**(3): 312-314.

Towner, G. D. (1980). "Theory of time response of tensiometers." Journal of Soil Science **31**(4): 607-621.

Vachaud, G., M. Vauclin, et al. (1973). "Effects of Air Pressure on Water Flow in an Unsaturated Stratified Vertical Column of Sand." Water Resources Research **9**(1): 160-173.

Vachaud, G., M. Vauclin, et al. (1972). "Study of Uniqueness of Soil-Moisture Characteristic during Desorption by Vertical Drainage." Soil Science Society of America Proceedings **36**(3): 531.

van Genuchten, M. T. (1980). "A Closed-form Equation for Predicting the Hydraulic Conductivity of Unsaturated Soils." Soil Sci. Soc. Am. J. **44**(5): 892-898.

Vogel, H. J., A. Samouelian, et al. (2008). "Multi-step and two-step experiments in heterogeneous porous media to evaluate the relevance of dynamic effects." Advances in Water Resources **31**(1): 181-188.

Watson, K. K. (1966). "An Instantaneous Profile Method for Determining Hydraulic Conductivity of Unsaturated Porous Materials." Water Resources Research **2**(4): 709-&.

Watson, K. K. and F. D. Whisler (1968). "System Dependence of Water Content-Pressure Head Relationship." Soil Science Society of America Proceedings **32**(1): 121-123.

Weitz, D. A., J. P. Stokes, et al. (1987). "Dynamic Capillary Pressure in Porous Media: Origin of the Viscous-Fingering Length Scale." Physical Review Letters **59**(26): 2967-2970.

Wildenschild, D., J. W. Hopmans, et al. (2005). "Quantitative analysis of flow processes in a sand using synchrotron-based X-ray microtomography." Vadose Zone Journal **4**(1): 112-126.

Wildenschild, D., J. W. Hopmans, et al. (2001). "Flow rate dependence of soil hydraulic characteristics." Soil Science Society of America Journal **65**(1): 35-48.